sensors

MDPI

Article

Geometric Accuracy Evaluation of High-Resolution Satellite Images Based on Xianning Test Field

Xiongwei Zheng [1], Qi Huang [2], Jingjing Wang [3], Taoyang Wang [2,*] and Guo Zhang [4]

1 China Aero Geophysical Survey & Remote Sensing Center for Land and Resources, Beijing 100083, China; zheng_xiongwei@163.com
2 School of Remote Sensing and Information Engineering, Wuhan University, Wuhan 430079, China; qihuang@whu.edu.cn
3 Shandong Institute of Geological Surveying and Mapping, Shandong 250011, China; skdwangjing@126.com
4 State Key Laboratory of Information Engineering in Surveying, Mapping and Remote Sensing, Wuhan University, Wuhan 430079, China; guozhang@whu.edu.cn
* Correspondence: wangtaoyang@whu.edu.cn; Tel.: +86-134-7609-3672

Received: 6 April 2018; Accepted: 20 June 2018; Published: 2 July 2018

Abstract: The evaluation of geometric accuracy of high-resolution satellite images (HRSIs) has been increasingly recognized in recent years. The traditional approach is to verify each satellite individually. It is difficult to directly compare the difference in their accuracy. In order to evaluate geometric accuracy for multiple satellite images based on the same ground control benchmark, a reliable test field in Xianning (China) was utilized for geometric accuracy validation of HRSIs. Our research team has obtained multiple HRSIs in the Xianning test field, such as SPOT-6, Pleaides, ALOS, ZY-3 and TH-1. In addition, ground control points (GCPs) were acquired with GPS by field surveying, which were used to select the significant feature area on the images. We assess the orientation accuracy of the HRSIs with the single image and stereo models. Within this study, the geometrical performance of multiple HRSIs was analyzed in detail, and the results of orientation are shown and discussed. As a result, it is feasible and necessary to establish such a geometric verification field to evaluate the geometric quality of multiple HRSIs.

Keywords: high resolution satellite images; test field; geometrical performance; evaluation; accuracy

1. Introduction

During the last decade, with the improvement of the resolution of HRSIs (Table 1), whose geometric positioning capabilities have also been gradually enhanced, the use of satellite images to produce large-scale topographic maps has become possible. Due to the distinctive feature of high-precision positioning of HRSIs, as well as the stringent requirements of high accuracy and high reliability in mapping, establishing a high stability and long-term continuous-operation scientific testing base for remote sensing and mapping will have significance and practical value.

Table 1. High-resolution optical satellite system. PAN: panchromatic, MS: multispectral, SWIR: Shortwave infrared.

Satellite	Nation	Launch Date	Bands	Spatial Resolution/m	Width/km
IKONOS	America	24 September 1999	PAN/MS	1/4	11
QuickBird	America	18 October 2001	PAN/MS	0.61/2.44	16.5
SPOT-5	France	4 May 2002	PAN/MS/SWIR	2.5/10/20	60
SPOT-6	France	9 September 2012	PAN/MS	1.5/6.0	60
CBERS-02B	China	21 October 2003	PAN/MS	2.36/20	27
Cartosat-1	India	5 May 2005	PAN	2.5 (forward), 2.2 (backward)	26
ALOS	Japan	24 January 2006	PAN/MS	2.5/10	35/70

Table 1. *Cont.*

Satellite	Nation	Launch Date	Bands	Spatial Resolution/m	Width/km
EROS-B	Israel	25 April 2006	PAN	0.7	14
Cartosat-2	India	10 January 2007	PAN	<1	10
WorldView-1	America	18 September 2007	PAN	0.5	17.6
GeoEye-1	America	6 September 2008	PAN/MS	0.41/1.65	15.2
WorldView-2	America	8 October 2009	PAN/MS	0.46/1.84	16.4
WorldView-3	America	13 August 2014	PAN/MS/SWIR	0.31/1.24	13.2
ZY3	China	9 January 2012	PAN/MS	2.1 (nadir)/3.5 (forward, backward)/5.8	52
TH-1	China	24 August 2010	PAN/MS	2 (HR)/5 (forward, backward, nadir)/10	60
Pléiades	France	17 December 2011	PAN/MS	0.5/2.0	20

Many research institutions, as well as experts and scholars, have done a lot of investigation and research work for the geometric calibration and validation of sensors. The Modular Optoelectronic Multispectral Scanner (MOMS-2P) was developed by DLR (Deutsches Zentrum für Luft- und Raumfahrt). The DLR updated the calibration data combined with photogrammetric bundle adjustment using an adapted functional model for the reconstruction of the interior orientation. In addition, it also compares the results of geometric laboratory calibration. The calibration field is located in the southern part of Germany and Austria [1,2]. Fraser et al. use different model to process the IKONOS images. The results can yield 3D object-point determination with an accuracy of 0.5 m in plane and 0.7 m in height. The GCPs are collected at road roundabouts or other distinct features conducive to high-precision measurement in both the imagery and on the ground [3]. Tadono et al. describe the updated plans for sensor calibration and product validation of the Panchromatic Remote-sensing Instrument for Stereo Mapping (PRISM), which is to fly on the Advanced Land Observing Satellite (ALOS). They not only evaluate the geometric accuracy of PRISM data, but also validate the derived DEM [4]. The Finnish Geodetic Institute has maintained a permanent test field for geometric, radiometric, and spatial resolution calibration and the testing of high-resolution airborne and satellite imaging systems in Sjökulla since 1994. The experience of nearly 10 years has shown that the use of gravel, combined with appropriate markers as the control objectives of the test field, can effectively eliminate the effects of seasonal and weather changes. It is also durable and able to guarantee the stability and consistency of the test field [5]. Meguro and Fraser evaluated a stereo pair of pansharpened GeoEye-1 Basic images covering the Tsukuba Test Field in Japan, which contains more than 100 precisely surveyed and image-identifiable GCPs. They indicated that the direct georeferencing accuracy is 2 m (CE90, the circular error of above 90% points) in plane and 3 m (LE90, the line error of above 90% points) in height. The use of a few GCPs improved the geopositioning accuracy to around 0.35 m (0.7 pixel) in plane and 0.7 m (1.4 pixel) in height [6]. John Dolloff, et al. use the Metric Information Network (MIN) method to process all 50 WorldView-1 stereo pairs. Statistics based on 101 ICPs (Independent Check Points) show that the positioning result is 0.5 m in plane and 0.3 m in height [7]. G. Agugiaro et al. evaluated the accuracy of GeoEye-1 and WorldView-2 by control and check data of the Trento test field in Italy. Also, 3D information extraction of the images was mentioned. For reference and validation, a DSM (Digital Surface Model) from airborne LiDAR acquisition is used as a comparison [8]. H. Topan and D. Maktav validated that different variations of point distribution and EOP configuration were preferred, achieving georeferencing accuracies of ~±1 m and ~±5 m at control and check points, respectively [9]. Wang et al. validated that ZY-3 can be used for the generation of cartographic maps at the 1:50,000 scale and for revision and updates of 1:25,000 scale maps [10–14]. By detecting and eliminating various kinds of geometric processing error, including equipment installation error, attitude and orbit measurement error, camera distortion, time synchronization errors and other errors, Li et al. found that the geometric orientation accuracy of Chinese satellite images could be improved to be better than 1.5 pixel, which is higher than the designed accuracy [15]. Tian et al. showed that more accurate and reliable assessment results can be obtained by choosing the appropriate evaluation method of geometric positioning accuracy [16].

Worldwide, scholars have done a lot of geometric accuracy verification work with multiple types of HRSIs. In previous research processes, the evaluation area and evaluation method of each satellite are different. The geometric positioning accuracy of each satellite could only be compared by related reports and papers. A unified test field is hoped to be established and a unified evaluation method is used to evaluate the geometric positioning accuracy of different satellites. The Xianning test field can meet this demand. Data collection, processing, and evaluation processes will become standardized with the Xianning test field, and the accuracy of the evaluation results can be compared more simply and intuitively.

Moreover, the designers of the test field will generally consider satellite geometry calibration and validation work in the same field. The internal and external orientation parameters of the satellite will be updated by the calibration. However, it requires a time lag after calibration in order to ensure the reliability of the accuracy. Therefore, a special validation test field is necessary only for accuracy evaluation using the ICPs (Independent Check Points) in the test field. In addition, this validation test field is different from the calibration test field. The main purpose of the validation test field is to verify the geopositioning accuracy and object recognition capabilities of the standard HRSI, and also to provide a reference for the direct application of the HRSI. The Xianning test field is such a test field for accuracy validation of HRSI or other remote sensing data.

2. Test Field Area and Data Sources

2.1. The Test Field

The test area is located in Xianning, a city of about 2,880,000 inhabitants in the south of Hubei province, central of China. The test field is situated in plain and hilly topography and the elevation ranges from 20 m to 400 m. This topographic feature is representative of flat and hilly land in China. The test field varies from urban areas with residential, industrial and commercial buildings at different sizes and heights, to agricultural or forested areas, and steep rocky surfaces, therefore offering a heterogeneous landscape in terms of geometrical complexity, land use and cover. Also, it needs convenient transportation and to be away from crowded areas in order to ensure that no deformation of the surface features will take place over time.

The area with the GCPs in the test field should contain at least two standard scenes to be able to make the most of the width of whole satellite images within the scope of the test field. Therefore, it is believed that the width of test field should be about 120 km (based on the value of double the current maximum width of the HRSIs in Table 1). A length of the test field of about 100 km along the track direction would be most appropriate; also double the standard length of one HRSI. Currently, the Xianning test field can meet the requirements of the width and length of most mainstream HRSIs. Thumbnail of multiple HRSIs coverage is shown in Figure 1.

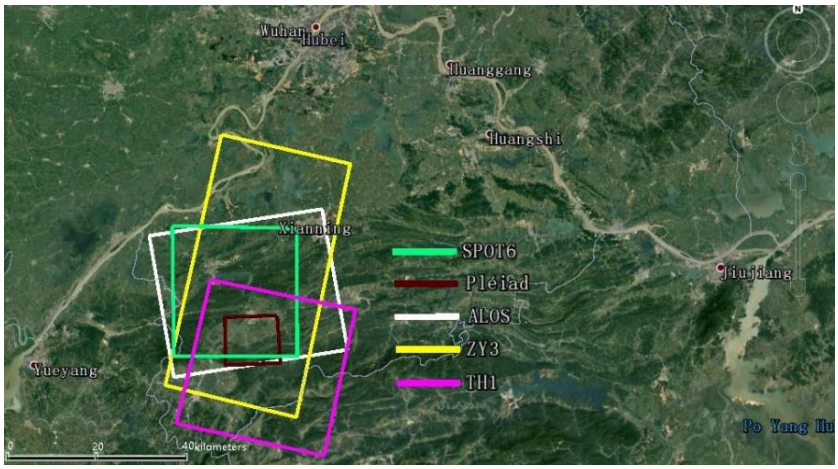

Figure 1. Thumbnail of multiple HRSIs coverage.

2.2. The GCPs

Precision ground control data is the guarantee of geometric accuracy validation of HRSIs. Our group has done related work about GCPs laid in the Xianning region. A total of 118 GCPs are located in the test field as shown in Figure 2. Natural and artificial object feature points are chosen as GCPs by a static GPS field survey. The control points can be evenly distributed in each image, and the accuracy is about 10 cm, which is able to fully meet the needs of control and check points for all types of HRSIs.

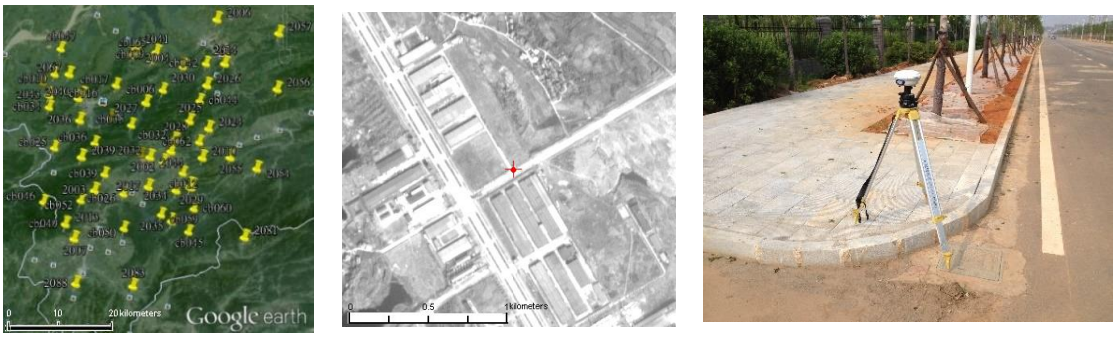

Figure 2. Distribution map of GCPs in the Xianning test filed.

2.3. Multiple HRSIs Data

Our team acquired 5 kinds of HRSIs within the range of the Xianning test filed. The HRSI data are summarized in Table 2, and include:

- **Pleiades**: The processing level is primary product. Primary product is the processing level closest to the natural image acquired by the sensor. This product restores perfect collections: the sensor is placed in rectilinear geometry, and the image is clear of all radiometric distortion. RPCs (Rational Polynomial Coefficients) and the sensor model are provided with the product. The data is a standard image product which includes nadir-forward-backward panchromatic images.
- **SPOT-6**: The processing level is primary product. The image is corrected for radiometric and sensor distortions, using internal calibration parameters, ephemeris and attitude measurements. RPCs and the sensor model are provided with the product. The data is a standard image product which includes nadir-forward-backward panchromatic images.
- **ALOS PRISM**: The processing level is 1B1 product. On the basis of Level 1A, the data with radiometric correction and added absolute calibration coefficient. RPCs and the sensor model are provided with the product. The data is a standard image product which includes nadir-forward-backward panchromatic images.
- **ZY-3**: The processing level is Sensor Corrected, i.e., the images are radiometrically and sensor corrected, but not projected to a plane using a map projection or datum, thus keeping the original acquisition geometry. The images were provided with RPCs. The data is a long strip image product which includes nadir-forward-backward panchromatic images [17].
- **TH-1**: the processing level is 1B; for each image, the RPCs were provided. The images are radiometrically and sensor corrected. The data is a standard image product which includes nadir-forward-backward panchromatic images. Other details about the characteristics of various satellite sensors are listed in Table 2.

Table 2. Characteristics of satellite imagery in the Xianning test field. PAN: panchromatic, GSD: Ground Sample Distance.

Satellite	Pléiades	SPOT-6	ALOS PRISM	ZY3	TH1
Country	France	France	Japan	China	China
Imaging Time	12 July 2013	11 July 2013	27 September 2006	16 February 2013	8 June 2013
Spatial Resolution	Panchromatic: 0.5 m Multispectral: 2 m	Panchromatic: 1.5 m Multispectral: 6 m	Panchromatic: 2.5 m Multispectral: 10 m	Panchromatic: 2.1 m/3.5 m Multispectral: 5.8 m	Panchromatic: 2 m Multispectral: 10 m Three line array: 5 m
Orbit Height	694 km	695 km	692 km	506 km	500 km
Nominal Positioning Accuracy	8.5 m	35 m	50 m	50 m	200 m
Width of Image	20 km	60 km	35 km	50 km	60 km
Side Pendulum Angle	Standard: ±30° Max: ±47°	Standard: ±30° Max: ±45°	±44°	±32°	±32°
Focal Length	12.905 m	6.023 m	1.939 m	1.7 m	2.187 m
Pixel Size	13 μm	13 μm	7 μm	7 μm	8 μm
Data Level	primary product	Standard product	Level 1B1	SC	Level 1B
Base to Height Ratio	0.3	0.4	1	0.88	1
Stereoscopic Mode	Along-track/Across-track	Along-track/Across-track	Along-track/Across-track	Along-track	Along-track
Imaging Mode	Three line array/pushbroom	Three line array/pushbroom	Three line array/pushbroom	Three line array/pushbroom	Three line array/pushbroom

3. General Geometric Processing Model of HRSIs

As seen in Section 2, all HRSIs are provided with RFM (Rational Function Model). Toutin and Teo's study has shown that the result of satellite image orientation based on the RFM is almost as accurate as that based on the rigorous geometric model [18,19]. Additionally, the RFM has a simple form and leads to fast computations, so the orientation selects the RFM as the geometric model. The RFM describes the relations between the image point coordinates (r_n, c_n) and the ground point coordinates (X_n, Y_n, Z_n), which have the following general form [20]:

$$\begin{cases} r_n = \frac{p_1(X_n,Y_n,Z_n)}{p_2(X_n,Y_n,Z_n)} \\ c_n = \frac{p_3(X_n,Y_n,Z_n)}{p_4(X_n,Y_n,Z_n)} \end{cases} \tag{1}$$

where (r_n, c_n) are measured line and sample coordinates of the nth image point, corresponding to the ground point with the object space coordinates (X_n, Y_n, Z_n), which are the variables of a polynomial p_i $(i = 1, 2, 3, 4)$, whose degree should not exceed three. For example, the form of the polynomial p_i is

$$\begin{aligned} p_i = {} & a_{i0} + a_{i1}Z + a_{i2}Y + a_{i3}X + a_{i4}ZY + a_{i5}ZX + a_{i6}YX + a_{i7}Z^2 + a_{i8}Y^2 + a_{i9}X^2 + a_{i10}ZYX + \\ & a_{i11}Z^2Y + a_{i12}Z^2X + a_{i13}Y^2Z + a_{i14}Y^2X + a_{i15}ZX^2 + a_{i16}YX^2 + a_{i17}Z^3 + a_{i18}Y^3 + a_{i19}X^3 \end{aligned} \tag{2}$$

where $a_{ij}(i = 1, 2, 3, 4,\ j = 0,\ 1, \cdots, 19)$ are rational polynomial coefficients [20].

Furthermore, bias compensation is needed. Previous studies have shown that the affine model combined with RFM can eliminate the systematic errors in the image points, which improves the geometry processing accuracy [11]. Therefore, we modify the relationship between the image coordinates (x, y) and the coordinates (X, Y, Z) according to Formula (3) [21].

$$\begin{cases} x + a_0 + a_1x + a_2y = \frac{P_1(X,Y,Z)}{P_2(X,Y,Z)} \\ y + b_0 + b_1x + b_2y = \frac{P_3(X,Y,Z)}{P_4(X,Y,Z)} \end{cases} \tag{3}$$

The affine transformation parameters $(a_0, a_1, a_2, b_0, b_1, b_2)$ are set as orientation parameters. It can be solved with a small number of GCPs.

4. Validation of Geometric Accuracy for HRSIs

The test is expected to demonstrate to what extent direct georeferencing and sensor orientation are accurate and efficient methods for the determination of the exterior orientation parameters for topographic mapping. Currently, such assessments are performed through the validation technique known as the Hold-Out Validation (HOV) method [22]. It is also known as test sample estimation. According to this, the data set (known ground points) is partitioned into two subsets: the first one is used in the orientation model (GCPs—Ground Control Points) and the second one is used to validate the model itself (ICPs—Independent Check Points).

4.1. Orientation Accuracy with Single Image

The image orientation determines the relation between the object and the image coordinates, which is dependent on the image product and the imaging mode. So at least for reliability, GCPs are required. The image orientation can be based on a geometric reconstruction of the imaging geometry, depending upon the available information. The direct sensor orientation may be available, too, as a sensor-oriented RPC. Like the geometric reconstruction, this can be improved by GCPs, named and also bias corrected [21].

The orientation accuracy was analyzed and verified based different schemes of laid GCPs, as follows in Table 3:

Table 3. Orientation accuracy of HRSIs.

Satellite	Number of GCP	Number of ICP	RMSE of GCP (Pixels)			RMSE of ICP (Pixels)		
			x	*y*	Plane	*x*	*y*	Plane
Pleaides	0	21	-	-	-	2.300	1.344	2.664
	4	17	0.768	0.082	0.772	0.929	1.322	1.591
	9	12	1.370	0.700	1.538	0.760	0.891	1.172
SPOT6	0	26	-	-	-	1.655	2.556	3.045
	4	22	0.381	0.166	0.415	1.121	0.821	1.390
	9	17	0.876	0.357	0.946	1.217	0.817	1.466
ALOS	0	11	-	-	-	2.193	3.943	4.511
	4	7	0.300	0.404	0.503	0.972	0.703	1.199
	9	2	0.768	0.560	0.951	0.337	0.698	0.775
ZY-3	0	38	-	-	-	6.342	1.180	6.451
	4	34	0.362	0.175	0.402	0.872	1.160	1.451
	9	29	0.546	0.479	0.726	0.853	1.123	1.410
TH-1	0	17	-	-	-	6.413	2.158	6.766
	4	13	0.444	0.049	0.447	0.591	1.622	1.726
	9	8	0.493	1.100	1.205	0.639	1.467	1.600

It can be seen that Pleaides and SPOT6 performed with the highest accuracy without GCPs, almost reaching the 3 pixel level, from Table 3. The results of ZY-3 and TH-1 are almost the same, reaching about 6 pixels. When 4 GCPs were laid in the four corners, ZY-3, SPOT6 and Pleaides all reached the 1.5 pixel level or better. However, residuals of some points in the TH-1 image were still large after orientation with GCPs. The interior geometric accuracy of TH-1 is poor, as can be seen from the residuals distributions in Figure 3. More GCPs were added, but no more obvious changes occurred. Therefore, the scheme with 4 GCPs located in each corner is recommended for HRSI orientation. Residual distribution figures are shown below in Figures 4–8:

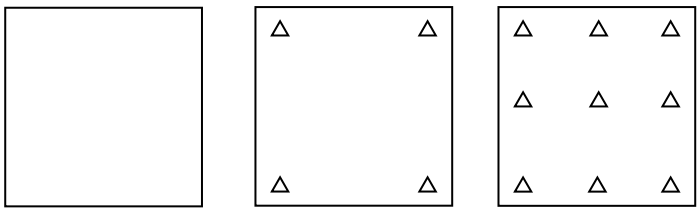

(0GCP) **(4GCP)** **(9GCP)**

Figure 3. GCP scheme.

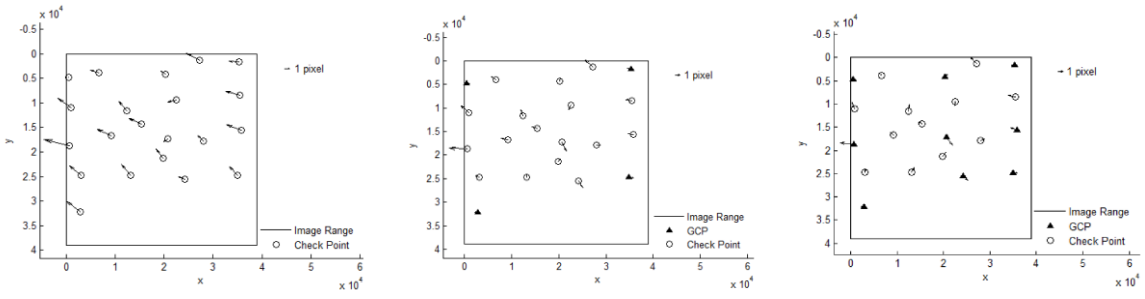

(0GCP) **(4GCP)** **(9GCP)**

Figure 4. Residual distributions of check points of orientation for Pleaides.

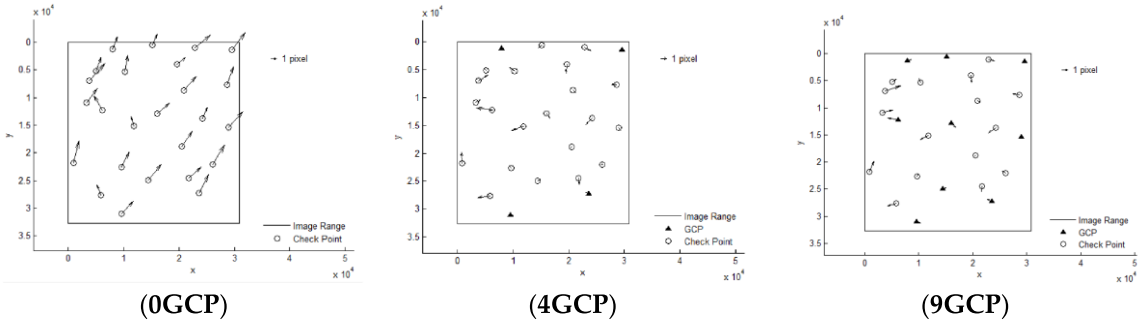

Figure 5. Residual distributions of check points of orientation for SPOT6.

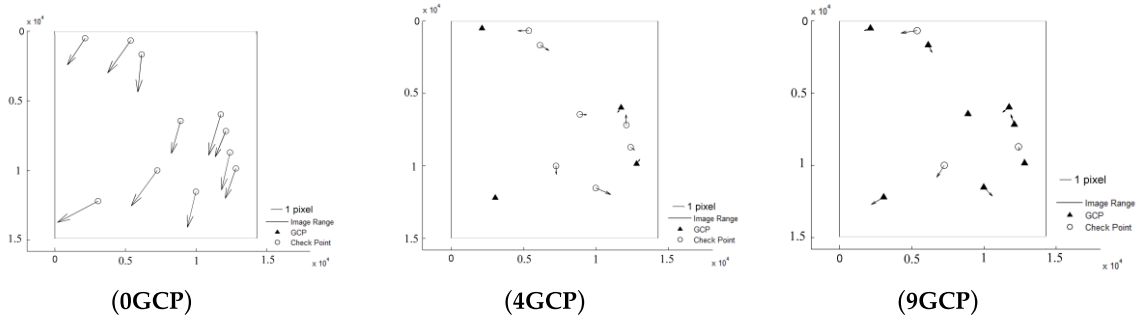

Figure 6. Residual distributions of check points of orientation for ALOS.

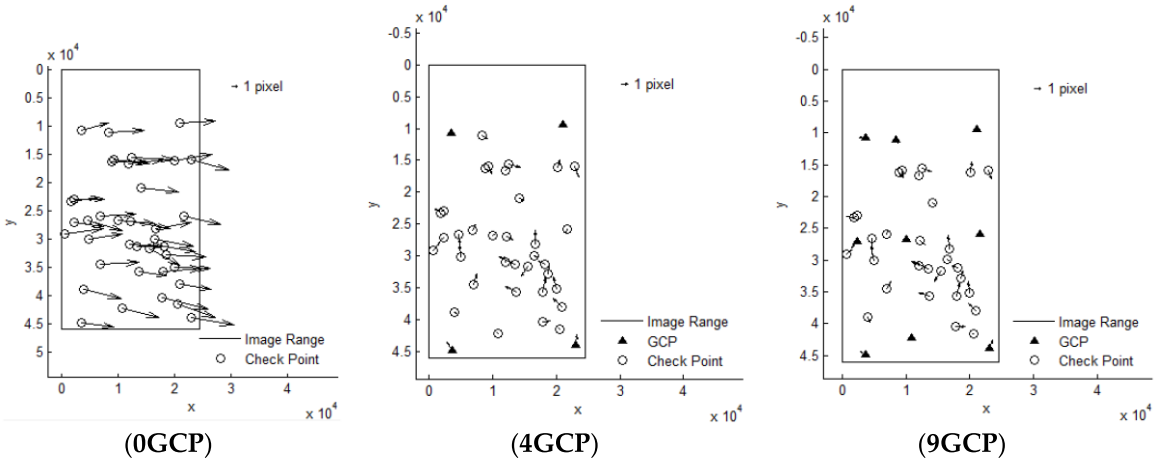

Figure 7. Residual distributions of check points of orientation for ZY-3.

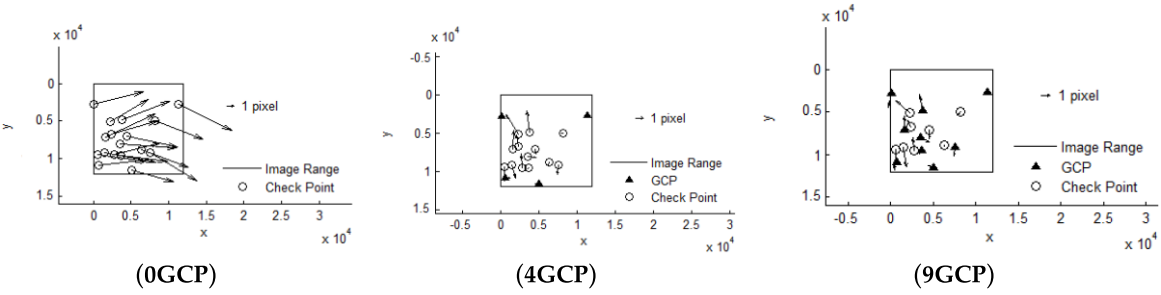

Figure 8. Residual distributions of check points of orientation for TH-1.

4.2. Orientation Accuracy of Block Adjustment with Tri-Stereo Images

All these HRSIs are able to constitute a three linear array stereo model with nadir-forward-backward images. In consideration of the multi-covered image data with redundant observations information, block adjustment was carried out with and without GCPs to evaluate the orientation accuracy. Conclusive results are as follows:

From Table 4 it can be seen that in the situation of no GCP, Pleaides reached an accuracy of 0.860 m in plane and 2.654 m in height, which is really unbelievable, although the 0.5 m GSD (Ground Sampling Distance) of Pleaides is the highest among the HRSIs. SPOT6 reached an accuracy of 5.336 m in plane and 4.595 m in height, and also has a superior performance in geometric accuracy without GCP. The block adjustment accuracy without GCP of Pleaides and SPOT6 meet the requirements for 1:50,000 Topographic maps. However, ALOS, ZY-3 and TH-1 cannot reach that level.

Table 4. Accuracy of block adjustment for HRSIs.

Satellite	Number of GCP	Number of ICP	RMSE of GCP (m)				RMSE of ICP (m)			
			x	*y*	Plane	Height	*x*	*y*	Plane	Height
Pleaides	0	21	-	-	-	-	0.588	0.628	0.860	2.654
	4	17	0.123	0.044	0.130	1.977	0.510	0.445	0.677	1.505
	9	12	0.574	0.340	0.667	1.530	0.403	0.395	0.564	1.377
SPOT6	0	26	-	-	-	-	3.362	4.144	5.336	4.595
	4	22	0.121	0.329	0.351	0.917	1.842	1.169	2.182	2.129
	9	17	1.231	0.480	1.321	2.209	2.006	1.309	2.396	2.294
ALOS	0	16	-	-	-	-	8.677	31.588	32.758	11.832
	4	12	1.639	1.489	2.214	0.717	1.655	2.381	2.900	1.363
	9	7	1.263	1.393	1.880	1.326	1.681	3.208	3.621	2.125
ZY-3	0	38	-	-	-	-	12.818	4.263	13.508	11.528
	4	34	0.030	0.289	0.291	0.259	1.565	2.142	2.653	1.858
	9	29	0.355	0.257	0.438	1.442	1.640	2.356	2.870	1.937
TH-1	0	32	-	-	-	-	29.095	15.089	32.775	12.228
	4	28	0.001	0.001	0.001	0.001	8.703	14.780	17.152	7.467
	9	23	0.687	4.306	4.361	1.900	4.770	8.674	9.899	5.028

From Table 4 it can also be seen that in the situation with GCPs, when four GCPs were laid in the four corners, the block adjustment accuracy of ZY-3 reaches 2.653 m in plane and 1.858 m in height, and ALOS reaches 2.900 m in plane and 1.363 m in height. Compared to the accuracy without GCP, this accuracy is improved a lot, reaching the level of SPOT6, with the accuracy in height being even better. Pleaides still has the best performance, while TH-1 has the worst performance, reaching 17.152 m in plane and 7.467 m in height, although its resolution of 5 m is the lowest. Under the condition of setting the GCPs in the four corners, without consideration of artificial pricking points, the accuracy almost reaches the best level for single image orientation and for block adjustment. The accuracy undergoes no more changes, even when more GCPs are added. Therefore, four GCPs laid in the corners is a good layout scheme, which is recommended.

From another point of view, if a satellite image cannot achieve an accuracy of 1–2 pixels with four GCPs laid, it can be shown that the internal geometric distortion has not been eliminated before the generation of standard image products. For satellite images without internal geometric distortion, the four GCPs laid can eliminate most of the errors and achieve high-precision positioning.

5. Conclusions

Different from the traditional methods of verification, the paper has embarked on a unified test investigating sensor orientation and describes the processing carried out on ZY-3, TH-1, ALOS, SPOT6 and Pleaides in a geometric accuracy test field, instead of verifying them separately. All the results are compared under conditions both without and with GCPs, and whether in orientation with single image or in block adjustment. The performance of Pleaides is the best. SPOT6, ALOS and

ZY-3 are almost comparable, although the ground resolution of SPOT6 is slightly higher than that of ZY-3. The performance of TH-1 is a little worse. A layout scheme of four GCPs laid in the corners is recommended, and can be used for geometric precision processing and evaluation of HRSIs.

Also, the test field set up in Xianning is presented with the aim of investigating spaceborne optical imagery. The reason for choosing the Xianing area as the test field is explained in detail, and the function of the Xianning test field is also illustrated for the geometric accuracy validation of HRSIs. The test field will undoubtedly be important both for development, analysis, and simulation of platforms and sensors in the future. In addition, verification work of the HRSI data obtained will continue to be carried out.

Author Contributions: Conceptualization, X.Z. and T.W.; Methodology, J.W.; Validation, Q.H., and J.W.; Formal Analysis, X.Z. and T.W.; Writing-Original Draft Preparation, Q.H.; Writing-Review & Editing, Q.H.; Supervision, G.Z.

Funding: This research was supported by, Key research and development program of Ministry of Science and Technology (2016YFB0500801, 2018YFB0504905), Quality improvement of Chinese satellite data and comprehensive application demonstration of Geology and mineral resources, National Natural Science Foundation of China (Grant No. 91538106, Grant Nos. 41501503, 41601490, 41501383), China Postdoctoral Science Foundation (Grant No. 2015M582276), Hubei Provincial Natural Science Foundation of China (Grant No. 2015CFB330), Open Research Fund of State Key Laboratory of Information Engineering in Surveying, Mapping and Remote Sensing (Grant No. 15E02), Open Research Fund of State Key Laboratory of Geo-information Engineering (Grant No. SKLGIE2015-Z-3-1), Fundamental Research Funds for the Central University (Grant No. 2042016kf0163), Special Fund for High Resolution Images Surveying and Mapping Application.

Acknowledgments: The authors would like to thank the editors and the anonymous reviewers for their constructive suggestions.

Conflicts of Interest: The authors declare no conflict of interest.

References

1. Komus, W.; Lehner, M.; Blechinger, F.; Putz, E. Geometric calibration of the stereoscopic CCD-line-scanner MOMS-2P. *Int. Arch. Photogramm. Remote Sens.* **1996**, *31*, 90–98.
2. Komus, W.; Lehner, M.; Schroeder, M. Geometric in-flight calibration of the stereoscopic CCD-line-scanner MOMS-2P. *ISPRS J. Photogramm. Remote Sens.* **2000**, *55*, 59–71.
3. Fraser, C.; Hanley, H.; Yamakawa, T. Three-Dimensional Geopositioning Accuracy of Ikonos Imagery. *Photogramm. Rec.* **2002**, *17*, 465–479. [CrossRef]
4. Tadono, T.; Shimada, M.; Watanabe, M.; Hashimoto, T.; Iwata, T. Calibration and validation of PRISM onboard ALOS. *Int. Arch. Photogramm. Remote Sens. Spat. Inf. Sci.* **2004**, *35*, 13–18.
5. Honkavaara, E.; Peltoniemi, J.; Ahokas, E.; Kuittinen, R.; Hyyppä, J.; Jaakkola, J.; Kaartinen, H.; Markelin, L.; Nurminen, K.; Suomalainen, J. A Permanent Test Field for Digital Photogrammetric systems. *Photogramm. Eng. Remote Sens.* **2008**, *74*, 95–106. [CrossRef]
6. Meguro, Y.; Fraser, C.S. Georeferencing accuracy of Geoeye-1 stereo imagery: Experiences in a Japanese test field. *Int. Arch. Photogramm. Remote Sens. Spat. Inf. Sci.* **2010**, *38*, 1069–1072.
7. Dolloff, J.; Settergren, R. Worldview-1 stereo extraction accuracy without MIN processing. In Proceedings of the ASPRS 2010 Annual Conference, San Diego, CA, USA, 26–30 April 2010.
8. Agugiaro, G.; Poli, D.; Remondino, F. Testfield Trento: Geometric evaluation of very high resolution satellite imagery. *Int. Arch. Photogramm. Remote Sens. Spat. Inf. Sci.* **2012**, *39*, B8. [CrossRef]
9. Topan, H.; Maktav, D. Efficiency of Orientation Parameters on Georeferencing Accuracy of SPOT-5 HRG Level-1A Stereoimages. *IEEE Trans. Geosci. Remote Sens.* **2014**, *52*, 3683–3694. [CrossRef]
10. Wang, T.Y.; Zhang, G.; Li, D.R.; Tang, X.M.; Jiang, Y.H.; Pan, H.B.; Zhu, X.Y.; Fang, C. Geometric accuracy validation for ZY-3 satellite imagery. *IEEE Geosci. Remote Sens. Lett.* **2014**, *11*, 1168–1171. [CrossRef]
11. Wang, T.; Zhang, G.; Li, D.; Tang, X.M.; Jiang, Y.H.; Pan, H.B.; Zhu, X.Y. Planar Block Adjustment and Orthorectification of ZY-3 Satellite Images. *Photogramm. Eng. Remote Sens.* **2014**, *80*, 559–570. [CrossRef]
12. Zhang, G.; Wang, T.Y.; Li, D.; Tang, X.; Jiang, Y.H.; Huang, W.C.; Pan, H. Block adjustment for satellite imagery based on the strip constraint. *IEEE Trans. Geosci. Remote Sens.* **2015**, *53*, 933–941. [CrossRef]

13. Pan, H.; Tao, C.; Zou, Z. Precise georeferencing using the rigorous sensor model and rational function model for ZiYuan-3 strip scenes with minimum control. *ISPRS J. Photogramm. Remote Sens.* **2016**, *119*, 259–266. [CrossRef]
14. Pan, H. Geolocation error tracking of ZY-3 three line cameras. *ISPRS J. Photogramm. Remote Sens.* **2017**, *123*, 62–74. [CrossRef]
15. Li, D.; Zhang, G.; Jiang, Y.; Shen, X. Research on image geometric precision of domestic optical satellites. *Spacecr. Eng.* **2016**, *25*, 1–9.
16. Tian, G.; Huang, Q.; He, H.; Xia, Z. Analysis on Geometric Positioning Accuracy Evaluation of Remote Sensing Satellite Image. *Spacecr. Recovery Remote Sens.* **2017**, *38*, 106–112.
17. Pan, H.; Zhang, G.; Tang, X.; Li, D.; Zhu, X.; Zhou, P.; Jiang, Y. Basic Products of the ZiYuan-3 Satellite and Accuracy Evaluation. *Photogramm. Eng. Remote Sens.* **2013**, *79*, 1131–1145. [CrossRef]
18. Toutin, T. Comparison of 3D physical and empirical models for generating DSMs from stereo HR images. *Photogramm. Eng. Remote Sens.* **2006**, *72*, 597–604. [CrossRef]
19. Teo, T.-A. Bias compensation in a rigorous sensor model and rational function model for high-resolution satellite images. *Photogramm. Eng. Remote Sens.* **2011**, *77*, 1211–1220. [CrossRef]
20. Tao, C.V.; Hu, Y. A comprehensive study of the rational function model for photogrammetric processing. *Photogramm. Eng. Remote Sens.* **2001**, *67*, 1347–1357.
21. Fraser, C.S.; Hanley, H.B. Bias compensation in rational functions for IKONOS satellite imagery. *Photogramm. Eng. Remote Sens.* **2003**, *69*, 53–57. [CrossRef]
22. Brovelli, M.A.; Mattia, M.; Fratarcangeli, F.; Giannone, F.; Realini, E. Accuracy assessment of high resolution satellite imagery orientation by leave-one-out method. *ISPRS J. Photogramm. Remote Sens.* **2008**, *63*, 427–440. [CrossRef]

Ore Geology Reviews xxx (xxxx) xxx–xxx

Contents lists available at ScienceDirect

Ore Geology Reviews

journal homepage: www.elsevier.com/locate/oregeorev

Potential of Sentinel-2 data for alteration extraction in coal-bed methane reservoirs

Li Chen[a,*], Xiucheng Yang[b], Guangwei Zhen[c]

[a] China Areo Geophysical Survey and Remote Sensing Center for Land and Resources, China
[b] ICube Laboratory, University of Strasbourg, France
[c] Sinomine Resource Exploration Company Limited, China

ARTICLE INFO

Keywords:
Sentinel-2 data
Hyperion data
Hydrocarbon micro-seepage
Alteration extraction
Coal-bed methane reservoirs

ABSTRACT

This study illustrates the potential of alteration extraction in coal-bed methane (CBM) reservoirs using the recently available Sentinel-2 data. This study then evaluates the capabilities for mapping the altered minerals and vegetation. In the alteration mapping process, we separately analyzed the key remote sensing signatures of altered minerals and geobotanical anomalies based on the hydrocarbon micro-seepage theory. The diagnostic spectral characteristics of irons, clays and altered vegetation were concentrated and demonstrated the distribution of hydrocarbon micro-seepage. In the bare soil region, the altered minerals, including irons and clays were extracted through band math and principal component analysis (PCA) methods. In the vegetation area mapping, the diagnostic spectral feature parameters, such as the locations and slopes of three feature edges, were calculated. In addition, the mapping accuracy was assessed based on the extraction results of Hyperion data through full spectral profile matching method and the X-ray diffraction (XRD) analysis results. The results show that: 1) compared with band math and PCA methods, the different extraction methods were suitable for different minerals; 2) the extraction results of iron and clay minerals were most accurate (78.33% and 76.67%, respectively) with XRD analysis; 3) the highest rate of change of the feature edge slope was up to 39% with a reference spectrum; and 4) the distribution of alteration information was consistent with the Hudi coal mining area in Jincheng, Shanxi province. The potential geological application of Sentinel-2 data was revealed to identify the direction of CBM exploration in a large scale, highly efficient, convenient, and inexpensive way.

1. Introduction

As the world's alternative energy resources, coal-bed methane (CBM) is a form of unconventional and natural gas generated in coal beds (Sircar, 2000; Ayers, 2002; Fu et al., 2009). CBM consists mainly of methane (more than 90%), some carbon dioxide and nitrogen, and several heavier hydrocarbons, such as propane or butane. CBM has recently become an important source of energy in many countries. Furthermore, CBM which is emitted into atmosphere in quantity during coal production, can not only cause the waste of resources, but also pollute the environment. The global explorations of CBM have a huge impact on lessening the energy crisis and alleviating environmental pollution (Yao et al., 2009; Moore, 2012). Traditional drilling and geophysical prospecting methods use logging, gravity, electromagnetic and seismic technology as bases. These methods are time-consuming, cost-intensive, and unsuitable for certain field conditions due to their use of large and heavy equipment. However, utilizing the current remote sensing technique in exploring CBM resources allows a synoptic view in geology that evaluates extensive areas at a low cost and with reduced field-work (Lammoglia and Filho, 2012).

Specifically, remote sensing imagery can identify structure, lithology, and landscape features, including lineaments, rocks composition, and drainage at a large-scale region, by considering differences in tone, shape, and spectral–mineralogical information. Until now, the spectral characteristics of different minerals and rocks had been examined in the visible-near infrared bands (Hunt and Ashley, 1979). For most kinds of rocks, such as mafic, granodiorite, and quartz rocks, the rock alterations are usually identified and comparatively analyzed through band math and principal component analysis (PCA) methods using ETM and ASTER (Advanced Spaceborne Thermal Emission and Reflectance Radiometer) imagery in the bare soil region based on the spectral absorption characteristics of altered minerals (Crosta and Moore, 1989; Tangestani and Moore, 2001; Pour and Hashim, 2012; Gu et al., 2015; Gu and Sheng, 2016; Rajendran and Nasir, 2017; Liu et al., 2017). Although the precise content of the mineral was still difficult to extract, the remote sensing method could supply a seamless mineral

* Corresponding author.
E-mail addresses: chenlixyz@163.com (L. Chen), xiucheng.yang@etu.unistra.fr (X. Yang), fengyue-zhen@163.com (G. Zhen).

http://dx.doi.org/10.1016/j.oregeorev.2017.10.009
Received 28 February 2017; Received in revised form 14 August 2017; Accepted 12 October 2017

Please cite this article as: Chen, L., Ore Geology Reviews (2017), http://dx.doi.org/10.1016/j.oregeorev.2017.10.009

map (Souza Filho and Drury, 1998; Ducart et al., 2006; Zheng et al., 2015; Qin et al., 2016). Furthermore, the remote sensing data had been improved to extract oil and gas, provide accurate altered information, enhance the effects of estimation, and significantly decrease the exploration risks. With the narrow bandwidths and high-spectral band, hyperspectral remote sensing data can be applied to identify and extract alteration minerals through the distinct absorption features of most minerals (Vane and Goetz, 1993; Chen et al., 2012; Xia et al., 2016; Zhou et al., 2017).

Micro-seepage, wherein a natural hydrocarbons escape slowly from a subsurface source, is the foundation of oil and gas exploration that utilizes remote sensing technology. Approximately 80% of the world's oil basin has micro-seepage, except for those with unfractured seals (Clarke and Cleverly, 1991). 89% of drilling on exploration is associated with a micro-seepage anomaly in discoveries (Schumacher, 1996). Micro-seepage theory was used to identify the potential oil and gas reservoirs based on the diagnostic spectral features of alteration anomalies through remote sensing methods or by integrating them with interpretations from other materials, including geological, geochemical and geophysical data (Hörig et al., 2001; Van der Meer et al., 2002; Kühn et al., 2004; Van Der Werff et al., 2006; Fu et al., 2007; Lyder et al., 2010; Van der Meer et al., 2012). Studies using the above-mentioned detection methods showed that hydrocarbons generally accumulated along fault areas and structurally controlled drainage, and several reservoirs, such as the Gulf of Mexico and Brazil, were identified in the history of the petroleum industry (Almeida-Filho et al., 2002). However, few studies have used the remote sensing method to extract hydrocarbon anomalies in the CBM reservoirs.

The objective of the present study is to evaluate the potential of Sentinel-2 imagery for extracting hydrocarbon alteration anomalies in CBM reservoirs through the following means: (1) establishing extraction algorithms to produce hydrocarbon prospective maps using Sentinel-2 data in the Southern Qishui Basin; (2) extracting the alteration anomalies through Sentinel-2 and Hyperion images in bare soil regions and vegetation areas, respectively; (3) comparing the extraction results of Sentinel-2 data and Hyperion imagery using the different algorithms; and (4) verifying the results using the measured spectral, sample and geological data in the field.

2. Study areas and dataset

2.1. Geological background of the study area

The Qinshui Basin, located in southeast of Shanxi Province, China, covers 2922 km^2 and is divided into three parts: Fanzhuang, Panzhuang and Zhengzhuang. The CBM resource in Qinshui Basin is estimated to contain 3.28×10^{12} m^3 of gas (Wang et al., 2014). Thus, the Qinshui Basin deserves commercial CBM exploration and exploitation. The study area (35°39′N–35°50′N, 112°29′E–112°46′E) lies in the southern Qinshui Basin in Hudi City as shown in Fig. 1(a).

2.1.1. Stratum and lithology

The stratigraphic structure of the study area can be divided into seven groups from top to bottom: Quaternary (Q), the Upper Permian Shihezi Formation (Fm.), the Lower Permian Shihezi Fm., the Lower Permian Shanxi Fm., the Upper Carboniferous Taiyuan Fm., the Upper Carboniferous Benxi Fm. and the Middle Fengfeng Fm. Meanwhile, Taiyuan Fm. and the Shanxi Fm. are the main coal-bearing strata, with an average thickness of 150 m. Given the continental-oceanic interaction environment in the Taiyuan Fm. As well as the delta and fluvial environments in the Shanxi Fm., the lake plain, blocked channel, and delta plain become conducive for the formation of coal (Wang et al., 2014). However, the coal formed in the lagoon and gulf environments is low quality in the Benxi Fm.

The study area mainly developed mudstone, sandy mudstone, sandstone, siltstone, argillaceous siltstone and limestone. Kaolinite (clay mineral) and calcite (carbonate) are the main component of mudstone and limestone respectively. In particular, the relative contents of the clay minerals reached 50% in the argillaceous rocks. Based on the recent geological researches, the irons, carbonates and clay minerals indicated the reducing environment which generated by hydrocarbon micro-seepage were widely distributed in the study area. Therefore, the irons, carbonates and clay minerals, such as siderite, calcite, montmorillonite and kaolinite, were considered as the indicatory minerals for the alteration extraction by remote sensing technique.

2.1.2. Tectonics

The study area is located at the Fanzhuang coal district in the Qinshui Basin which distinct from the North China Craton Basin as a separate and complex dual syncline. There are only a few faults and folds with an axial strike of NNE–SSW and near N-S, such as Sitou fault, Guxianhe fault and Dongshanling fault (Fig. 1(b)). Specifically, the Sitou fault located the northwestern study area is a tenso-shear normal fault, with a strike of 30° NE and a dip angle of 70°. This fault is 350 m wide and the length is about 10 km. As the important boundary of groundwater in the study area, the Sitou fault deeply influenced the formation and migration of the CBM.

2.1.3. Coal seam

The total thickness of coal-bearing strata is 144 m, which contain twelve coal seams in the study area. The detailed information of two key coal seams about micro-seepage is shown in Table 1.

The main CBM reservoirs are distributed in the 3# and 15# coal seam that belong to the Lower Permian Shanxi Fm. and the Upper Carboniferous Taiyuan Fm., respectively. The average thickness of 3#

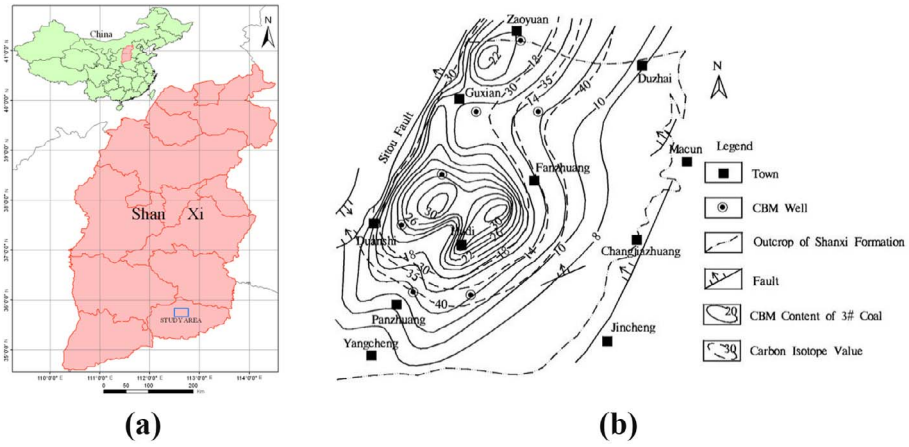

Fig. 1. (a) Location map of study area in the Shanxi province, China; (b) Distribution of the coal-bearing stratum, fault, well and CBM content in study area (Zhang et al., 2015).

Table 1
Introduction of two key coal seams about micro-seepage.

No.	Coal-bearing strata	Coal seam thickness/m	Coal seam depth/m	Gas content/(m^3/t)	Texture of coal seam	Roof and floor lithology
3#	Shanxi formation	4.10–6.815.60	430–770	9–32.019	simple and stabile	roof lithology: mudstone and siltstone; floor lithology: mudstone and sandy mudstone
15#	Taiyuan formation	2.20–5.70 3.24	unmined	8–25.615.8	simple and stabile	roof lithology: limestone; floor lithology: mudstone and sandstone

and 15# coal seams is about 3 m and 6 m, respectively, and their burial depth range is approximately 400 m to 800 m.

2.2. Dataset and pre-processing

2.2.1. Sentinel-2 data

As part of the European Copernicus program, the European Space Agency (ESA) successfully launched the Sentinel-2A satellite, which armed to provide high spatial resolution optical observations over global land surfaces, on 23 June 2015 (Donlon et al., 2012).

Sentinel-2 satellite carries a wide-swath, high-spatial resolution and a multi-spectral imager (MSI). Moreover, it has 13 spectral bands spanning from the visible (VIS) and the near infrared (NIR) to the short wave infrared (SWIR) (433–2190 nm) (Table 2) (Drusch et al., 2012). Due to the bands of the 10 and 20 m spatial resolution utilized in this study, the bands of 20 m spatial resolution needs to be resampled to 10 m by nearest neighbor method.

Sentinel-2 possesses the following advantages: (1) a wide coverage, that is, a wide swath that is approximately 290 km (20.6° field-of-view from an altitude of 786 km) (Malenovský et al., 2012); (2) a high resolution, i.e., a spatial resolution of up to 10 m; (3)novel spectral bands, wherein the three red-edge bands are added especially for vegetation-related applications; (4) its short revisit frequency provides a global coverage every five days using the Sentinel-2B sensor launched on 7 March 2017; and (5) free access. Given the unprecedented specifications above, Sentinel-2 imagery has been widely used in land and land cover mapping (Schuster et al., 2012), forest stress monitoring (Eitel et al., 2011), built-up areas mapping (Pesaresi et al., 2016; Yang and Chen, 2017), water detection (Du et al., 2016)and biophysical variable retrieval (Verrelst et al., 2012; Clevers and Gitelson, 2013).

Sentinel-2 Level-1C product (relative orbit: R075) comprises 100 km × 100 km tiles in the UTM/WGS84 projection and provides top-of-atmosphere (TOA) reflectance (Sibanda et al., 2015). In this paper, the Sentinel-2 MSI image which acquired on June 22, 2016 was downloaded from the Copernicus Open Access Hub's website (https://scihub.copernicus.eu/). It was of high quality, cloudless (1.32%), and had produced radiometric and geometric corrections, such as orthorectification and spatial registration on a global reference system with sub-pixel accuracy (Sibanda et al., 2015). Hence, the pre-processing only required the following steps: (1) precise geometric correction that improved the geographical coordinates accurately using a topographic map (1: 50 000); (2) mosaic imaging and masking to obtain the study area image and compare it with Hyperion data centered at 35°43′29″N, 112°36′29″E; (3) image enhancement which mainly included linear and contrast stretching of a single band, band ratios, false color composites (FCC), and PCA. The sentinel-2 imagery of the study area was covered by vegetation, built-up areas, and water bodies and is shown in Fig. 2(a).

Table 2
Sentinel-2 spectral bands definition and spatial resolution.

Band number	Central wavelength /nm	Spatial resolution/m	Band number	Central wavelength /nm	Spatial resolution/m
1	443	60	8	842	10
2	490	10	8a	865	20
3	560	10	9	945	60
4	665	10	10	1380	60

2.2.2. Hyperion data

The other hyperspectral data in this paper are provided by the space-borne hyperspectral sensor, Hyperion, on the National Aeronautics and Space Administration (NASA) Earth Observer-1 (EO-1) satellite (Landgrebe et al., 2001), which is a push broom imaging spectrometer launched in November 2000. Moreover, it has 242 bands covering the VIS, NIR, and SWIR regions at 10 nm spectral sampling intervals with a 30 m spatial resolution. Specifically, the NIR and SWIR bands are the most useful wavelength regions for spectral signature extraction, making Hyperion data highly suitable for identifying alteration minerals (Hunt and Salisbury, 1970; Hubbard et al., 2003).

The good-quality Hyperion data (path/row: 125/35) in this study were acquired from the study area on October 6, 2014, with approximately 9% cloud cover. To correct the sensor artifacts and the atmospheric and geometric effects, the Hyperion data underwent the following pre-processing steps (Kruse et al., 2003; Ren et al., 2014): (1) remove invalid and useless bands that were uncalibrated and strongly affected by water vapor and noise and further analyze the 152 bands of the final dataset; (2) fix the bad lines caused by the functional failure of a single detector element through the average of the neighbor lines; (3) perform destriping using the global destriping technique to eliminate the systematic noise and the striping in the Hyperion image; (4) reduce noise using the Savitzky-Golay Filter method; (5) execute atmospheric correction using FLAASH tools provided by ENVI 5.3; (6) perform geometry calibration using a second-order polynomial corresponding to the Sentinel-2 image. To compare with extraction results between Sentinel-2 and Hyperion data, the spatial resolution of Hyperion data needs to resample from 30 m to 10 m. The true color composite image is shown in Fig. 2(b). Flowchart of Hyperion data processing steps is shown in Fig. 3. In order to analyze the quality of Hyperion data and make sure that the date is useful for alteration mineral extraction, the SNR of Hyperion data used have been calculated in our pervious works (Zhang et al., 2015). Compared with the precious studied (Gersman et al., 2008; Green et al., 2003), our estimated results gave a well consistency.

2.2.3. Field spectral data

Aside from the above image data, the systematic fieldwork was executed at the study area in September 2014. The different types of rock, vegetation, and soil were considered as field samples, and all spectral measurements adjoining the CBM were taken under cloudless conditions between 10:00 and 14:00 using the ASD FieldSpec FP spectrometer (Analytical Spectral Devices, Boulder, CO. USA). The spectrometer was fitted with a 25° field-of-view and was operated in the wavelength ranging from 350 nm to 2500 nm, with sampling intervals of 3 or 8 nm. Reflectance spectra were measured through calibration with a standardized white panel. A panel radiance measurement was taken before each measurement. Each sample was measured five times, and the average value was calculated afterwards. The 200 samples near the CBM well were scanned in the study area. Aside from the abnormal spectral data, 50 samples of reference spectra were collected from

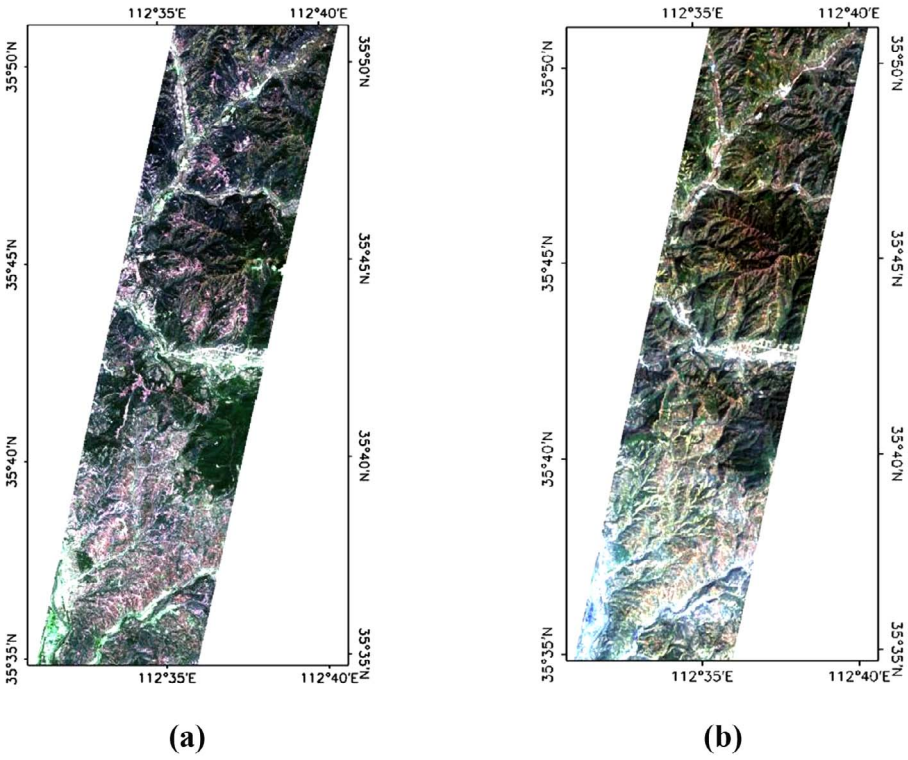

Fig. 2. Two true color composite images after the pre-processing procedure: (a) Sentinel-2 image (band 4, 3, and2 in RGB); (b) Hyperion image (band 31, 21 and14 in RGB).

Jiafeng town, far from the CBM enrichment region, for an analysis and comparison of the abnormal spectral.

To enhance the spectral characteristics, the pre-processing of acquired spectra was necessary to obtain more information about hydrocarbon micro-seepage based on the View SpecPro. The noise from the instrument and in the in-situ environment was reduced through the

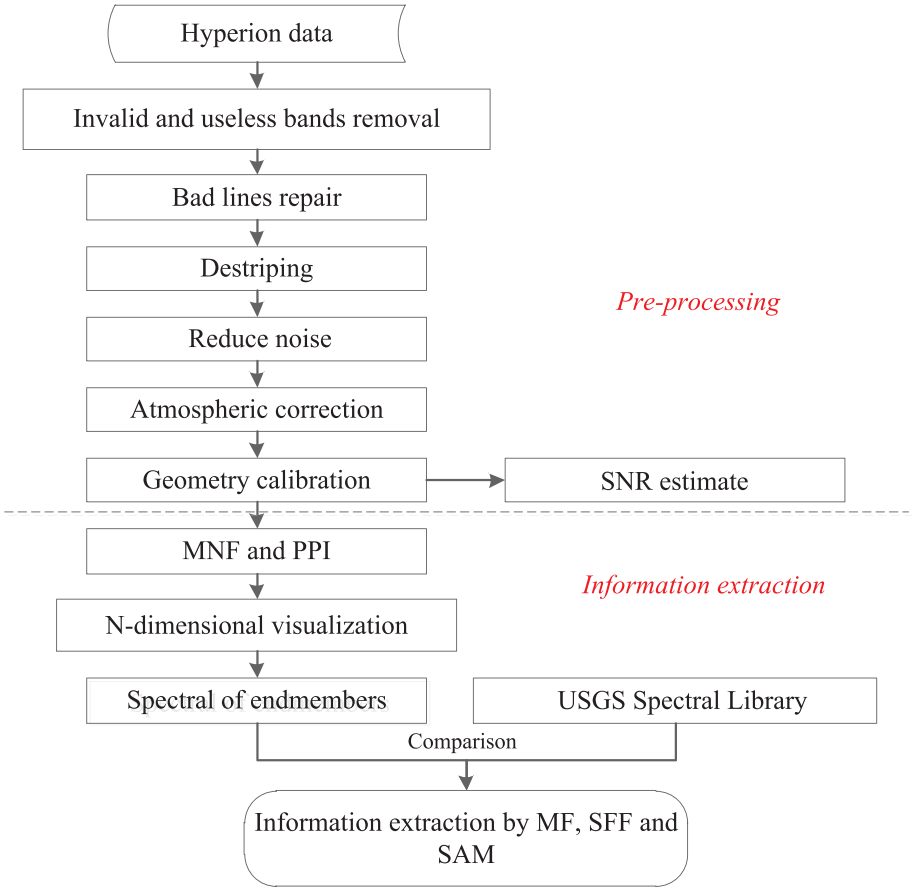

Fig. 3. Flowchart of Hyperion data processing steps in this study.

average filter method. In addition, the 1st derivative and continuum removal were applied to gain further spectral characteristics to extract the alteration information (Kumar et al., 2013; Malenovský et al., 2013).

3. Theory and method

3.1. Micro-seepage theory

Distinguished from conventional oil and gas reservoirs, the CBM exists with three ordinary states (adsorbed, free and water-soluble) in coal seam. Although CBM is generally confined beneath the cap rocks and absorbed on the inside of pores within the coal seam, the strong diffusion ability of CBM at free state and the big pore diameter of the cap rock, which leads to CBM leakage towards ground surface above the CBM reservoirs. Additionally, it is certain that there is much open fractures and underground water considered as the migration pathway in the CBM reservoirs, so CBM at free and water-soluble state can migrate slowly near the ground surface with faults and underground water regardless of the ability of CBM (Rice, 2003; Pashin et al., 2014; Zhang et al., 2000; Chen, 2012). Given that the underground hydrocarbon permeates up to elevate the hydrocarbon components in the soil, the interaction of hydrocarbon components with the material of the stratigraphic column generates an ample variety of physical, chemical, botanical, microbiological, and mineralogical alterations on the surface. For example, the interaction with the ground water forms a weak acid, makes the Fe^{3+} translate to Fe^{2+}, generates hydroxyl minerals, combines into the carbonate with the metal ions, keeps the clay mineral enrichment, shift the vegetation's red edge to blue, and causes other effects. Conceptual model of hydrocarbon seepage mechanism is shown in Fig. 4. The above phenomena indicate the reflectance spectrum of rock or vegetation depending on the mineralogical composition of its surface, as the absorption characteristics of these minerals in VIS, NIR and SWIR regions are produced by either electronic or vibrational processes (Hunt and Salisbury, 1970). A comprehensive analysis of the spectral absorption compositional features can provide significant insights into the causes of spectral variations for extracting remote sensing alterations (Cloutis and Gaffey, 1991; Cloutis et al., 2004).

3.1.1. Altered minerals

3.1.1.1. Bleaching. Bleaching promotes the red bed discoloration anomaly due to the action of reduced solutions that facilitate the removal of ferric ions and the generation of ferrous ions (Donovan, 1974; Schumacher, 1996; Van der Meer, et al., 2002; Everett et al., 2002; Khan and Jacobson, 2008). The chemical reactions are shown in the following expressions:

$$C_nH_m + Fe_2O_3 \rightarrow Fe_3O_4 + FeO + CO_2 + H_2O \quad (1)$$

$$C_nH_m + Fe(OH)_3 \rightarrow Fe_3O_4 + FeCO_3 + 2H_2O \quad (2)$$

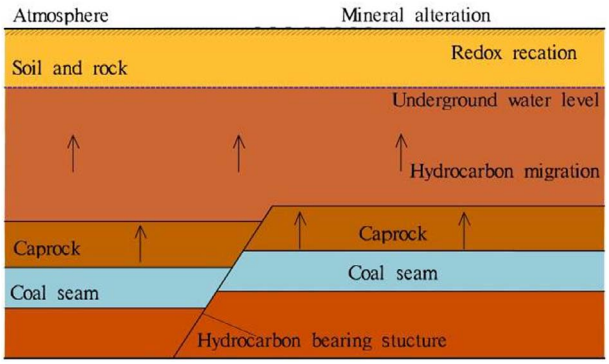

Fig. 4. Conceptual model of hydrocarbon seepage mechanism.

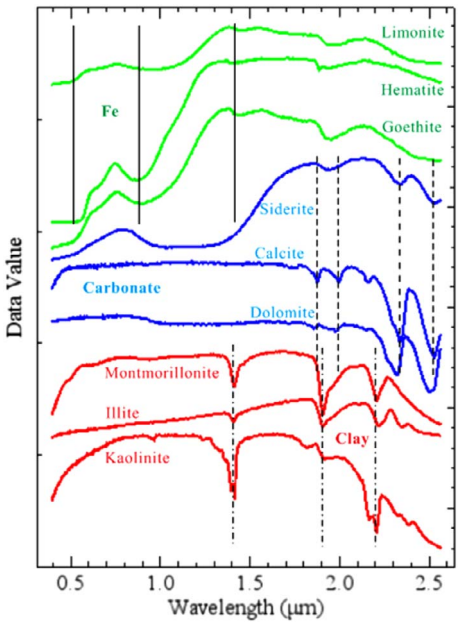

Fig. 5. Offset spectral plots of major and altered minerals from the USGS mineral spectral library (ENVI 5.3) involving iron minerals, carbonates and clay minerals.

This phenomenon can be detected based on the rock or soil spectral characteristics in VIS and NIR bands. In particular, the electromagnetic spectrum of ferric-bearing minerals (i.e., limonite, hematite (Fe_2O_3), or goethite) has a steep gradient in the VIS region. Once these minerals are eliminated, a sharp decrease is observed in the visible reflectance gradient (Lammoglia and Filho, 2013). Furthermore, given that the ferric ions change to ferrous ions (i.e. pyrite, siderite ($FeCO_3$), magnetite (Fe_3O_4), and eventually jarosite), a strong absorption of ferrous ions shows a broad shallow band at 1.0–1.4 μm apart from the absorption features of ferric ions at 0.45–0.5 μm and 0.8–0.9 μm (shown by the vertical line in Fig. 5). These characteristics can be used to separate bleaching from unbleached red beds by spectral data.

3.1.1.2. Carbonates. Carbonates are the obvious alteration minerals that combine with the metal ions by chemical oxidation or bacteriologic conversion under the micro-seepage of hydrocarbons micro-seepage and enrich enrichment in the surface (Clarke and Cleverly, 1991; Schumacher, 1996). The chemical reaction is shown in the following expression:

$$CH_4 + CaSO_4 + O_2 \rightarrow CaCO_3 + H_2S \quad (3)$$

The carbonate minerals such as calcite ($CaCO_3$), dolomite and magnesite possess useful narrow absorption features around at 2.35 μm due to their C-O bands (Hunt and Ashley, 1979; Mars and Rowan, 2010). Particularly, the siderite as near-surface diagenetic carbonates is formed through the solubility of ferric ions present in other minerals and their subsequent incorporation as a byproduct of methane oxidation (Hörig et al., 2001). The moderate absorption feature at 2.3 μm is caused by calcite content and subordinately, by others around 1.9, 2.0, and 2.5 μm depending on the spectral characteristics of the carbonates. These common calcite bands can be used to extract anomalies and map the carbonate concentrations. Hence, carbonates can be distinguished and identified by variations in their absorptions (shown by the vertical dashed line in Fig. 5) in the SWIR range.

3.1.1.3. Clay minerals. A reduced and slightly acidic environment produced by the gas that contains CO_2, H_2S, and methane close to the surface promotes the alteration of feldspar minerals into clay minerals, and may convert the normally stable illite clays into kaolinite ($All_4[SiO_{10}](OH)_8$), which is closely related with hydrocarbon anomalies

(Clarke and Cleverly, 1991; Yang et al., 1998). The spectral characteristic of kaolinite exhibits two diagnostic double absorption features in the SWIR region centered at 1.4 μm and 1.9 μm as well as a series of features between 2.0 μm and 2.4 μm (shown by the vertical dash-dot lines in Fig. 5), which result from the hydroxyl bands (Mars and Rowan, 2010). Moreover, Montmorillonite ($(Na, Ca)_{0,3}(Al, Mg)_2Si_4O_{10}(OH)_2{\cdot}n(H2O)$) has a 2.2 μm AlOH absorption feature. The doublet and subordinate absorption features can be indicative in clay mineral enrichment areas using spectral data. In addition, bleaching, as a function of secondary effects, can enhance the spectral characteristic of clay minerals in soil (Lammoglia and Filho, 2013). The absorption features of the clays tend to become more evident when the ferric ions are removed from the soil.

3.1.2. Geobotanical anomalies

Geobotanical anomalies generally exist in environment with heavy metals and hydrocarbons, such as areas with a lack of vegetation, the presence of an indicator plant, canopy architecture variations and plant cell structure change, which are the commonly marked features caused by the micro-seepage of hydrocarbons. Most of the studies that demonstrate, the above mentioned changes of vegetation are based on the spectral character variations on the different spectral bands: the variation of chlorophyll pigment manifested in VIS bands, the plant call structure with responses from NIR bands and the leaf water in SWIR bands (Hörig et al., 2001; Sanches et al., 2013). Moreover, the diagnostic spectral features of altered vegetation are analyzed through mathematical and statistical analyses. The main spectral features of vegetation comprise four feature points (blue valley, green peak, red valley, and near infrared high reflection point) and the three feature edges (blue edge, yellow edge, and red edge). Given the reflectance of vegetation that rapidly increased from 700 nm to 800 nm, the curve-like linearity with a big slope is called, “red edge”, which is a significant parameter for researching the growth status of vegetation. The vegetation under hydrocarbon stress displays a characteristic displacement of the “red edge” inflection towards short wavelengths, and is called, “Blue Shift”, which is a famous phenomenon and has been used to remotely extract geobotanical anomalies associated with hydrocarbon micro-seepage as shown in Fig. 6 (Clarke and Cleverly, 1991; Hörig et al., 2001; Noomen et al., 2012). Moreover, it provides a theoretical basis for the study of vegetation contamination using hyperspectral remote sensing technology. In addition, the location, reflectivity and slope of the three feature edges essential to identifying the diagnostic anomaly characteristics in the CBM enrichment region.

In summary, the interesting targets of the hydrocarbon micro-seepage prospective map can be identified from the following two aspects in this paper: 1) in the bare soil region, areas with a high concentration of hydrocarbon gas and areas where the ferric iron are removable and areas of carbonate (especially calcite and siderite) and clay (particularly kaolinite) enrichment; and 2) in the vegetation region, the areas where

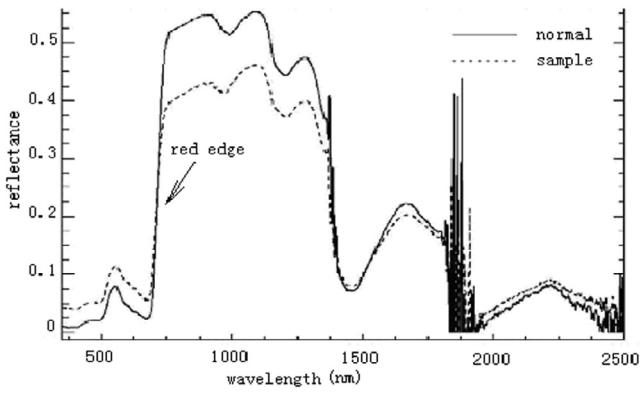

Fig. 6. Spectral of normal reference and altered sample vegetation in the field.

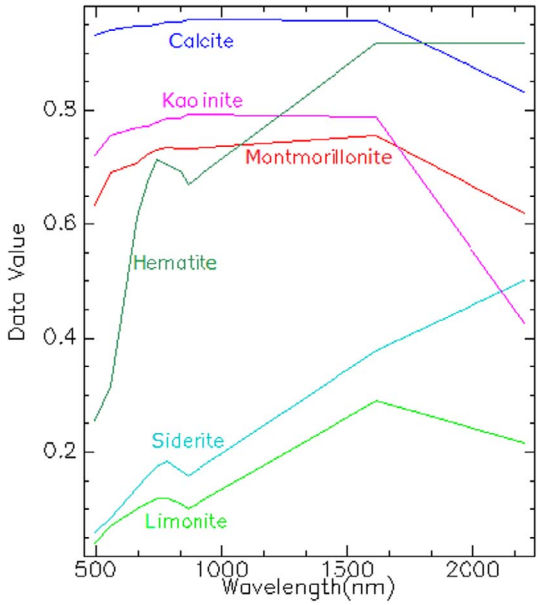

Fig. 7. Wavelength of classical altered minerals from the USGS mineral spectral library resampled to Sentinel-2 data.

geobotanical anomalies exist and experience have strong changes in the spectral features of vegetation. Notably, the above alteration characteristics can be affected by hydrocarbons at surfaces; however, in practice they do not have to occur singularly or simultaneously, and none of them are in themselves unique to hydrocarbon micro-seepage. Moreover, given the other reasons, such as heavy metal contamination and methane pipeline leakage, the above phenomena can emerge.

3.2. Information extraction methods

3.2.1. Spectral absorption feature extraction method

As the typical methods, band math and PCA methods are widely utilized to extract the mineral alteration information by using remote sensing imagery which based on the spectral absorption feature of altered minerals (Rowan and Mars, 2003; Pour and Hashim, 2012; Rajendran and Nasir, 2017; Liu et al., 2017). A band math method, such as the normalized difference vegetation index (NDVI) that can enhance the effect of vegetation, is applied. The wavelength of classical altered minerals (calcite, siderite, montmorillonite, kaolinite, limonite and hematite) from the USGS mineral spectral library, as resampled to Sentinel-2 data is shown in Fig. 7.

The reflection and absorption features of clay minerals, such as montmorillonite and kaolinite, are at 1610 nm and 2190 nm, corresponding to bands 11 and 12 of Sentinel-2 data, respectively. As iron minerals, limonite and hematite have one clear absorption feature at 865 nm corresponding to band 8a and two clear reflection features at 740 nm and 1610 nm corresponding to bands 6 and 11, respectively. Hence, band ratios 11/12, 6/2, and 11/8a of Sentinel-2 data can improve the enrichment areas of hydroxyl bearing, iron oxides, and ferrous iron oxides. The above RGB band combinations are the prime FCC that can be created for visual interpretation over the alteration field of the study area (Van der Meer et al., 2014). On the other hand, considering that Sentinel-2 data only contain a few SWIR bands, the diagnostic spectral features of the carbonates minerals at 2300 nm do not exist in Fig. 7.

As a mathematical procedure, PCA is used to minimize the redundant information within highly correlated bands and produce a set of values of linearly uncorrelated variables called principal components, which is widely utilized to extract the alteration minerals (Crosta and Moore, 1989). A part of the principal components contain subtle but important information used to enhance understated altered

features, from which alteration information is extracted in a grey scale. The component used for extraction is chosen by the eigenvector of the covariance. Given that Sentinel-2 band ratios are an analogue of ASTER band ratios, the PCA method was used on bands 3, 6, 8a, and 11 to extract the ferrous alterations and bands 3, 8, 11, and 12 to extract the hydroxyl alterations.

In the vegetation region, the locations (λ), reflectivity (R), and slopes (k) of three edges were calculated to describe the altered vegetation features. Consider red edge as an example:

$$K_r = (R_{780} - R_{670})/(780 - 670) \quad (4)$$

$$\lambda_r = 700 + 40 \times (R_r - R_{700})/(R_{740} - R_{700}) \quad (5)$$

where $R_r = (R_{670} + R_{780})/2$, R_{670}, R_{700}, R_{740} and R_{780} are the reflectance at 550 nm, 670 nm, 680 nm, 700 nm, 740 nm, and 780 nm, respectively.

3.2.2. Full spectral profile matching method

In recent years, the hyperspectral remote sensing methods of alteration anomaly information extraction have been based the full spectral profile matching. Researchers have successfully analyzed and mapped the distribution of the alteration anomalies using hyperspectral remote sensing (Percival et al., 2013; Chen et al., 2013). Hydrocarbon alterations, such as calcite, kaolinite, and montmorillonite, were accurately extracted through matched filtering (MF), mixture tuned matched filtering (MTMF), spectral feature fitting (SFF) and spectral angle mapper (SAM) from hyperspectral remote sensing image (Molan et al., 2014; Farooq and Govil, 2014). In the MF algorithm, the similarity of pixel spectra and reference spectra are obtained using the local separation techniques based on the reference spectra, such as the end-member spectra, field measurement spectra and USGS mineral spectral library. In this method, the response of the known end-member spectrum is maximized, whereas the response of the unknown background is suppressed (Harsanyi and Chang, 1994). In the SFF algorithm, a least-square estimation method is used to calculate the quality of fitting between the pixel spectrum and reference spectrum, which are both processed by a continuum removal algorithm (Chen et al., 2007). In the SAM method, the angle between the pixel spectrum and reference spectrum in the n-dimensional vectors space (n is the number of bands) is calculated to estimate their comparability (Kruse et al., 1993). In this paper, the clay, carbonate and iron minerals were extracted through MF, SFF, and SAM algorithms, respectively, in the bare soil region to delineate the altered mineral abnormal area. In the Hyperion data, the alteration information was extracted using end-member spectra as the reference spectra which have similar diagnostic absorption characteristics with field spectra and USGS spectra of alteration minerals.

3.3. Validation method

Virtual verification is the basis of the accuracy evaluation method, which combines visual interpretation of the remote sensing data with the geological data (Chen et al., 2014; Molan et al., 2014; Chen et al., 2015). The using of the field samples based on the sample locations is also a typical method of evaluation. To further verify the results, 60 field samples were selected to confirm the altered minerals extraction results by X-ray diffraction analysis (XRD).

4. Results and analysis

4.1. Bare soil region

4.1.1. Iron mineral

In the study area, the main types of altered minerals are irons, clays, and carbonates combined with the geology materials. However, only the iron and clay minerals were extracted through band math and PCA methods from Sentinel-2 image in this paper. Considering the absorption feature of iron mineral at band 8a and two clear reflection features at bands 6 and 11, the diagnostic spectral features of iron mineral were enhanced by band math (band 11 / 8a) and PCA (band 3, 6, 8a, and 11) methods. The second principal component (PC 2) was selected for the iron mineral extraction because the PC 2 eigenvectors of band6, 11 and band 3, 8a were opposite in signs. The eigenvectors of the principal components of band 3, 6, 8a, and 11 are shown in Table 3. The threshold was set based on the average value plus the triple variance. The extraction results of iron minerals after the mean filtering are shown in Fig. 8 and denoted in red.

Table 3
Eigenvectors of principal components (band 3, 6, 8a, and 11).

	Band 3	Band 6	Band 8a	Band 11
PC 1	0.260284	0.570124	0.325139	0.708163
PC 2	0.232001	−0.168392	0.888728	−0.357745
PC 3	−0.919887	−0.037926	0.321854	0.220863
PC 4	0.179545	−0.803221	0.029267	0.567224

Fig. 8 indicates that the distribution of the iron mineral in the two methods, which was observed mostly in the central image and in the southwest region, was similar. The total PCA results were apparent, especially in the southwest region. The geology data show that the central region was the Hudi coal mining area in Jincheng, Shanxi Province. The distribution of the iron mineral was consistent with the coal mining area in which the CBM had been mined. The southern area could be considered a potential CBM enrichment region for further research.

4.1.2. Clay mineral

Given the clear absorption feature of clay minerals at band 12 and a reflection feature at band 11, the diagnostic spectral features of clay minerals were enhanced by band math (band 11/12) and PCA (band 3, 8, 11, and 12) methods. The fourth principal component (PC 4) was selected for the altered clay mineral extraction because the PC 4 eigenvectors of band 12 and the other bands were opposite in signs. The eigenvectors of the principal components of band 3, 8, 11, and 12 are shown in Table 4. The threshold was set based on the average value plus the double variance. The extraction results of clay minerals after the mean filtering are denoted in blue in Fig. 9.

Fig. 9 shows that the distribution of the clay mineral in the two methods varied slightly. Although the distribution of the clay minerals was basically similar in the central image, the distribution by the PCA method was largely visible in the southern region. The geology data show that the central region was also in the Hudi coal mining area. The distribution of the clay mineral in the central region corresponded to the CBM enrichment region. On the other hand, the extraction results in the southern area require further research.

4.1.3. Vegetation region

The main field vegetation samples comprised corn, mulberry, and cocklebur canopy, which were common in the study area. Meanwhile, the diagnostic spectral characteristics of the field spectral were calculated. A part of the statistical results of the three feature edges, namely location, reflectivity, and slope, are shown in Table 5. Meanwhile, the field photos are shown in Fig. 10. To visually compare the diagnostic spectral characteristics of three feature edges, the linear fitting results are shown in Fig. 11(a) to (c). Fig. 11(d) shows that the distributions of altered vegetation are based on the red edge slope.

Table 5 and Fig. 11(a) to (c) show that the changes of yellow edge slope, red edge slope, and the location of red edge were most significant, showing a rating of 39% with the reference spectrum in the vegetation region. In Fig. 11(d), the distribution of altered vegetation was mainly in the central image and coincided with Hudi coal mining area and the east Taihang Mountain.

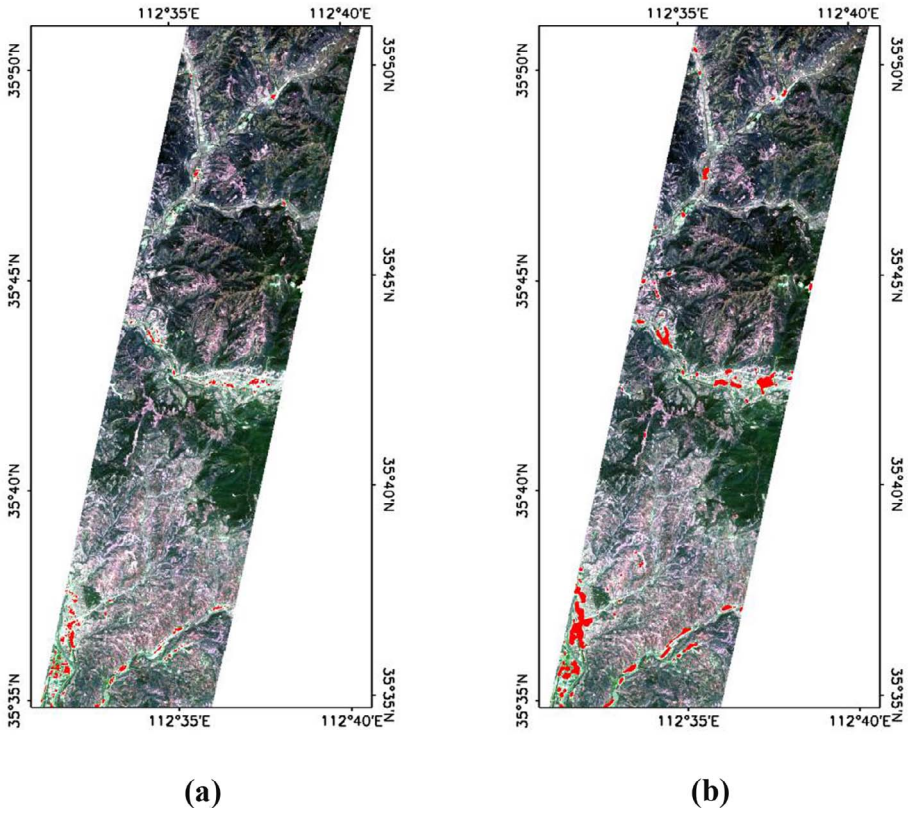

Fig. 8. Extraction results of the iron mineral are denoted in red. (a) Band math (band 11 / 8); (b) PCA (band 3, 6, 8a and 11).

Table 4
Eigenvectors of principal components (band 3, 8, 11, and 12).

	Band 3	Band 8	Band 11	Band 12
PC 1	0.296545	0.372710	0.802371	0.359651
PC 2	0.146439	0.712866	−0.561671	0.393577
PC 3	0.843122	−0.449958	−0.199606	0.216428
PC 4	−0.423984	−0.387875	−0.029727	0.817867

5. Validation

To verify the results, the alteration anomalies were extracted using the Hyperion data through full spectral profile matching method in Fig. 12(a). Sixty field samples collected from the homogeneous region of study area are located around the potential CBM enrichment region in Fig. 12(b). Producer's accuracy (PA), user's accuracy (UA), overall accuracy (OA), and kappa coefficient (Kappa) were used to evaluate the final alteration extraction results based on the XRD analysis (Yang and Chen, 2017). The accuracy assessment is shown in Table 6.

According to the full spectral profile of altered minerals and vegetation, the results of clay, carbonate, and iron mineral alteration anomaly information from the Hyperion image by MF, SFF, and SAM algorithms were largely distributed in the central and southern regions. Furthermore, to sum up the altered mineral and vegetation information, the prospecting signs were identified, and the regional anomaly areas were delineated. Synthesizing regional geology, the well logging and seismic data in the study area, the extracted results were consistent with the Jincheng Hudi mine area of Qinshui basin in the black rectangle of the central image. Specifically, the distribution of the irons and clays were consistent with the extraction results of Sentinel-2 data. Besides, the XRD analysis was applied to validate the effectiveness and extraction accuracy of Sentinel-2 data, of which the total accuracy value reaches to 77.50%, were computed the average of the better accuracies of clay and iron minerals (78.33% and 76.67%) by different extraction methods. This finding confirmed the authenticity and reliability of the alteration anomaly information extraction using remote sensing technology. Furthermore, the southern region is a potential target. However, the results of altered vegetation by Hyperion data were unsatisfactory. The spatial distribution of the altered vegetation appeared sporadically because the spectral features of altered vegetation were minute and influenced by many factors, one of which was the noise of the Hyperion data and background.

6. Discussion

This study focused on alteration extraction in the CBM enrichment region using the Sentinel-2 data by different methods. The spectral features of the iron, clay minerals and altered vegetation on the surface were analyzed. The compared results of Hyperion data, geological data and XRD analysis demonstrated the potential effectiveness of Sentinel-2 data for CBM exploration.

The spectral features of Sentinel-2 data (VIS, VNIR and SWIR) were analyzed targeting the identification of iron and clay mineral to detect hydrocarbon micro-seepage. The band math and PCA methods were used to extract the classical minerals, respectively. For the iron mineral, the results of two methods showed consistency with the extraction results of Hyperion data and XRD analysis results in the central image. However, the band math method is more appropriate for the iron mineral extraction than the PCA method because false information barely existed in the southern image. Meanwhile, the two methods obtained different results for clay mineral. Aside from the central area, the southern regions spatially coincided with the extraction results of Hyperion data and the XRD analysis where the abundant clay minerals were well-extracted by using the PCA method. Therefore, the PCA method is more suitable for clay mineral extraction than the band math method. Nevertheless, the carbonates minerals, such as calcite and siderite, were hardly extracted because SWIR bands were insufficient. The diagnostic spectral features of carbonate minerals were not yet available in Sentinel-2 data. In turn, the integration of the multi-source data, such as ASTER, will become necessary in the future.

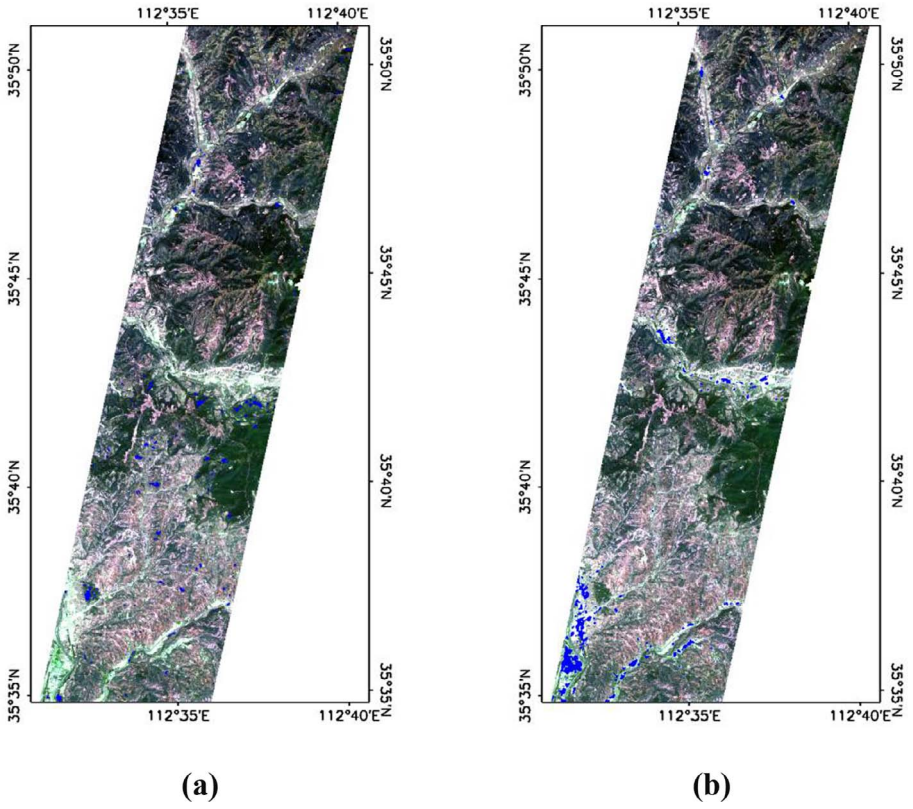

Fig. 9. Extraction results of the clay mineral are denoted in blue. (a) Band math (band 11 / 12); (b) PCA (band 3, 8, 11 and 12).

Until now, the altered minerals have been thoroughly examined, whereas the geobotanical anomalies have been frequently overlooked, leading to the following two aspects may result. On one hand, a majority of studies chose in the bare soil region as a study area to reduce the influence of vegetation and to extract the altered minerals. On the other hand, the geobotanical anomalies are so weak information that is difficult to distinguish, and the band range of the red edge is rarely involved in the satellite data. Therefore Sentinel-2 data can be used to extract the altered vegetation. Through analyzing the diagnostic spectral characteristics of the vegetation in the CBM enrichment region, the changes of yellow edge slope and red edge location and slope were outstanding, providing a rating of 39% with the reference spectra. The distribution of altered vegetation based on the red edge slope was mainly in the central image and coincided with Hudi coal mining area, which was mining the CBM.

The full spectral profile matching methods (i.e., MT, SFF, and SAM) were applied for Hyperion data to extract the alteration on the basis of VNIR–SWIR bands. For each technique used, the difference in the quality of the results did not exceed 10%. The optimum results were obtained by using the full spectral profile matching methods, that is, those more restrictive than the selected reference spectra. The diagnostic spectral characteristics of alteration anomaly information in the CBM enrichment can easily be described by hyperspectral remote sensing. Hence, the total accuracy of the extraction result by the Hyperion data reached 78.30%, which was slightly greater than the Sentinel-2 data obtained through XRD analysis. However, the bad line, stripe, noise and swath of Hyperion data limit the application.

The advantage of Sentinel-2 data with respect to Hyperion data is the 290 km wide swath, which provides a large-scale and rapid method to observe the earth's surface. Furthermore, the processing steps, including the band math and PCA methods, are easy and effective. Moreover, the processing works are inexpensive and can be done indoors, unlike seismic exploration and drilling. Consequently, the alteration extraction using Sentinel-2 data possesses the following advantages: high efficiency, agility, low cost, and the ability cover a large area. Although the techniques presented the alteration extraction results of the micro-seepages in association with spectral analysis methods for CBM enrichment prospecting, micro-seepage can be controlled by structure and drainage and the distribution of alteration extraction results are not necessarily correlated with the regions with high gas content. Furthermore, we cannot be sure that the mineral alterations over CBM reservoirs in this study area were only caused by CBM seepage to the ground surface because of more than one explanation for the results in remote sensing geology. It requires more experiments to

Table 5
Statistic results of the diagnostic spectral characteristics of altered vegetation.

Vegetation spectral characteristics		Blue edge			Yellow edge			Red edge		
		λ/nm	R	Slope	λ/nm	R	Slope	λ/nm	R	Slope
Corn canopy	Reference	523	0.088	0.541	569	0.115	−0.602	718	0.278	6.881
	Sample 1	523	0.069	0.479	569	0.092	−0.471	715	0.205	5.531
	Sample 2	522	0.058	0.404	569	0.076	−0.442	714	0.191	5.541
	Sample 3	522	0.053	0.393	568	0.072	−0.427	700	0.140	5.600
Cocklebur canopy	Reference	523	0.110	0.752	569	0.129	−0.627	718	0.379	10.116
	Sample	523	0.113	0.595	568	0.129	−0.381	716	0.336	7.759

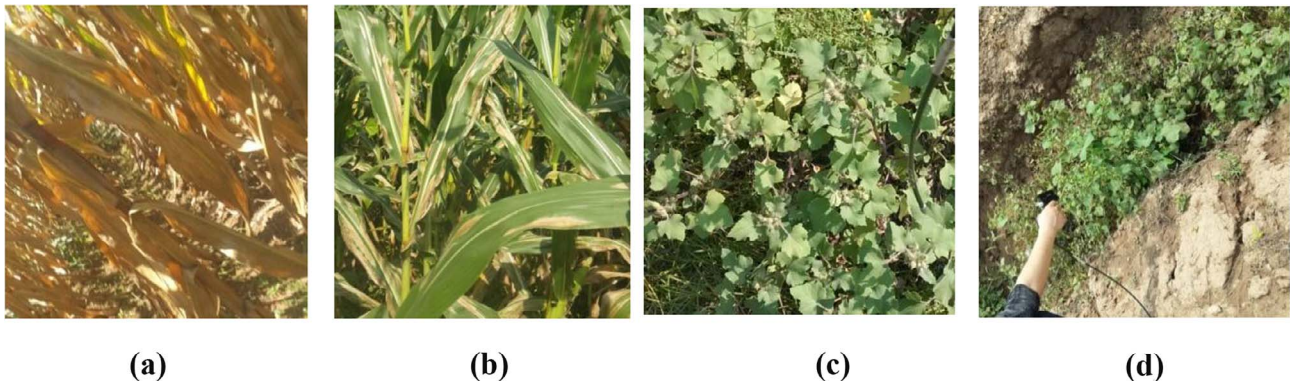

Fig. 10. Field photos in the study area. (a) Sample 3 of the corn canopy closed to CBM well No.3; (b) Sample 2 of the corn canopy near CBM well No.2; (c) Sample of the cocklebur canopy closed to CBM well No.1; (d) Reference sample of the cocklebur canopy collected in the Jiafeng town far away CBM well.

investigate that there are similar surface mineral characteristics in more CBM enrichment areas. The subsequent prospection, such as core analysis and well-test analysis, are essential for further confirmation of commercial CBM exploitation (Zhang et al., 2015; Zhen et al., 2016).

7. Conclusions

In this paper, the alteration information was extracted from the CBM enrichment region using Sentinel-2 data. The following conclusions were obtained:

1) The alteration information, including the irons, clays, and altered vegetation was successfully extracted using Sentinel-2 data. The distribution of iron and clay minerals exhibited good accuracy (78.33% and 76.67%) when using XRD analysis. The distribution of altered vegetation was basically consistent with Hudi coal mining area in Jincheng, Shanxi province. These results demonstrate that Sentinel-2 data have an alteration mapping ability and can be used to identify the alteration anomaly region.
2) In the bare soil region, the iron and clay minerals were extracted by band math and PCA methods. The band 11 ratio band 8a was the most suitable method to extract the iron minerals, whereas the PCA method was more appropriate than band 11 ratio band 12 for the clay mineral extraction. In addition, the results of Sentinel-2 data were relatively consistent with Hyperion data, particularly in the central image. However, the carbonate minerals were difficult to extract because of insufficient SWIR bands.
3) The diagnostic spectral features of the altered vegetation in the CBM enrichment were calculated in the vegetation region. The yellow edge slope, red edge slope and location were the most outstanding

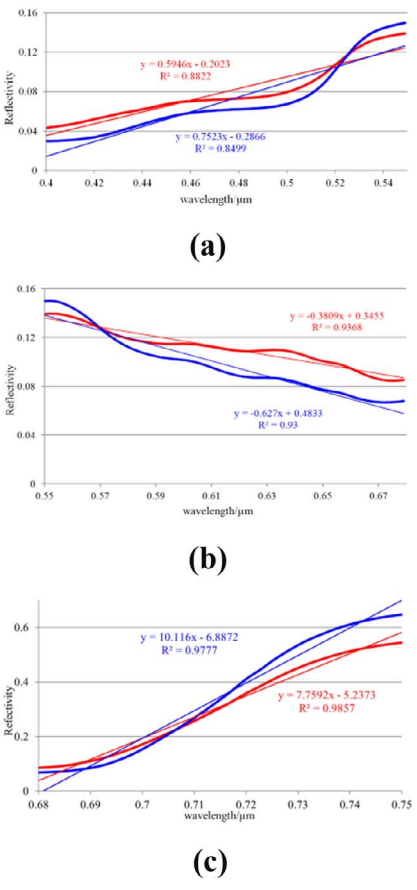

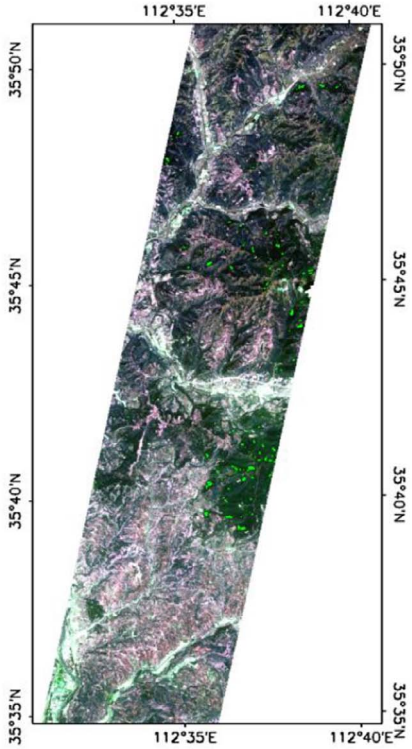

Fig. 11. (a) Red edge linear fitting; (b) Yellow edge linear fitting; (c). Blue edge linear fitting; (d) Extraction results of altered vegetation based on red edge slope are denoted in green.

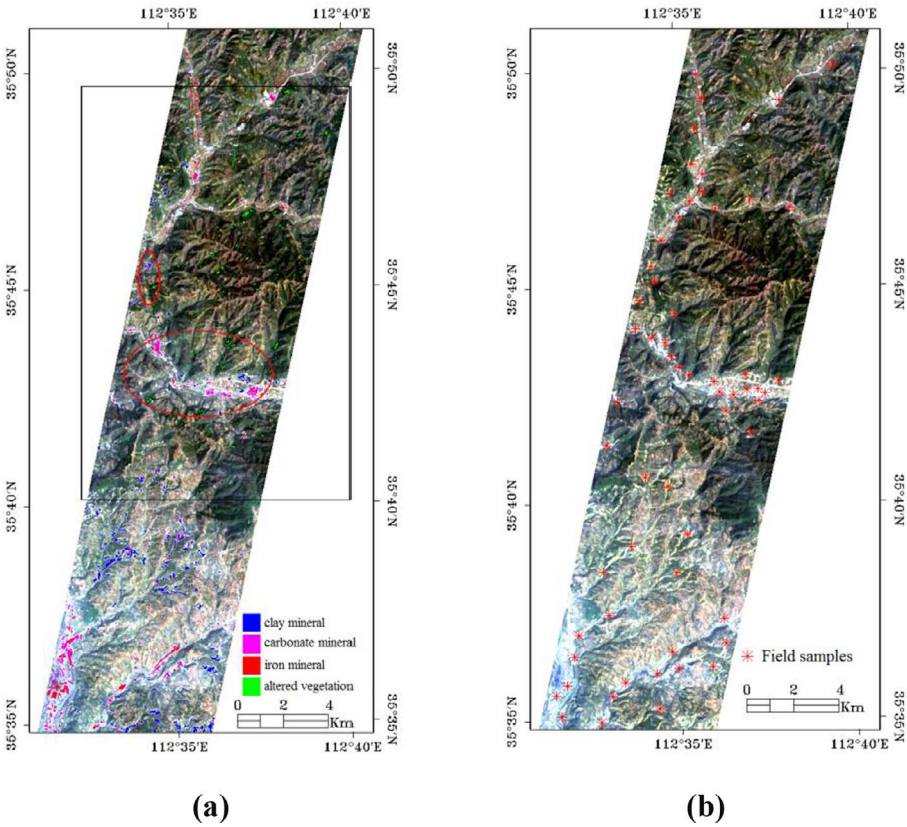

Fig. 12. (a) Distribution of alteration anomalies using the Hyperion data, such as clays, carbonates, irons and altered vegetation by MT, SFF and SAM respectively; (b) Location of the 60 samples selected for XRD analysis to assess the accuracy of the results.

Table 6
Accuracy assessment of the altered mineral extraction results through XRD analysis.

Methods	Class	Producer's accuracy/%	User's accuracy/%	Overall accuracy/%	Kappa
Band math	Clay minerals	79.31	76.67	78.33	0.567
	Iron minerals	72.41	70.00	71.67	0.433
PCA	Clay minerals	75.86	73.33	75.00	0.500
	Iron minerals	70.97	78.57	76.67	0.518

characteristics. In particular, the highest rate of the feature edge slope reached up to 39% with reference spectrum, which provided an interesting direction for future research. Thus, analyzing the feature edge slope of vegetation is necessary to identify and distinguish the altered vegetation.

4) The potential geological application of Sentinel-2 data was illustrated to identify the direction of CBM exploration through a large-scale, highly efficient, agile and inexpensive way. This is also the most significant conclusion reached by this study.

On the other hand, further research on the potential geological application of Sentinel-2 data is necessary to pursue and will be significant in the future. The diagnostic spectral features of altered vegetation can be used to clarify and support the weak information. Moreover, the results of altered vegetation technically lack laboratory validation. The field samples only covered a part of the study area; thus, more field samples will be collected in the entire study area to verify the accuracy in the future works. Besides, the geochemical analysis (e.g., isotopic tracer) is required in the future work to finally demonstrate the alteration minerals caused by CBM seepages in the study area. Furthermore, the universality and generalizability of the methods need further verification. In general, the multi-source data integration will inevitably become trend for geology exploration in the future.

Author contributions

Li Chen conceived and designed the experiments; Li Chen performed the experiments; Li Chen and Xiucheng Yang analyzed the data; Li Chen and Guangwei Zhen contributed reagents/materials/analysis tools; Li Chen and Xiucheng Yang wrote the paper.

Conflicts of interest

The authors declare no conflict of interest.

Acknowledgments

This work was supported by the Youth Innovation Fund Project of Ministry of Land and Resources Key Laboratory of Airborne Geophysics and Remote Sensing Geology (2016YFL16) and Geological Survey Project of China (DD20160117). The authors gratefully acknowledge the European Space Agency (ESA) and United States Geological Survey (USGS) for providing free Sentinel-2 and Hyperion datasets to carry out this study. We also thank the anonymous reviewers and editor whose suggestions helped to improve the paper.

References

Almeida-Filho, R., Miranda, F.P., Yamakawa, T., Bueno, G.V., Moreira, F.R., Camargo, E.G., Bentz, C.M., 2002. Data integration for a geologic model of hydrocarbon microseepage areas in the Tonã Plateau region, North Tucano basin. Brazil. Can. J. Remote Sens. 28 (1), 96–107.

Ayers, W.B.J., 2002. Coal bed gas systems, resources, and production and a review of contras ting cases from the San Juan and Powder River basins. AAP G Bull. 86 (11), 1853–1890.

Chen, C., Qin, Q., Chen, L., Zheng, H., Fa, W., Ghulam, A., Zhang, C., 2015. Photometric

correction and reflectance calculation for lunar images from the Chang'E-1 CCD stereo camera. J. Opt. Soc. Am. A: Opt. Image Sci. Vision 32 (12), 2409–2422.
Chen, C., Qin, Q., Zhang, N., Li, J., Chen, L., Wang, J., Qin, X., Yang, X., 2014. Extraction of bridges over water from high-resolution optical remote-sensing images based on mathematical morphology. Int. J. Remote Sens. 35 (10), 3664–3682.
Chen, L., Qin, Q.M., Chen, C., Jiang, H.B., 2012. Remote sensing information of mineralizing alteration extraction methods. IEEE Int. Geosci. Remote Sens. Symp. 2012, 5947–5950.
Chen, J.C., 2012. Study of Non-seismic Integrated Geophysical Technology and Experiment for Coal Bed Methane Enrichment Region. Chengdu University of Technology (Doctoral Dissertation).
Chen, S., Chen, L., Liu, Y., Li, X., 2013. Experimental simulation on mixed spectra of leaves and calcite for inversion of carbonate minerals from EO-1 Hyperion data. GISci. Remote Sens. 50 (6), 690–703.
Chen, X., Warner, T.A., Campagna, D.J., 2007. Integrating visible, near-infrared and short-wave infrared hyperspectral and multispectral thermal imagery for geological mapping at Cuprite, Nevada. Remote Sens. Environ. 110 (3), 344–356.
Clarke, R.H., Cleverly, R.W., 1991. Petroleum seepage and post accumulation migration. In: England W.A., Fleet A.J., (Eds.) Petroleum migration. Geological Society London Special Publications, 59(1), 265–271.
Clevers, J.G.P.W., Gitelson, A.A., 2013. Remote estimation of crop and grass chlorophyll and nitrogen content using red-edge bands on Sentinel-2 and-3. Int. J. Appl. Earth Obs. Geoinform. 23 (8), 344–351.
Cloutis, E.A., Gaffey, M.J., 1991. Pyroxene spectroscopy revisited: spectral–compositional correlations and relationship to geothermometry. J. Geophys. Res. 96 (E5), 22809–22826.
Cloutis, E.A., Sunshine, J.M., Morris, R.V., 2004. Spectral reflectance-compositional properties of spinels and chromites: implications for planetary remote sensing and geothermometry. Meteorit. Planet. Sci. 39 (39), 545–565.
Crosta, A.P., Moore, J.M., 1989. Enhancement of Landsat Thematic Mapper imagery for residual soil mapping in SW Minais Gerais State, Brazil: A prospecting case history in Greenstone belt terrain. In: Proceedings of the 7th ERIM Thematic Conference: Remote sensing for exploration geology. pp. 1173–1187.
Donlon, C., Berruti, B., Buongiorno, A., Ferraria, M.H., Femenias, P., Frerick, J., Goryll, P., 2012. The global monitoring for environment and security (GMES) sentinel-3 mission. Remote Sens. Environ. 120 (6), 37–57.
Donovan, T.J., 1974. Petroleum microseepage at cement, Oklaroma—evidence and mechanism. AAPG Bull. 58 (3), 429–446.
Drusch, M., Bello, U.D., Carlier, S., Colin, O., Fernandez, V., Gascon, F., Hoersch, B., Isola, C., Laberinti, P., Martimort, P., 2012. Sentinel-2: ESA's optical high-resolution mission for GMES operational services. Remote Sens. Environ. 120 (1), 25–36.
Du, Y., Zhang, Y., Ling, F., Wang, Q., Li, W., Li, X., 2016. Water bodies' mapping from sentinel-2 imagery with modified normalized difference water index at 10-m spatial resolution produced by sharpening the SWIR band. Remote Sens. 354 (8), 1–19.
Ducart, D.F., Crosta, A.P., Filho, C.R.S., Coniclio, J., 2006. Alteration mineralogy at the Cerro La Minaepithermal prospect, Patagonia, Argentina: field mapping, shortwave infrared spectroscopy, and ASTER images. Econ. Geol. 101 (5), 981–996.
Eitel, J.U., Vierling, L.A., Litvak, M.E., Long, D.S., Schulthess, U., Ager, A.A., Krofcheck, D.J., Stoscheck, L., 2011. Broadband, red-edge information from satellites improves early stress detection in a new Mexico conifer woodland. Remote Sens. Environ. 115 (12), 3640–3646.
Everett, J.R., Staskowski, R.J., Jengo, C., 2002. Remote sensing and GIS enable future exploration success. World Oil 223 (11), 59–63.
Farooq, S., Govil, H., 2014. Mapping Regolith and Gossan for mineral exploration in the Eastern Kumaon Himalaya, India using Hyperion data and object oriented image classification. Adv. Space Res. 53 (12), 1676–1685.
Fu, B.H., Zheng, G.D., Ninomiya, Y., Wang, C.Y., Sun, G.Q., 2007. Mapping hydrocarbon-induced mineralogical alteration in the northern Tian Shan using ASTER multispectral data. Terra Nova 19 (4), 225–231.
Fu, X., Qin, Y., Wang, G.G.X., Rudolph, V., 2009. Evaluation of gas content of coalbed methane eservoirs with the aid of geophysical logging technology. Fuel 88 (1), 2269–2277.
Gersman, R., Ben Dor, E., Beyth, M., Avigad, D., Abraha, M., Kibreab, A., 2008. Mapping of hydrothermally altered rocks by the EO-1 Hyperion sensor, Northern Danakil Depression, Eritrea. Int. J. Remote Sens. 29 (13), 3911–3936.
Green, R.O., Pavri, B.E., Chrien, T.G., 2003. On-orbit radiometric and spectral calibration characteristics of EO-1 Hyperion derived with an underflight of AVIRIS and in situ measurements at Salar de Arizaro, Argentina. IEEE Trans. Geosci. Remote Sens. 41 (6), 1194–1203.
Gu, B., Sheng, V.S., 2016. A robust regularization path algorithm for ν-support vector classification. IEEE Trans. Neural Networks Learn. Syst. 28 (5), 1241–1248.
Gu, B., Sheng, V.S., Wang, Z., Ho, D., Osman, S., Li, S., 2015. Incremental learning for ν-Support Vector Regression. Neural Networks. 67(C), 140–150.
Harsanyi, J.C., Chang, C., 1994. Hyperspectral image classification and dimensionality reduction: an orthogonal subspace projection approach. IEEE Trans. Geosci. Remote Sens. 32 (4), 779–785.
Hörig, B., Kühn, F., Oschütz, F., Lehmann, F., 2001. HyMap hyperspectral remote sensing to detect hydro-carbons. Int. J. Remote Sens. 22 (8), 1413–1422.
Hubbard, B.E., Crowley, J.K., Zimbelman, D.R., 2003. Comparative alteration mineral mapping using visible to shortwave infrared (0.4–2.4 μm) Hyperion, ALI, and ASTER Imagery. IEEE Trans. Geosci. Remote Sens. 41 (6), 1401–1410.
Hunt, G.R., Salisbury, J.W., 1970. Visible and near infrared spectra of minerals and rocks: I. Silicate minerals. Mod. Geol. 1, 283–300.
Hunt, G.R., Ashley, R.P., 1979. Spectra of altered rocks in the visible and near infrared. Econ. Geol. 74 (7), 1613–1629.
Khan, S.D., Jacobson, S., 2008. Remote sensing and geochemistry for detecting hydrocarbon microseepages. Geol. Soc. Am. Bull. 120 (1–2), 96–105.
Kruse, F.A., Lefkoff, A.B., Dietz, J.B., 1993. Expert system-based mineral mapping in northern death-valley, California/Nevada, using the airborne visible infrared imaging spectrometer (AVIRIS). Remote Sens. Environ. 44 (2–3), 309–336.
Kruse, F.A., Boardman, J.W., Huntington, J.F., 2003. Comparison of airborne hyperspectral data and EO-1 Hyperion for mineral mapping. IEEE Trans. Geosci. Remote Sens. 41 (6), 1388–1400.
Kühn, F., Oppermann, K., Horig, B., 2004. Hydrocarbon index—an algorithm for hyperspectral detection of hydrocarbons. Int. J. Remote Sens. 25 (12), 2467–2473.
Kumar, A., Manjunath, K.R., Meenakshi, Bala, R., Sud, R.K., Singh, R.D., Panigrahy, S., 2013. Field hyperspectral data analysis for discriminating spectral behavior of tea plantations under various management practices. Int. J. Appl. Earth Obs. Geoinf. 23(8), 352–359.
Lammoglia, T., Filho, C.S., 2012. Mapping and characterization of the API gravity of offshore hydrocarbon seepages using multispectral ASTER data. Remote Sens. Environ. 123 (3), 381–389.
Lammoglia, T., Filho, C.R.D.S., 2013. Unraveling hydrocarbon microseepages in onshore basins using spectral–spatial processing of advanced spaceborne thermal emission and reflection radiometer (ASTER) data. Surv. Geophys. 34 (34), 349–373.
Landgrebe, D.A., Serpico, S.B., Crawford, M.M., Singhroy, V., 2001. Introduction to the special issue on analysis of hyperspectral image data. IEEE Trans. Geosci. Remote Sens. 39 (7), 1343–1345.
Liu, L., Zhou, J., Han, L., Xu, X.L., 2017. Mineral mapping and ore prospecting using Landsat TM and Hyperion data, Wushitala, Xinjiang, northwestern China. Ore Geol. Rev. 81, 280–295.
Lyder, D., Feng, J., Rivard, B., Gallie, A., Cloutis, E., 2010. Remote bitumen content estimation of Athabasca oil sand from hyperspectral infrared reflectance spectra using Gaussian singlets and derivative of Gaussian wavelets. Fuel 89 (3), 760–767.
Malenovský, Z., Rott, H., Cihlar, J., Schaepman, M.E., García-Santos, G., Fernandes, R., Berger, M., 2012. Sentinels for science: Potential of Sentinel-1, -2 and -3 missions for scientific observations of ocean, cryosphere, and land. Remote Sens. Environ. 120 (10), 91–101.
Malenovský, Z., Homolová, L., Zurita-Milla, R., Lukeˇs, P., Kaplan, V., Hanuˇs, J., Gastellu-Etchegorry, J.P., Schaepman, M.E., 2013. Retrieval of spruce leaf chlorophyll content from airborne image data using continuum removal and radiative transfer. Remote Sens. Environ. 131 (8), 85–102.
Mars, J.C., Rowan, L.C., 2010. Spectral assessment of new ASTER SWIR surface reflectanced at a products for spectroscopic mapping of rocks and minerals. Remote Sens. Environ. 114 (9), 2011–2025.
Molan, Y.E., Refahi, D., Tarashti, A.H., 2014. Mineral mapping in the Maherabad area, eastern Iran, using the HyMap remote sensing data. Int. J. Appl. Earth Obs. Geoinf. 27 (4), 117–127.
Moore, T.A., 2012. Coalbed methane: a review. Int. J. Coal Geol. 101 (6), 36–81.
Noomen, M.F., Van der Werff, H.M.A., Van der Meer, F.D., 2012. Spectral and spatial indicators of botanical changes caused by long-term hydrocarbon seepage. Ecol. Inf. 8 (2), 55–64.
Pashin, J.C., Mcintyre-Redden, M.R., Mann, S.D., Kopaska-Merkel, D.C., Varonka, M., Orem, W., 2014. Relationships between water and gas chemistry in mature coalbed methane reservoirs of the Black Warrior Basin. Int. J. Coal Geol. 126 (2), 92–105.
Percival, J.B., White, H.P., Goodwin, T.A., Parsons, M.B., Smith, P.K., 2013. Mineralogy and spectral reflectance of soils and tailings from historical gold mines, Nova Scotia. Geochem. Explor. Environ. Anal. 14 (14), 3–16.
Pesaresi, M., Corbane, C., Julea, A., Florczyk, A.J., Syrris, V., Soille, P., 2016. Assessment of the added-value of sentinel-2 for detecting built-up areas. Remote Sens. 8 (4), 299.
Pour, A.B., Hashim, M., 2012. The application of ASTER remote sensing data to porphyry copper and epithermal gold deposits. Ore Geol. Rev. 44, 1–9.
Qin, Q.M., Zhang, Z., Chen, L., Wang, N., Zhang, C., 2016. Oil and gas reservoir exploration based on hyperspectral remote sensing and super-low-frequency electromagnetic detection. J. Appl. Remote Sens. 10 (1), 016017.
Ren, H., Du, C., Liu, R., Qin, Q.M., Yan, G., Li, Z.L., Meng, J., 2014. Noise Evaluation of early images for Landsat 8 Operational Land Imager. Opt. Express 22 (22), 27270–27280.
Rajendran, S., Nasir, S., 2017. Characterization of ASTER spectral bands for mapping of alteration zones of Volcanogenic Massive Sulphide (VMS) deposits. Ore Geol. Rev. 88, 317–335.
Rice, C.A., 2003. Production waters associated with the Ferron coalbed methane fields, central Utah: chemical and isotopic composition and volumes. Int. J. Coal Geol. 56 (1–2), 141–169.
Rowan, L.C., Mars, J.C., 2003. Lithologic mapping in the Moutain Pass, California area using Advanced Spaceborne Thermal Emission and Reflection Radiometer (ASTER) data. Remote Sens. Environ. 84 (3), 350–366.
Sanches, I.D., Souza Filho, C.R.S., Magalhaes, L.A., Quiterio, G.C.M., Alves, M.N., Oliveira, W.J., 2013. Unravelling remote sensing signatures of plants contaminated with gasoline and diesel: an approach using the red edge spectral feature. Environ. Pollut. 174 (5), 16–27.
Schumacher, D., 1996. Hydrocarbon-induced alteration of soils and sediments. In: Schumacher, D., Abrams, M.A., (Eds.) Hydrocarbon migration and its near surface expression. AAPG memoir. 66, 71–89.
Schuster, C., Förster, M., Kleinschmit, B., 2012. Testing the red edge channel for improving land-use classifications based on high-resolution multi-spectral satellite data. Int. J. Remote Sens. 33 (17), 5583–5599.
Sircar, A., 2000. A review of coalbed methane exploration and exploitation. Curr. Sci. 79 (4), 404–406.
Sibanda, M., Mutanga, O., Rouget, M., 2015. Examining the potential of Sentinel-2 MSI spectral resolution in quantifying above ground biomass across different fertilizer treatments. ISPRS J. Photogramm. Remote Sens. 110, 55–65.

Souza Filho, C.R.D., Drury, S.A., 1998. Evaluation of JERS-1 (FUYO-1) OPS and Landsat TM images for mapping of gneissic rocks in Arid Areas. Int. J. Remote Sens. 19 (18), 3569–3594.

Tangestani, M.H., Moore, F., 2001. Comparison of three principal component analysis techniques to porphyry copper alteration mapping: a case study, Meiduk area, Kerman. Iran. Can. J. Remote Sens. 27 (2), 176–182.

Van der Meer, F.D., Van Dijk, P.V., Van der Werff, H.M.A., Yang, H., 2002. Remote sensing and petroleum seepage: a review and case study. Terra Nova 14 (1), 1–17.

Van der Meer, F.D., Van der Werff, H.M.A., Van Ruitenbeek, F.J.A., Hecker, C.A., Bakker, W.H., Noomen, M.F., Meijde, M.V.D., Carranza, E.J.M., de Smeth, J.B., Woldai, T., 2012. Multi- and hyperspectral geologic remote sensing: a review. Int. J. Appl. Earth Obs. Geoinf. 1, 112–128.

Van der Meer, F.D., Van der Werff, H.M.A., Van Ruitenbeek, F.J.A., 2014. Potential of ESA's Sentinel-2 for geological applications. Remote Sens. Environ. 148 (148), 124–133.

Van der Werff, H.M.A., Bakker, W.H., Van der Meer, F.D., Siderus, W., 2006. Combining spectral signals and spatial patterns using multiple Hough transforms: an application for detection of natural gas seepages. Comput. Geosci. 32 (9), 1334–1343.

Vane, G., Goetz, A.F.H., 1993. Terrestrial imaging spectrometry: current status, future trends. Remote Sens. Environ. 44 (2–3), 117–126.

Verrelst, J., Muñoz, J., Alonso, L., Delegido, J., Rivera, J.P., Camps-Valls, G., Moreno, J., 2012. Machine learning regression algorithms for biophysical parameter retrieval: opportunities for Sentinel-2 and-3. Remote Sens. Environ. 118 (4), 127–139.

Wang, N., Qin, Q.M., Chen, L., Bai, Y.B., Zhao, S.S., 2014. Dynamic monitoring of coalbed methane reservoirs using Super-Low Frequency electromagnetic prospecting. Int. J. Coal Geol. 127 (7), 24–41.

Xia, Z., Wang, X., Sun, X., Liu, Q., Xiong, N., 2016. Steganalysis of LSB matching using differences between nonadjacent pixels. Multimedia Tools App. 75 (4), 1947–1962.

Yang, H., Zhang, J., Van der Meer, F.D., Kroonerberg, B., 1998. Geochemistry and field spectroscopy for detecting hydrocarbon Microseepage. Terra Nova 10 (5), 231–235.

Yang, X.C., Chen, L., 2017. Evaluation of automated urban surface water extraction from Sentinel-2A imagery using different water indices. J. Appl. Remote Sens. 11 (2), 026016. http://dx.doi.org/10.1117/1.JRS.11.026016.

Yao, Y., Liu, D., Tang, D., Tang, S., Che, Y., Huang, W., 2009. Preliminary evaluation of the coalbed methane production potential and its geological controls in the Weibei Coal-field, Southeastern Ordos Basin, China. Int. J. Coal Geol. 78, 1–15.

Zhang, C.Y., Qin, Q.M., Chen, L., Nan, W., Zhao, S.S., Hui, J., 2015. Rapid determination of coalbed methane exploration target region utilizing hyperspectral remote sensing. Int. J. Coal Geol. 150–151, 19–34.

Zhang, J.B., Wang, H.Y., Zhao, Q.B., 2000. Coalbed Methane Geology of China. China Geological Publishing House, Beijing.

Zhen, G.W., Chen, L., Chen, C., Guo, B., 2016. Alteration anomaly information extraction using hyperspectral remote sensing in coalbed methane enrichment. In: 2016 IEEE International Geoscience and Remote Sensing Symposium (IGARSS), Beijing, China, 5394–5397.

Zheng, Y., Jeon, B., Xu, D., Wu, Q.M.J., Zhang, H., 2015. Image segmentation by generalized hierarchical fuzzy C-means algorithm. J. Intell. Fuzzy Syst. 28 (2), 4024–4028.

Zhou, Z., Wang, Y., Wu, Q.M.J., Yang, C.N., Sun, X., 2017. Effective and efficient global context verification for image copy detection. IEEE Trans. Inf. Forensics Secur. 12 (1), 48–63.

PROCEEDINGS OF SPIE

SPIEDigitalLibrary.org/conference-proceedings-of-spie

Comparison of inversion accuracy of soil copper content from vegetation indices under different spectral resolution

Zhongqing Sun, Kun Shang, Lingjun Jia

Zhongqing Sun, Kun Shang, Lingjun Jia, "Comparison of inversion accuracy of soil copper content from vegetation indices under different spectral resolution," Proc. SPIE 10611, MIPPR 2017: Remote Sensing Image Processing, Geographic Information Systems, and Other Applications, 106110Q (8 March 2018); doi: 10.1117/12.2288745

SPIE.

Event: Tenth International Symposium on Multispectral Image Processing and Pattern Recognition (MIPPR2017), 2017, Xiangyang, China

Comparison of Inversion Accuracy of Soil Copper Content from Vegetation Indices under Different Spectral Resolution

Zhongqing Sun[a,b], Kun Shang[*a] , Lingjun Jia[a,b],
[a]China Aero Geophysical Survey and Remote Sensing Center for Land and Resources, No.31 Xueyuan Rd. Haidian District, Beijing, China 100083; [b]China University of Geosciences (Beijing), No.29 Xueyuan Rd. Haidian District, Beijing, China 100083

ABSTRACT

Remote sensing inversion of heavy metal in vegetation leaves is generally based on the physiological characteristics of vegetation spectrum under heavy metal stress, and empirical models with vegetation indices are established to inverse the heavy metal content of vegetation leaves. However, the research of inversion of heavy metal content in vegetation-covered soil is still rare. In this study, Pulang is chosen as study area. The regression model of a typical heavy metal element, copper (Cu), is established with vegetation indices. We mainly investigate the inversion accuracies of Cu element in vegetation-covered soil by different vegetation indices according to specific spectral resolutions of ASD (Analytical Spectral Device) and Hyperion data. The inversion results of soil copper content in the vegetation-covered area shows a good accuracy, and the vegetation indices under ASD spectral resolution correspond to better results.

Key words: vegetation index; soil copper content; spectral resolution; inversion accuracy

1. INTRODUCTION

With developments of high spectral technology and demands of the national economy for resources, hyperspectral has become one of the state of the art technologies of mineral resource exploration, achieving good application results. Thanks to the advantages of continuous spectral curves and nanoscale spectral resolution, with vegetation spectrum and its derivations, hyperspectral data can be used to determine whether mineral element information in the vegetation-covered area is abnormal, and to obtain regional distribution of geochemical information. It provides unique indicative information for mineral resource investigation, and thus has a wide application prospect in geological prospecting over vegetation-covered area. Generally, the common remote sensing inversion methods of heavy metal in vegetation leaves are on the basis of physiological characteristics of the estimated vegetation spectrum under heavy metal stress, and empirical models with vegetation indices are established to inverse the heavy metal content of vegetation leaves. However, the inversion research of heavy metal content in vegetation-covered soil is still rare. In this study, the regression model of a typical heavy metal element,

* shangkun0213@126.com; phone: 86-10-62060320

MIPPR 2017: Remote Sensing Image Processing, Geographic Information Systems, and Other Applications, edited by Nong Sang, Jie Ma, Zhong Chen, Proc. of SPIE Vol. 10611, 106110Q · © 2018 SPIE
CCC code: 0277-786X/18/$18 · doi: 10.1117/12.2288745

copper (Cu), is established based on vegetation indices. Then the soil copper content in vegetation-covered area obtained by using ASD (Analytical Spectral Device) and Hyperion hyperspectral data, respectively, are compared so as to provide a more appropriate selection of spectral resolution for the inversion of Cu element.

2. METHODOLOGY

2.1 Study areas and data

2.1.1 Study areas

In this study, Pulang, Yunan Province is chosen as the study area. The Pulang porphyry copper deposit is located in the "Sanjiang" tectonic magmatic ore belt in the southwest of China, which is a typical Indosinian porphyry copper deposit in the Geshan area. In the study area, 22 vegetation samples and 22 soil samples are collected. The copper content and chlorophyll content in the soil are determined by laboratory measurements.

2.1.2 Data

In this study, FieldSpec Pro FR spectrometer of ASD (Analytical Spectral Device) is used to measure spectra of vegetation leaves. The spectral range of ASD is 350 ~ 2500 nm and the spectral data is resampled to 1nm.

The Hyperion sensor aboard on EO-1 satellite platform launched in November 2000, is the first satellite digital imaging spectrometer, which contains 242 spectral bands, ranging from 355 to 2577 nm, with the spatial resolution of 30 meters. The ASD spectrum is resampled according to the Hyperion spectral response function. To analyze the influence caused by different spectral resolution, we compare the inversion results of original ASD spectrum and the resampled spectrum.

2.2 Methods

In this paper, we mainly investigate the inversion accuracies of soil Cu element in vegetation-covered area by employing different vegetation indices according to the specific spectral resolutions of ASD and Hyperion data. The major steps of the method are as follows and Figure 1 shows the whole method scheme.

(1) Spectral resampling. The ASD spectral data is resampled according to spectral response function of Hyperion data.

(2) Calculation of the spectral indices shown in Table 2-1. The vegetation indices are calculated under the spectral resolutions of ASD and Hyperion data, respectively.

(3) Vegetation index selection. Taking the impacts of heavy metal stress on chlorophyll into account, the correlations between vegetation indices and chlorophyll content are analyzed, and the indices with correlation larger than 0.55 are selected as preference.

(4) The vegetation indices calculated by ASD data and by the resampled spectrum are used as independent variables, to establish a multiple regression model, including partial least squares (PLS) analysis and support vector machine (SVM) model, with 80% of the measured soil copper content.

(5) Accuracy assessment. The inversed copper content from different spectral resolutions are statistically analyzed with the measured values, to obtain the inversion accuracies under different situations.

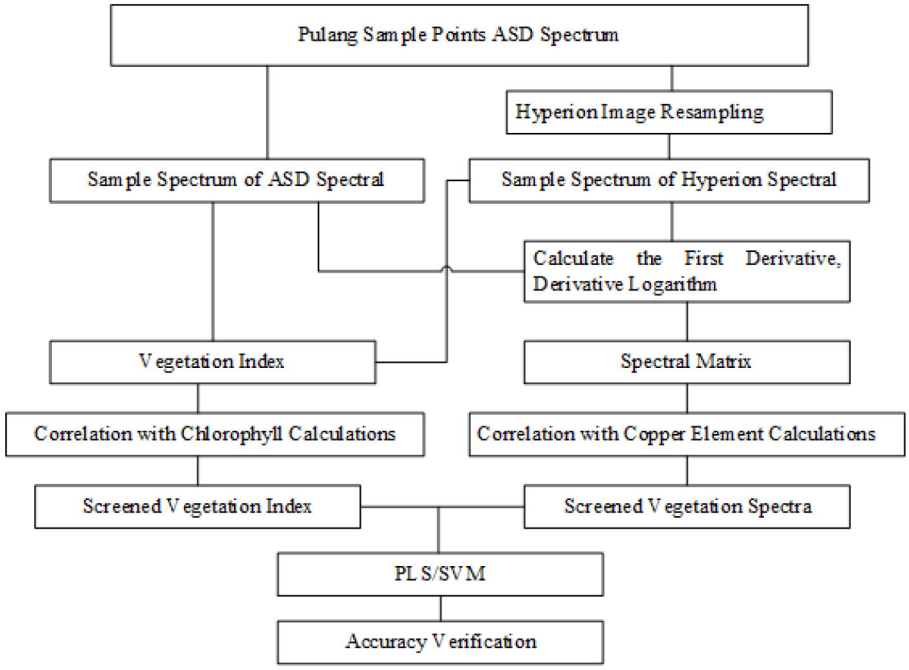

Figure 1. The methodology scheme of this study

2.2.1 Vegetation index

The vegetation spectral indices, which are sensitive to chlorophyll, are investigated taking the vegetation stress into account, and 64 different vegetation spectral index according to literatures (see Table 1) are tested. These spectral indices are modeled at different spectral resolutions.

Table 1. VI (Vegetation index) used in this study

No.	VI	Calculation formula	References
1	BGI1	BGI1=R400/R550	Zarco-Tejada, *et al*. 2005
2	BGI2	BGI2=R450/R550	
3	BRI1	BRI1=R400/R690	
4	BRI2	BRI2=R450/R690	
5	CIgreen	CIgreen=R800/R750-1	Gitelson, *et al*.2005
6	CIrededge	CIrededge=R750/R710-1	Gitelson, *et al*.2005
7	DCNI	DCNI=(R720-R700)/(R700-R670)/(R720-R670+0.03)	Chen, *et al*.,1995
8	GreenNDVI	GreenNDVI=(R750-R550)/(R750+R550)	Gitelson,1994
9	HI	HI=(R534-R698)/(R534+R698)-R704/2	Mahlein, *et al*. 2013
10	LCI	LCI=(R850-R710)/(R850+R680)	Le Maire, *et al*.2004
11	MCARI	MCARI=R700-R670-0.2*(R700-R550)*(R70	Daughtry,2000

		0/R670)	
12	MCARI/ MTVI2	MTVI2=1.5*(1.2*(R800-R550)-2.5*(R670-R550))/sqrt((2*R800+1)*2-(6*R800-5*sqrt(R670))-0.5)	Eitel, *et al*.,2007
13	MCARI_OSAVI	MCARI_OSAVI=MCARI/OSAVI	Eitel, *et al*.2007
14	MCARI2	MCARI2=[1.5*(2.5*(R800-R670)-1.3*(R800-R550))]/[sqrt((2*R800+1)^2-(6*R800-5*sqrt(R670))-0.5)]	Haboudane. *et al*. 2004
15	MSAVI	MSAVI=(0.5*R800+1-sqrt((2*R800+1)^2-8*(R800-R670)))/2	Qi, *et al*.1994
16	MSR705	MSR705=(R750-R445)/(R705-R455)	Sims & Gamon,2002
17	MTCI	MTCI=(R750-R710)/(R710-R680)	Jadun&an, *et al*.,2004
18	MTVI	MTVI=1.2*(1.2*(R800-R550)-2.5*(R670-R550))	Haboudane, *et al*.2004
19	NDPI	NDPI=(R680-R430)/(R680+R430)	Penuelas, *et al*.1995
20	NDVI(g-b)	NDVI(g-b)=(R575-R440)/(R575+R440)	Hansen, *et al*.2003
21	NDVI3	NDVI3=(R800-R670)/(R800+R670)	Rouse, *et al*.1974
22	NPCI	NPCI=(R680-R430)/(R680+R430)	Peñuelas, *et al*. 1993
23	NPQI	NPQI=(R415-R435)/(R415+R435)	Barnes,*et al*.1992
24	NRI	NRI=(R560-R670)/(R560+R670)	Schleicher,2001
25	OSAVI	OSAVI=1.16(R800-R670)(R800+R670+0.16)	Rondeaux, *et al*. 1996
26	PI	PI=(R750-R705)/(R750+R705)	Gitelson,1994
27	PI2	PI2=(R780-R550)/(R780+R550)	Gitelson,1994
28	PPR	PPR=(R550-R450)/(R550+R450)	Jacquemoud,1994
29	PRI	PRI=R675*R690/(R683)^2	Meroni, *et al*.2009
30	PRI0	PRI0=(R570-R531)/(R570+R531)	Gamon,1992
31	PRI1	PRI1=(R550-R531)/(R550+R531)	
32	PRI2	PRI2=R750/R800	
33	PRI3	PRI3=R685/R655	
34	PRI4	PRI4=R680/R630	
35	PRI5	PRI5=(R685)^2/R675*R690	
36	PRI6	PRI6=diff(R688)*diff(R710)/diff((R697))^2	
37	PRI7	PRI7=diff(R705)/diff(R722)	
38	PRI8	PRI8=diff(R730)/diff(R706)	
39	PRI9	PRI9=R690/R600	
40	PSDNa	PSDNa=(R800-R680)/(R800+R680)	Blackburn,1998
41	PSDNb	PSDNb=(R800-R635)/(R800+R635)	
42	PSDNc	PSDNc=(R800-R470)/(R800+R470)	
43	PSSRa	PSSRa=R800/R675	Blackburn, *et al*. 1998
44	PSSRb	PSSRb=R800/R650	
45	R515_R570	R515_R570=R515/R570	Zarco-Tejada, *et al*. 2012
46	R515_R670	R515_R670=R515/R670	
47	R520_R500	R520_R500=R520/R500	
48	RDVI	RDVI=(R800-R670)/sqrt(R800+R670)	Roujean & Breon.1995
49	R-M	R-M=R750/R720-1	Gitelson, *et al*.,1975
50	RVI I	RVI I=R810/R660	Zhu, *et al*.,2008
51	RVI_II	RVI_II=R801/R560	Xue, *et al*.,2004

52	SI	SI=(R774-R677)/(R774+R677)	Zarco-Tejada, *et al*. 2009
53	SIPI	SIPI=(R800-R445)/(R800-R550)	Penuelas, *et al*.,1995
54	SIPI2	SIPI2=(R445-R800)/(R445+R550)	Peñuelas & Filella ,1998
55	SR	SR=R750/R550	Gitelson,1994
56	SR2	SR2=R750/R710	Zarco-Tejada, *et al*. 2004
57	SR705	SR705=R750/R705	Sims & Gamon,2002
58	SRI	SRI=R801/R670	Deering,*et al*.,1975
59	TCARI	TCARI=3*((R700-R670)-0.2*(R700-R550)*(R700/R670))	Haboudane, *et al*.,2002
60	TCARI_OSAVI	TCARI_OSAVI =TCARI/ OSAVI	
61	TCARI_MSAVI	TCARI_OSAVI= TCARI/MSAVI	
62	TVI	TVI=0.5*(120*(R750-R550)-200*(R670-R550))	Broge & Leblanc,2001
63	VIopt	VIopt=1.45*(R800^2+1)/(R670+0.45)	Reyniers, *et al*.,2006
64	VOG4	vog4=diff(R715)/diff(R705)	Zarco-Tejada, *et al*.1999

2.2.2 Regression model

2.2.2.1 Partial Least Squares (PLS) method Regression Model

PLS is a multivariate analysis method developed in recent decades. It is able to achieve regression modeling (multiple linear regression), data structure simplification (principal component analysis), and correlation analysis between two variable sets (typical correlation analysis) to solve the problem of multiple collinearity between variables.

PLS regression has the advantages including:

(1) Carrying out regression modeling even if independent variables have serious multiple correlations.
(2) Allowing regression modeling when the number of sample points is less than variables.
(3) Containing all of the original independent variables in the final model.
(4) Making it easier to identify system information and noise (even some non-random noise).
(5) The regression coefficients of each independent variable are easy to be interpreted.

2.2.2.2 Support Vector Machine (SVM) Regression Model

SVM is a supervised approach, widely used in statistical classification and regression analysis. It is an excellent way to realize the idea of structural risk minimization. Its machine learning strategy is the principle of structural risk minimization, and in order to minimize the expected risk, the experience risk and confidence range should be minimized at the same time.

SVM is a novel small sample learning method with solid theoretical basis. It is basically not involved in the probability measure and the law of large numbers, so it is different from the existing statistical methods. In essence, it avoids the traditional process from induction to deduction, and achieves efficient.

The final decision function of SVM is determined by a small number of support vectors, and the computational complexity depends on the number of support vectors, not the dimension of the sample space, which in some sense avoids the "dimensionality disaster".

In this study, we mainly utilize the partial least square method in the inversion model of soil copper content in vegetation-covered area

2.2.3 Accuracy verification

In this study, 80% of the samples are randomly selected as training samples for the least square method, and the rest 20% are used to verify the accuracy of the model. Meanwhile the accuracy verification of SVM model is based on cross validation. Cross validation is primarily used for modeling applications. In a given modeling sample, we should take out most of the samples to build models, leave a small number of samples with the newly established model to predict, calculate the prediction error of this small samples, and record their squared sums. This process has been carried out until all the samples have been predicted once and only once. But Leave-One-Out is a special cross validation method, that is, leaving only one sample for verification, and the remaining samples are for modeling.

3. RESULT

The results show that the vegetation indices calculated by the ASD data and the resampled data both have good inversion results for the soil copper element. The goodness of fit of PLS model with the resampled data is above 0.9, and those with ASD is a little better, ~0.9455. We use the remaining 20% of the sample data as preliminary validation of inversions at different spectral resolutions. Using the ASD data, the correlation coefficient between the copper content and the measured value is 0.8753 and the average relative error is 3.4%. The correlation coefficient between the copper content and the measured value is estimated to be 0.7862 using the resampled data, and the average relative error is 4%, respectively. Prediction of soil copper content and actual soil copper content comparison are shown in Figure 2. The sum of squared errors of SVM fitting model with ASD data is 12.988, and that with the resampled data is 43.864. So the result of ASD spectral resolution has a better fitting effect.

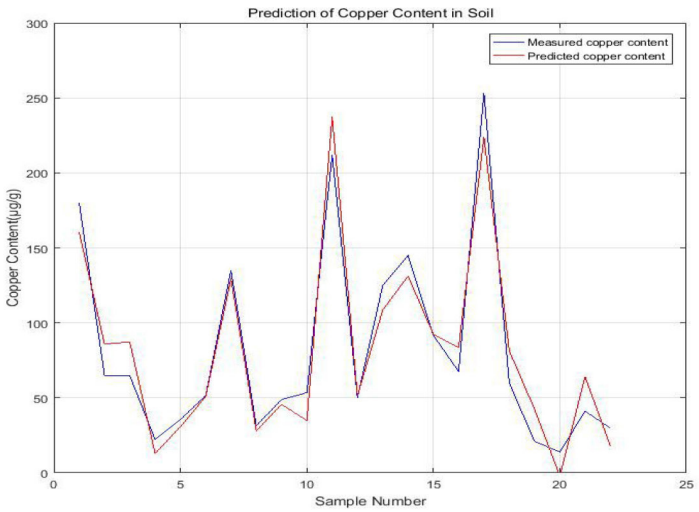

Figure 2. Prediction of Copper Content in Soil

[10] Jacquemoud S., Ustin S. L., Verdebout J., *et al.* " Estimating leaf biochemistry using the PROSPECT leaf optical properties model" Remote sensing of environment, 1996, 56(3): 194-202.
[11] Schleicher T. D., Bausch W. C., Delgado J. A., *et al.* "Evaluation and refinement of the nitrogen reflectance index (NRI) for site-specific fertilizer management"//2001 ASAE Annual International Meeting, St-Joseph, MI, USA. ASAE Paper. 2001 (01-11151).
[12] Le Maire G., Francois C., Dufrene E. "Towards universal broad leaf chlorophyll indices using PROSPECT simulated database and hyperspectral reflectance measurements" Remote sensing of environment, 2004, 89(1): 1-28.
[13] Haboudane D., Miller J. R., Tremblay N., *et al.* " Integrated narrow-band vegetation indices for prediction of crop chlorophyll content for application to precision agriculture" Remote sensing of environment, 2002, 81(2): 416-426.
[14] Daughtry C. S. T., Walthall C. L., Kim M. S., *et al.* "Estimating corn leaf chlorophyll concentration from leaf and canopy reflectance" Remote sensing of Environment, 2000, 74(2): 229-239.
[15] Zarco-Tejada P. J., Miller J. R. "Land cover mapping at BOREAS using red edge spectral parameters from CASI imagery" Journal of Geophysical Research: Atmospheres (1984–2012), 1999, 104(D22): 27921-27933.
[16] Qi J., Chehbouni A., Huete A. R., *et al.* "A modified soil adjusted vegetation index" Remote sensing of environment, 1994, 48(2): 119-126.
[17] Rondeaux G., Steven M., Baret F. "Optimization of soil-adjusted vegetation indices" Remote Sensing of Environment, 1996, 55(2): 95-107.
[18] Meroni M., Rossini M., Guanter L., *et al.* "Remote sensing of solar-induced chlorophyll fluorescence: Review of methods and applications" Remote Sensing of Environment, 2009, 113(10): 2037-2051.
[19] Zarco-Tejada P. J., González-Dugo V., Berni J. A. J. "Fluorescence, temperature and narrow-band indices acquired from a UAV platform for water stress detection using a micro-hyperspectral imager and a thermal camera" Remote Sensing of Environment, 2012, 117: 322-337.

PROCEEDINGS OF SPIE

SPIEDigitalLibrary.org/conference-proceedings-of-spie

Comparison of water extraction methods in Tibet based on GF-1 data

Lingjun Jia, Kun Shang, Jing Liu, Zhongqing Sun

Lingjun Jia, Kun Shang, Jing Liu, Zhongqing Sun, "Comparison of water extraction methods in Tibet based on GF-1 data," Proc. SPIE 10611, MIPPR 2017: Remote Sensing Image Processing, Geographic Information Systems, and Other Applications, 106110P (8 March 2018); doi: 10.1117/12.2288734

SPIE.

Event: Tenth International Symposium on Multispectral Image Processing and Pattern Recognition (MIPPR2017), 2017, Xiangyang, China

Comparison of Water Extraction Methods in Tibet Based on GF-1 Data

Lingjun Jia[a,b], Kun Shang[*a], Jing Liu[b], Zhongqing Sun[a,b]
[a]China Aero Geophysical Survey and Remote Sensing Center for Land and Resources, No.31 Xueyuan Rd. Haidian District, Beijing, China 100083; [b]China University of Geosciences (Beijing), No.29 Xueyuan Rd. Haidian District, Beijing, China 100083

ABSTRACT

In this study, we compared four different water extraction methods with GF-1 data according to different water types in Tibet, including Support Vector Machine (SVM), Principal Component Analysis (PCA), Decision Tree Classifier based on False Normalized Difference Water Index (FNDWI-DTC), and PCA-SVM. The results show that all of the four methods can extract large area water body, but only SVM and PCA-SVM can obtain satisfying extraction results for small size water body. The methods were evaluated by both overall accuracy (OAA) and Kappa coefficient (KC). The OAA of PCA-SVM, SVM, FNDWI-DTC, PCA are 96.68%, 94.23%, 93.99%, 93.01%, and the KCs are 0.9308, 0.8995, 0.8962, 0.8842, respectively, in consistent with visual inspection. In summary, SVM is better for narrow rivers extraction and PCA-SVM is suitable for water extraction of various types. As for dark blue lakes, the methods using PCA can extract more quickly and accurately.

Key words: Tibet; water extraction; GF-1 data

1. INTRODUCTION

Water resource plays a key role in Tibet. For example, local farms, pasture lands, and electric power generation are all in great need of water resource. The distribution of water resource is also part of the basic data of hydrological model. Therefore, it is necessary to monitor the water resource in Tibet. Satellite remote sensing, as a high-tech approach developed in recent decades, is able to not only identify the distribution of water resource quickly and accurately, but also save a lot of manpower and material resources especially for some dangerous areas.

GF-1 is equipped with two scanners of 2m resolution panchromatic and 8m resolution and 4 multispectral scanners of 16m resolution launched by China in 2013. At present, domestic and foreign scholars have conducted lots of research on water resource monitoring using GF-1 data and obtained reliable results [1-3]. Ke *et al.* proposed that PCA (Principal Component Analysis) method, compared to other water extraction methods, could reach to more accurate water boundary extraction [1]. Li *et al.* obtained small rivers in hilly areas information and effectively eliminated the interference of shadows

*shangkun0213@126.com; phone:86-10-62060320

MIPPR 2017: Remote Sensing Image Processing, Geographic Information Systems, and Other Applications, edited by Nong Sang, Jie Ma, Zhong Chen, Proc. of SPIE Vol. 10611, 106110P · © 2018 SPIE
CCC code: 0277-786X/18/$18 · doi: 10.1117/12.2288734

and salt and pepper phenomenon by MRMAS (Modified Ratio of Mean Difference to Neighbors (ABS) to Standard Deviation) [4]. Chen *et al.* found that snow and bare soil could be eliminated by using DTC to extract water body in mountainous area effectively [5]. Huang *et al.* used object-oriented classification to avoid salt and pepper noise and patch fragmentation [6]. Wang *et al.* used improved SWI (Shade Water Index) to extract water body and obtained good results in arid area [7].

There are different types of water resource in Tibet, including saltwater lake, freshwater lake, permanent stream, ephemeral stream, and glacier and so on. However, how to choose an appropriate way to extract water information of different types still needs further study. In this study, we compare different methods of water information extraction using GF-1 satellite image and analyze the performances of different methods for each type of water body.

2. DATA

2.1 Data resource

GF-1 satellite that launched on April 26, 2013 is the first high resolution earth observing satellite of China, the height of the sun-synchronous recursive orbit is 645 km. Based on the high temporal resolution (revisit cycle of four days) and high spatial resolution (up to 2 m), GF-1 shows great potential in observing the earth. In this study, we selected the fusion images from panchromatic images of 2 m and multi-spectral images of 8 m as the main data. The multi-spectral image consists of four bands of blue, green, red and near infrared (0.45-0.52μm、0.52-0.59μm、0.63-0.69μm、0.77-0.89μm). All of the images are cloudless and well qualified.

2.2 Study area

The study area, located in Tibet, is part of the south-west China plateau with an average elevation of 4650 m and is about 18.15 kilometers northwest of the Bam Co (90°17′30″~90°21′30″E, 31°19′30″~31°22′00″N). Because of the wide distribution of lakes and the complicated water types, this study area is the key region of remote sensing investigation.

3. METHODOLOGY

We compared SVM (Support Vector Machine), PCA (Principal Component Analysis), FNDWI -DTC (False Normalized Difference Water Index - Decision Tree Classification) and PCA-SVM (Principal Component Analysis - Support Vector Machine) to analyze the extraction results of different water body types.

3.1 Data pre-processing

Based on ENVI software, the pre-processing of GF-1 satellite images includes the following steps. First, we calibrate the radiometric by using the coefficients of gain and offset. Then, we perform the atmosphere calibration with the FLAASH (Fast Line-of-sight Atmospheric Analysis of Hypercubes) model. In this step, the model is set as Mid-Latitude Summer according to the imaging time of the data. Next, the orthographic correction is performed. We uses the defaulted GMTED2010 data as DEM (Digital Elevation Model) data. The pixel size and resampling method are set to 8m and Bilinear. Last but not the least, we operate the automatic registration and use panchromatic image as base image to adjust the multispectral image. 160 control points are generated and the root-mean-square error is limited within 0.5 pixels.

Before the water information extraction, image fusion is performed by using Gram-Schmidt spectral sharpening, and the resampling method is set as cubic convolution.

3.2 PCA

The purpose of PCA is to fetch the appropriate information from different spectral bands. This method eliminates the redundant information within the bands. The principal components are linear combinations of the eigenvectors of the covariance matrices of each band weighed by coefficients. We calculate the covariance matrix of each band, and then calculate the eigenvalues and eigenvectors of the covariance matrix. Assuming that the image has n bands, and λp represents the P-band eigenvalues (P = 1, 2, 3 ... n), the percentage of the total variance of the original data contained in each principal component can be expressed as:

$$\%_{\mathrm{p}} = \left(\lambda_{\mathrm{p}} \times 100\right) / \sum_{\mathrm{i}=1}^{\mathrm{n}} \lambda_{\mathrm{p}} \tag{1}$$

The a_{kp} represents the eigenvector between the k- band and the p-band main component, and the correlation coefficient R_{kp} between the k-band and the p-band main component can be expressed as:

$$R_{\mathrm{kp}} = \left(a_{\mathrm{kp}} \times \sqrt{\lambda_{\mathrm{p}}}\right) / \sqrt{V_{\mathrm{ark}}} \tag{2}$$

Where V_{ark} represents the variance of k-band.

The comparison of the four single principal components is shown in Figure 1, and it can be seen that PC1 image could enhance water information well. The rest of the images cannot or can only enhance a certain type of water body. Hence, we set a threshold to extract water information by using PC1 image (Figure 1). The optimal threshold for water body extraction is set based on the histograms of water and non-water samples. The gray value range of water is from -3214 to -224 while that of non-water is from -750~4217, might causing a confusion within -750~ -224. The experimental results indicate that when the critical value is set as -700, the extraction effect is the best (Figure 2).

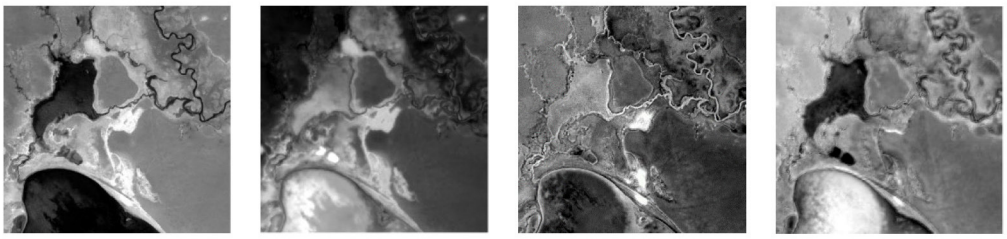

PC1 PC2 PC3 PC4

Fig1.The result of PCA

3.3 SVM

As one of the machine learning algorithms, SVM has the advantages of small quantity of training samples, no need of data dimension reduction, as well as accurate and fast classification and recognition. The method can not only extraction water information, but also obtain the classification results of all interested land cover types.

The basic theory is to use the optimal classification hyperplane to accurately separate the objects and ensure the maximum separation interval. Finding the optimal hyperplane is actually an optimization problem. The Lagrange function can be used to turn the original optimization problem into a dual optimization problem. The formula can be expressed as:

$$\max_{\alpha} L(\alpha) = \sum_{i=1}^{k} \alpha_i - \frac{1}{2} \sum_{i=1}^{k} \sum_{j=1}^{k} \alpha_i \alpha_j y_i y_j K(x_i x_j) \tag{3}$$

$$\sum_{i=1}^{k} y_i \alpha_i = 0, \alpha_i \geq 0, i = 1,2, \cdots, k \tag{4}$$

Where $K(x_i x_j)$ is a kernel function, which can map the feature space to high-dimensional space.

Roli *et al.* found that radical basis function (RBF) kernel was more suitable than polynomials and S-shaped function and had good ability of filtering noise and anti-interference [8]. Therefore, RBF is chosen in this study. We select six types of samples (grassland(A), saline soil(B), rivers(C), sky-blue lakes(D), green lakes(E), blue-grey lakes(F)), compute the separability to evaluate the sample quality, and then use SVM to perform the classification.

Table1. Number of sample in six land types

Type	A	B	C	D	E	F
Sample size	61	50	55	10	33	24

3.4 FNDWI-DTC

Compared with other algorithms, DTC has the advantages of clear structure and fast operation. Considering the flexibility of data processing, this study select a decision tree algorithm based on artificial prior knowledge, and combine FNDWI index with the original band to extract water information.

The FNDWI index proposed by Zhou *et al.* is to use brightness value of infrared band to modify green band [9]. The false green band formula is shown below.

$$FGreen = Green + S(CNIR - NIR) \tag{5}$$

Both S and CNIR are constants(S determines the magnitude of the correction, CNIR determines the threshold boundary of water and grassland). Based on near-infrared band and the modified green band, the FNDWI can be calculated as shown below.

$$FNDWI = (FGreen - NIR)/(FGreen + NIR) \tag{6}$$

There are six types of land cover in the image. When FNDWI is set greater than 11500, most of water could be separated from grassland and saline land (Fig3). We use B_1 band to separate the saline land from narrow rivers and grass land (Fig4). And we extract the narrow rivers from grass land by using $B_{1\text{-}3}$ band, which is calculated as the sum of B_1, B_2 and B_3, with the threshold set as 4315 (Fig5).

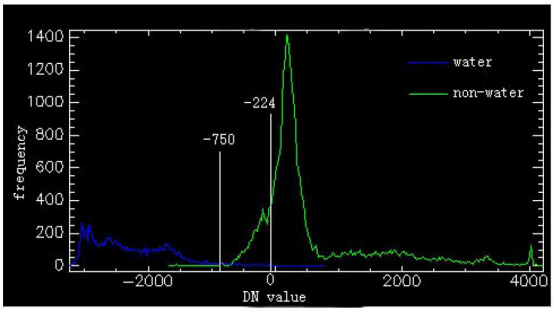

Fig2. Histogram for water and non-water in PC1

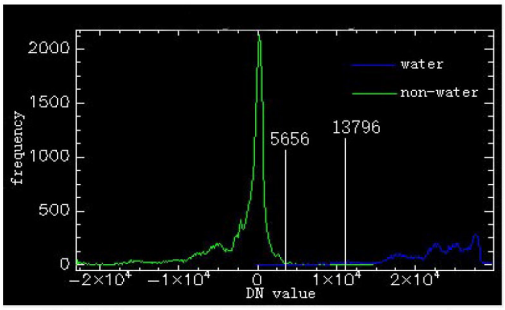

Fig3. Histogram for water and non-water in FNDWI band

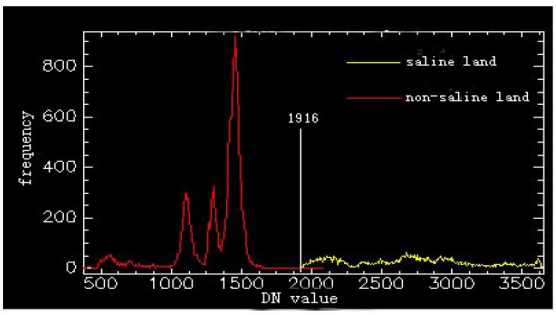

Fig4. Histogram for saline land and non-saline land in B_1 band

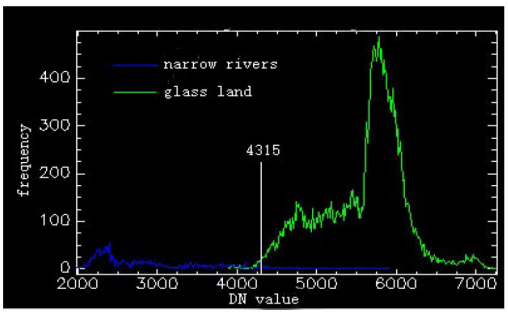

Fig5. Histogram for narrow rivers and glass land in $B_{1\text{-}3}$

3.5 PCA-SVM

The classification result of SVM could show differences of various water types, but the accuracy is not satisfying. PCA could highlight differences between water types. So we combine the two methods to improve the extraction accuracy of different water types.

J-M (Jeffreys-Matusita) distance can evaluate the separability of samples. The samples with J-M distance greater than 1.9 are supposed to have good separability. The following table shows that the separability is improved by using PCA transform. And nearly half of the J-M distances have increased, implying better separability (Table2). In the SVM classification, we set radial basis function as kernel function and leave the rest of the parameters as default values.

Table2. J-M distance matrix of six land types

	A-B	A-C	A-D	A-E	A-F	B-C	B-D	B-E
original bands	1.95	1.95	1.99	2.00	2.00	1.99	1.97	1.98
PCA	1.96	1.98	1.99	2.00	2.00	1.99	1.99	1.99
	B-F	C-D	C-E	C-F	D-E	D-F	E-F	
original bands	1.99	1.98	1.92	1.96	1.85	1.96	1.65	
PCA	1.99	1.99	1.95	1.97	1.85	1.96	1.70	

Note: A- Grassland, B-Saline Base, C-River, D-Sky Blue Lake, E-Green Lake, F-Blue Gray Lake

4. RESULTS

Figure 6 shows that all of these four methods can extract water body of large area. PCA-SVM is the best method to extract water bodies containing various types, and SVM and FNDWI-DTC are better for narrow river extraction. As for dark blue lakes, PCA can extract them quickly and accurately. As shown in Table 3, the accuracy of the PCA-SVM method is the highest, followed by SVM and FNDWI-DTC, and PCA obtains the lowest accuracy. Compared with other methods, the omission rate of FNDWI-DTC is a little higher. SVM could extract the rivers with more detailed information, while PCA improves the precision for dark blue water extraction, and both of the two methods could extract green water very well. As shown in the results, the combination of PCA and SVM presented in this study can reduce classification errors caused by wetlands, making the PCA-SVM method a simple yet effective method of water extraction.

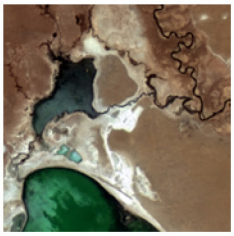

GF-1 image

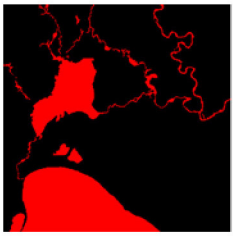

The actual distribution of water bodies

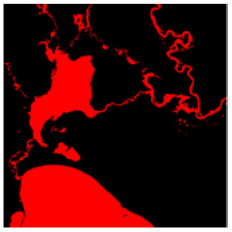

(a) SVM

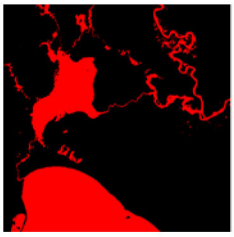

(b) PCA

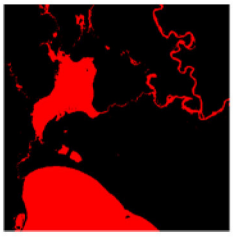

(c) FNDWI-DTC

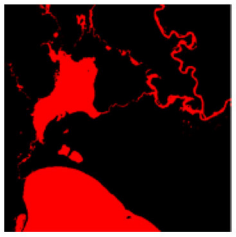

(d) PCA-SVM

Fig.6 Water extraction results of different methods

Table3. Water extraction accuracy of different methods

	Overall accuracy	Kappa
PCA	93.01%	0.8842
SVM	94.23%	0.8995
FNDWI-DTC	93.99%	0.8962
PCA-SVM	96.68%	0.9308

5. CONCLUSIONS

In this study, different water extraction methods were compared according to different water types in Tibet. Based on GF-1 satellite images over Bam Co region, the extraction performances of water body in Tibet by different method were compared and evaluated, including SVM, PCA, FNDWI-DTC and PCA-SVM. The results showed that all the four methods could obtain good results but each had its own appropriate scenarios. Besides, how to extract water body of different types together and to achieve higher accuracy should be investigated more in future, which can provide supports for water resource research in Tibet.

ACKNOWLEDGMENT

This work was supported in part by the Geological Survey Program of China Geological Survey Bureau under Grant 121201203000160007, and in part by the Chinese Major Project of High Resolution Earth Observation System under Grant 04-Y20A36-9001-15/17.

REFERENCES

[1] Lijuan Ke, Lihong Zhao, Yunzhong Jiang. "Comparison of Methods for Extracting Water Based on G F-1 Satellite Remote Sensing Image." Gansu Science and Technology. Papers 31 (10), 18-35(2015)

[2] Jinsong Deng, Ke Wang, Yanhua Deng, Qinjuan Huang. "An Effective way for automatically extracting water body information from SPOT-5 images." Journal of Shanghai Jiao Tong University (Agricultural Science). Papers 3(2), 198-201(2005)

[3] Jinkang Du, Yongsheng Huang, Xuezhi Feng, Zhoulong Wang. "Study on water bodies extraction and classification from SPOT image." Journal of Remote Sensing. Papers 5(3), 214-219(2001)

[4] Yanhua Li, Jianli Ding, Renhua Yan. "Extraction of small river information based on China-made GF-1 remote sense images." Resources Science. Papers 37(2), 408-416(2015)

[5] Wenqian Chen, Jianli Ding, Yanhua Li, Zengyi Niu. "Extraction of water information based on China-made GF-1 remote sense images." Resources Science. Papers37(6), 1166-1172(20-15)

[6] Shuai Huang. "Reseach on automatic extraction algorithm of enclosure culture area in Yangcheng lake ased on ZY-3 image." Proc. 1-57(2017)

[7] Jinjie Wang, Jianli Ding, Cheng Zhang, Wenqian Cheng. "Method of information extraction by improved SWI based on GF-1 satellite image." Remote sensing for land & resources. Papers 29(1), 29-35(2017)

[8] Fabio Roli, Giorgio Fumera. "Support vector machines for remote-sensing image classification." Image and Signal Processing for Remote Sensing. PapersVI, 160-166(2001)

[9] Yi Zhou, Guanglei,Xie, Shixin Wang, Feng Wang. Wang Futao. "Information extraction of thin rivers around build-up lands with false NDWI." Journal of Geo-information Science. Papers 16(1), 102-107(2014)

2018 Fifth International Workshop on Earth Observation and Remote Sensing Applications

Emissivity image generation of Gaofen-5's thermal infrared bands using ASTER data

Yao liu*
China Aero Geophysical Survey and Remote Sensing Center for Land and Resources
Beijing, China
Corresponding author: yao.liu_agrs@foxmail.com

Chenchao Xiao
China Aero Geophysical Survey and Remote Sensing Center for Land and Resources
Beijing, China
xcc_surpass@qq.com

***Abstract*—To explore the application of Gaofen-5's thermal infrared (TIR) data, algorithm development and validations needs to be conducted before its launch; and image simulation is necessary to provide datasets for such research. In this paper, using ASTER imagery as the data source, a simulation method is proposed for Gaofen-5's four TIR bands' emissivity images. For the first 3 bands, emissivity images are generated through translation models built on spectral correlation between emissivity of Gaofen-5 bands and those of ASTER bands. For the 4th TIR band of Gaofen-5, we propose a spectral matching and spectral mixing method for emissivity image generation. To test the feasibility of our simulation method, ASTER thermal infrared emissivities are simulated and then compared with their actual values. Average relative errors of these simulated emissivities are 4.04%, 2.98%, 1.74%, -4.02% and -2.79% in 5 ASTER TIR bands, indicating that our proposed method can be used for emissivity image generation.**

Keywords—Gaofen-5, surface emissivity, image simulation, ASTER

I. INTRODUCTION

The Gaofen-5 (GF-5) satellite is the fifth flight unit in China High-resolution Earth Observation System (CHEOS). It carries six payloads and has been launched on March 9, 2018. In CHEOS, GF-5 is the only one that provides a thermal infrared (TIR) payload, which has four channels centered at 8.20 (8.01–8.39 μm), 8.63 (8.42–8.83 μm), 10.80 (10.30–11.30 μm), and 11.95 μm (11.40–12.50 μm) [1]. In addition, all these four channels have a spatial resolution of 40m, which is much higher than that of previous launched satellites (e.g., ASTER (90m), Landsat 8 (100m)). With such specifications, we see its potential of being used for land observation applications such as environmental protection and natural resources exploration, combined with its visible to short-wave infrared images, as well as GF-5's hyperspectral images. As such, it is necessary to conduct researches regarding its data processing and application.

Actual GF-5's thermal infrared data is unavailable before launch, simulated imagery is therefore required for purpose of algorithm development and validation. The at-sensor radiance ($L_\lambda^{at-sensor}$) in thermal infrared region for a given wavelength (λ) can be calculated according to radiative transfer equation as following:

$$L_\lambda^{at-sensor} = \left[\varepsilon_\lambda B(\lambda, T_s) + (1-\varepsilon_\lambda)L_\lambda^{atm\downarrow}\right]\tau_\lambda + L_\lambda^{atm\uparrow} \quad (1)$$

where ε_λ is the surface emissivity, τ_λ is the total transmissivity of atmosphere on the upwelling radiative transfer path, $L_\lambda^{atm\downarrow}$ and $L_\lambda^{atm\uparrow}$ are downwelling and upwelling atmospheric radiance respectively, $B(\lambda, T_s)$ is the radiance emitted by a blackbody at temperature T_s and it's defined by Planck's law. From (1) we know that simulating thermal infrared radiance requires surface emissivity and temperature, as well as atmospheric parameters (i.e., τ_λ, $L_\lambda^{atm\downarrow}$ and $L_\lambda^{atm\uparrow}$). To use existing remote sensing imagery as the simulation data source, the surface temperature image can be retrieved using LST retrieval algorithms [2]. Meanwhile, atmospheric parameters can be accurately calculated from radiative transfer code (such as MODTRAN [3]). Thus, the focus of image simulation for GF-5's TIR bands is the corresponding emissivity image generation. In this paper, we propose a simulation method for generating GF-5's TIR emissivity images using ASTER imagery as our data source.

II. APPROACH

A. Data source selection

We choose ASTER as the data source of image simulation, mainly because it has similar spatial resolution and spectral ranges (see Fig. 1) as Gaofen-5's TIR bands. ASTER has 14 bands: 4 visible to near-infrared (VNIR) bands, 5 short-wave infrared (SWIR) bands, and 5 thermal infrared bands. Detailed ASTER satellite sensor specifications are given in Table I.

TABLE I. ASTER SATELLITE SENSOR SPECIFICATIONS

	Band	Spectral Range (μm)	Spatial Resolution (m)
VNIR	Band1	0.52~0.60	15
	Band2	0.63~0.69	
	Band3	0.76~0.86	
	Band4	1.60~1.70	30
SWIR	Band5	2.145~2.185	30
	Band6	2.185~2.225	
	Band7	2.235~2.285	
	Band8	2.295~2.365	

978-1-5386-6642-5/18/$31.00 ©2018 IEEE

	Band9	2.36~2.43	
TIR	Band10	8.125~8.475	90
	Band11	8.475~8.825	
	Band12	8.925~9.275	
	Band13	10.25~10.95	
	Band14	10.95~11.65	

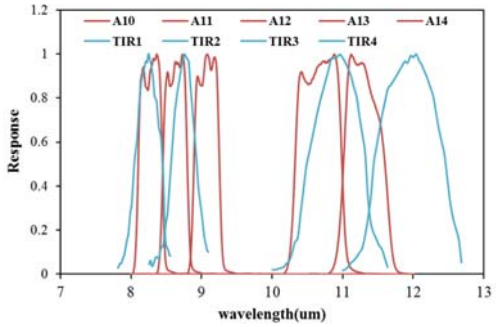

Fig. 1. Spectral response functions of GF-5's (TIR1-4) and ASTER's (A10-14) thermal infrared bands.

B. Simulation method

First, as revealed in Fig. 1, TIR band ranges are similar between ASTER and GF-5; therefore, we consider to simulate GF-5's TIR emissivity image based on their spectral correlation with surface emissivity in ASTER's TIR bands. To conduct this correlation analysis, 149 spectra from JHU (Johns Hopkins University) [4] spectral library and 85 spectra from ASU (Arizona State University) spectral library [5] are used.

Through correlation analysis using these spectra, we found that emissivities in GF-5's first three TIR bands has a linear correlation with ASTER's bands, as displayed in Fig. 2. Specifically, band TIR1-3 has the highest correlation with ASTER band 10, band 11, and band 13, respectively; and the coefficient of determination (R^2) are all higher than 0.95. This shows that TIR1-3 emissivity images can be then generated using translation models (i.e. equations in Fig. 2).

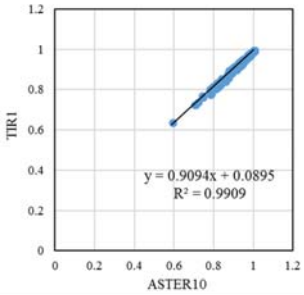

(a) TIR1 band

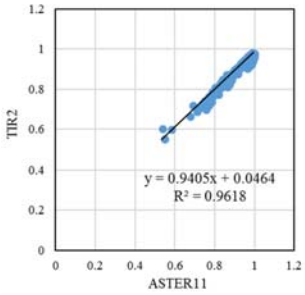

(b) TIR2 band

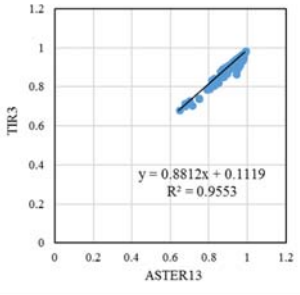

(c) TIR3 band

Fig. 2. Correlation between emissivity of GF-5's TIR bands and ASTER bands.

However, correlation analysis also shows that emissivity in GF-5's fourth TIR band has no good correlation with any of ASTER's TIR bands. Therefore, we come up with a different simulation strategy for TIR4 band emissivity using ASTER data. Considering that ASTER has 14 bands covering visible to thermal infrared range, we use spectral matching and spectral mixing to perform the simulation, which has four steps. First, pure pixels in the ASTER reflectance/emissivity image are selected to extract endmember spectra. Second, spectral matching is performed between extracted endmembers on the image and materials from spectral library. Those spectral library materials (referred as surface endmembers) that are most similar to image endmembers are then used as endmember for abundance inversion on ASTER's reflectance/emissivity images. Third, abundance maps are retrieved based on linear spectral unmixing model. Finally, with spectral emissivity in four TIR channels of surface endmembers and abundance maps, spectra are mixed to generate Gaofen-5's TIR band emissivity images. To achieve simulation using this method, measured spectra from spectral library has to cover the spectral range of both the data source (i.e. all ASTER's bands) and the simulated payload (i.e. GF-5's TIR4 bands).

III. Experiments and Results

A. Experiment Data

ASTER data used in the simulation experiment was collected on September 27, 2004, and the ground area is located in the north of Liuyuan Town, Gansu Province.

B. Data preprocessing

Atmospheric correction should be conducted on ASTER's radiance data to retrieve reflectance image in band 1-9, as well as emissivity images in band 10-14. For band 1-9, atmospheric correction was performed using FLAASH module in ENVI 5.2. Emissivity images in band 10-14 was retrieved using the Temperature Emissivity Separation (TES) algorithm [6]. As reflectance images of band 8-9 has a number of invalid values, only band 1-7 and band 9-14 images are then used for spectral unmixing in the simulation for TIR4 emissivity image.

C. Simulation process

Using emissivity images of ASTER band 10, band 11, and band 13, GF-5's TIR1-3 emissivity images were generated based on translation models built on spectral correlation analysis displayed in Fig. 2. TIR4 emissivity image was then simulated using the second method step by step. First, 4 endmembers were determined on the image. Statistics shows that pixels consisting of these 4 endmembers account for over 99% of the image. Second, spectral angle matching was conducted between spectra of JHU spectral library materials and that of 4 image endmembers. JHU library materials with the highest cosine which were also greater than 0.985 were selected as surface endmembers. Third, spectral unmixing was performed on ASTER's reflectance and emissivity images (a total of 12 bands) with selected surface endmembers, and abundance maps were acquired. Finally, TIR4 band emissivity image was generated from linear spectral mixing using abundance maps and TIR4 band emissivity spectra from surface endmembers. Simulated emissivity images of GF-5's TIR bands are shown in Fig. 3.

D. Accuracy analysis

Since true GF-5's TIR emissivity data is unavailable, accuracy analysis is performed to evaluate the feasibility of our simulation method. Therefore, ASTER TIR emissivity for JHU materials were simulated using method proposed here and compared with their actual emissivity values. The average relative errors (RE) were then calculated for five ASTER TIR band emissivities. Average REs of the bands are 4.04%, 2.98%, 1.74%, -4.02% and -2.79%, indicating that simulated emissivities are close to actual ones.

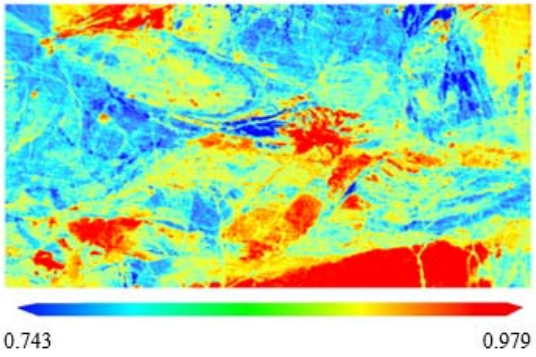

(a) TIR1 band

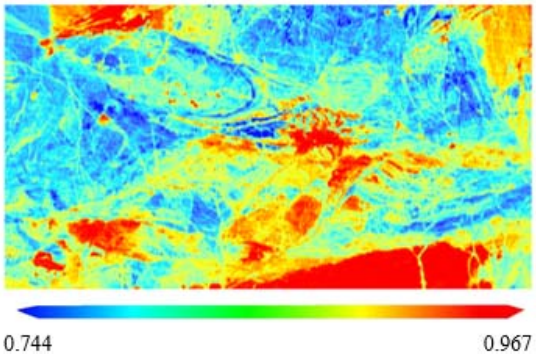

(b) TIR2 band

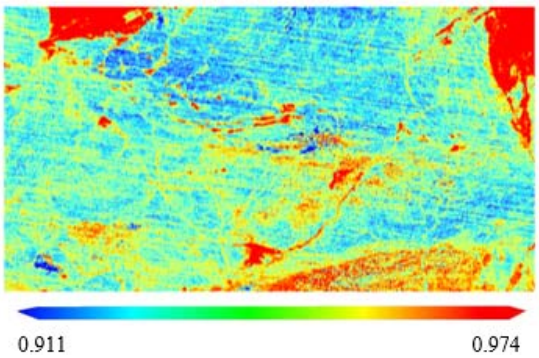

(c) TIR3 band

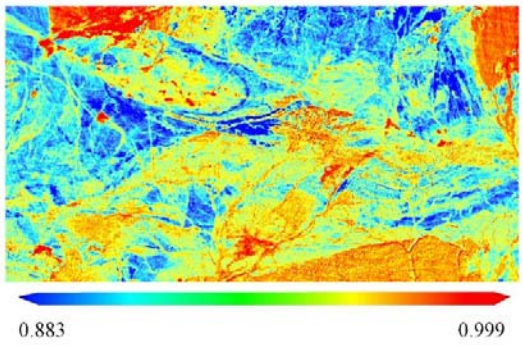

(d) TIR4 band

Fig. 3. Simulated emissivity images in GF-5's TIR bands.

IV. Conclusion

In this paper, a simulation method is proposed for emissivity image generation of Gaofen-5's thermal infrared bands. ASTER data is selected as the simulation source considering its similar spatial and spectral resolution with GF-5's TIR bands. As actual GF-5 data has not been acquired yet, accuracy analysis has been conducted for the simulation method, which is used for simulating ASTER TIR band emissivity. Relative errors show the proposed simulation method here is feasible for TIR emissivity image generation.

Acknowledgment

This work was supported by the Chinese Major Project of High Resolution Earth Observation System under Grant 30-Y20A30-9003-15/17.

References

[1] X. Ye, H. Ren, R. Liu, Q. Qin, Y. Liu, J. Dong, "Land surface temperature estimate from chinese gaofen-5 satellite data using split-window algorithm," *IEEE Transactions on Geoscience and Remote Sensing*, vol. 55, no. 10, pp. 5877-5888, 2013.

[2] Z. L. Li, B. H.Tang, H. Wu, H. Ren, G. Yan, Z. Wan. "Satellite-derived land surface temperature: current status and perspectives," *Remote Sensing of Environment,* vol. 131, pp. 14-37, 2013.

[3] A. Berk, L. S. Bernstein, D. C. Robertson, MODTRAN: A Moderate Resolution Model for LOWTRAN 7, Technical Report GL-TR-89-0122, Geophys. Lab, Bedford, MA, 1989.

[4] A. M. Baldridge, S. J. Hook, C. I. Grove, G. Rivera, “The aster spectral library version 2.0,” *Remote Sensing of Environment, 113*(4), 711-715, 2009.

[5] http://speclib.asu.edu/

[6] A. Gillespie, S. Rokugawa, T. Matsunaga, J. S. Cothern, S. Hook, A. B. Kahle, “A temperature and emissivity separation algorithm for advanced spaceborne thermal emission and reflection radiometer (aster) images,” *IEEE Transactions on Geoscience and Remote Sensing,* vol. 36, no. 4, pp. 1113-1126, 2002.

MINERAL INFORMATION EXTRACTION BASED ON GAOFEN-5’S THERMAL INFRARED DATA

Yao Liu [1, *], Kun Shang [1]

[1] China Aero Geophysical Survey and Remote Sensing Center for Land and Resources, Beijing, China, - yao.liu_agrs@foxmail.com, shangkun0213@126.com

KEY WORDS: Gaofen-5, thermal infrared, emissivity spectra, mineral information extraction, image simulation

ABSTRACT:

Gaofen-5 carries six instruments aimed at various land and atmosphere applications, and it’s an important unit of China High-resolution Earth Observation System. As Gaofen-5’s thermal infrared payload is similar to that of ASTER, which is widely used in mineral exploration, application of Gaofen-5’s thermal infrared data is discussed regarding its capability in mineral classification and silica content estimation. First, spectra of silicate, carbonate, sulfate minerals from a spectral library are used to conduct spectral feature analysis on Gaofen-5’s thermal infrared emissivities. Spectral indices of band emissivities are proposed, and by setting thresholds of these spectral indices, it can classify three types of minerals mentioned above. This classification method is tested on a simulated Gaofen-5 emissivity image. With samples acquired from the study area, this method is proven to be feasible. Second, with band emissivities of silicate and their silica content from the same spectral library, correlation models have been tried to be built for silica content inversion. However, the highest correlation coefficient is merely 0.592, which is much lower than that of correlation model built on ASTER thermal infrared emissivity. It can be concluded that GF-5’s thermal infrared data can be utilized in mineral classification but not in silica content inversion.

1. INTRODUCTION

Gaofen-5 (GF-5) satellite is the fifth flight unit of China High-resolution Earth Observation System (CHEOS) and will be launched in 2018. GF-5 will be carrying six types of instruments, including visible and short-wave infrared hyper-spectral camera, spectral imager, greenhouse gas detector, atmospheric environment infrared detector at very high spectral resolution, differential absorption spectrometer for atmospheric trace gas, and multi-angle polarization detector, with a designed lifespan of 8 years. Its thermal infrared (TIR) payload on the spectral imager will collect land surface thermal emission in four channels, which are centered at 8.20μm (TIR1), 8.63μm (TIR2), 10.80μm (TIR3) and 11.95μm (TIR4) with a spatial resolution of 40 m (Ye et al., 2017). Such spectral range settings are similar to the thermal infrared bands of ASTER instrument (see Figure 1).

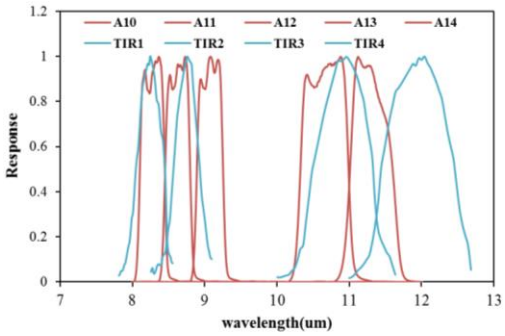

Figure 1. Spectral response functions of GF-5 TIR (TIR1-4) and ASTER TIR (A10-14) channels.

Previous research and applications show that ASTER TIR data has been successfully used to delineate mineral zones and assemblages of carbonate and silica (Kanlinowski et al., 2004). Specifically, sulfate, carbonate, and silicate minerals can be classified on ASTER images based on their difference of spectral features in thermal infrared bands (Ninomiya, et al., 2003). Also, the content of silica in silicate minerals can be estimated using ASTER TIR data; as silica is the main component of the earth's crust, and its content is an important chemical parameter for the classification of geological bodies and the analysis of its genetic evolution. Therefore, we see potentials of GF-5’s thermal infrared data applied in mineral exploration.

In this paper, the ability of mineral classification and silica content estimation are analyzed using GF-5’s thermal infrared bands, to prepare GF-5 thermal infrared data for possible application in mineral information extraction.

2. STUDY AREA AND DATA

2.1 Study Area

The study area is located about 15km in the north of Liuyuan Town, which is located in the northwestern Gansu Province of China (see Figure 2). This area is in the Yujingzi and Liuyuan intracontinental rift zone, which is a polymetallic metallogenic belt that contains copper, gold, silver, iron, tungsten, molybdenum, lead and zinc (Cui et al., 2014).

2.2 Data

Since Gaofen-5 satellite has not been launched yet, emissivity image of GF-5’s TIR bands at the study area is simulated for our research, and ASTER image was used as the simulation data source. This ASTER data was acquired on September 27, 2004.

In addition, to analyze minerals’ spectral features indicated by GF-5’s TIR data, carbonate, sulfate, and silicate mineral spectra from ASU (Arizona State University) spectral library is used. Specifically, 85 spectra of minerals from ASU emissivity spectral library are selected, including 7 carbonate samples, 5 sulfate samples, and 73 silicate samples (which contains 17 feldspars, 16

* Corresponding author

amphiboles, 40 pyroxene). It is noted that carbonate, sulfate, and silicate comprise 1.7%, 0.1% and over 90% of earth crust’s quality separately.

Figure 2. The map of the study area (©2018 Bing Maps)

3. METHODOLOGY

The basic processing steps applied for mineral classification and silica content estimation using GF-5 thermal infrared data are given in Figure 3 and explained in the following subsections briefly. First, band emissivities are calculated for these minerals with spectral response functions of GF-5’s TIR bands. Then, spectral features of these minerals are analyzed based on GF-5’s TIR band emissivities; spectral indices and correlation model are established for classification and silica content estimate, respectively. Finally, these established methods are performed on GF-5’s emissivity images.

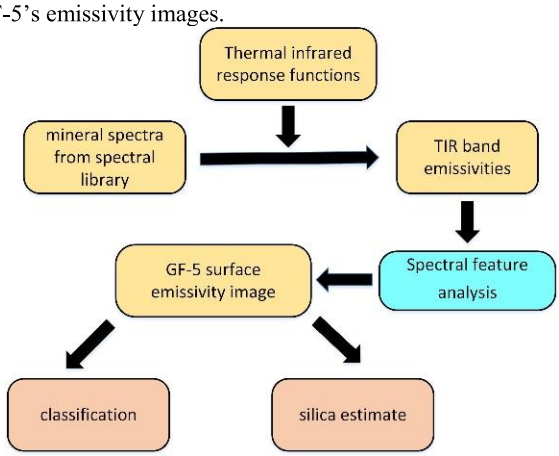

Figure 3. Flow chart used in the study.

3.1 Spectral Indices

We compared these minerals’ TIR band emissivities, which are shown in Figure 4. It can be observed that carbonate minerals have a slightly higher emissivity in band TIR1 than in band TIR2, whereas sulfate and silicate minerals show the opposite spectral signature. Also, silicate and sulfate minerals have different spectral features in band TIR2, TIR3 and TIR4. That is, sulfate minerals have relatively higher emissivity in band TIR3 than in band TIR2 and TIR4, while silicates generally show absorption in TIR3 band emissivity. To quantitatively analyze these spectral features for classification, two spectral indices are designed, and they are defined as following:

$$R1 = \varepsilon_2/\varepsilon_1 \quad (1)$$

$$R2 = (\varepsilon_2 + \varepsilon_4)/\varepsilon_2 \quad (2)$$

where ε_i = emissivity of ith TIR band

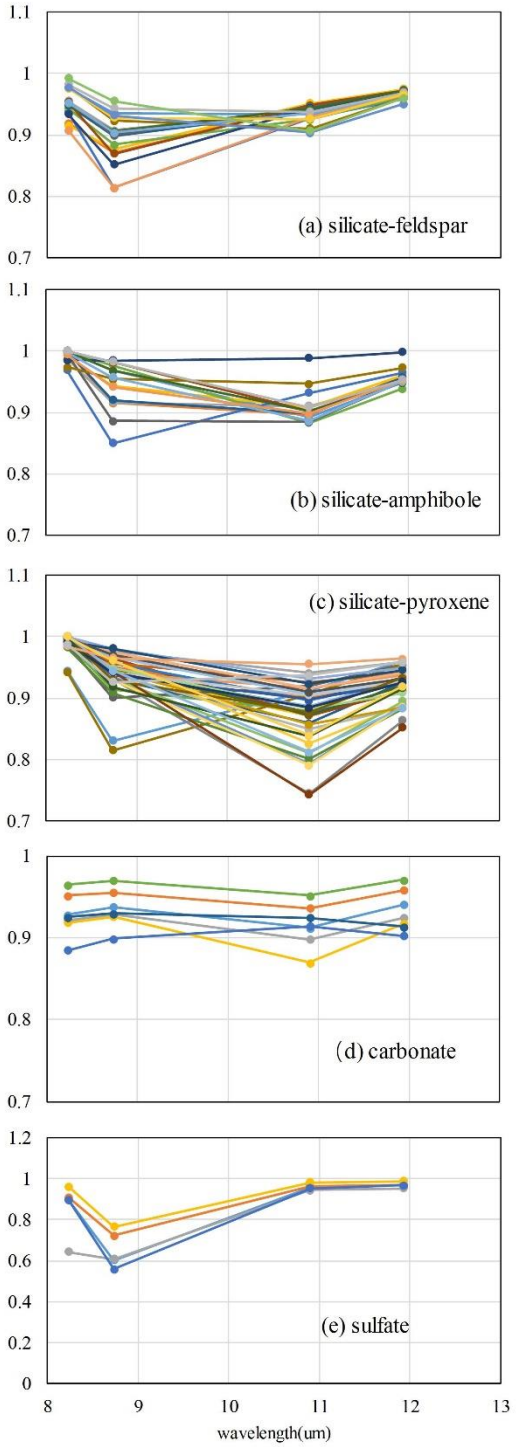

Figure 4. GF-5’s TIR band emissivities of minerals in ASU library.

R1 and R2 are calculated for 85 spectra mentioned above and their range are listed in Table 1.

Mineral Type	R1 range	R2 range
carbonate	1.003 – 1.015	-
sulfate	0.620 – 0.946	0.799 – 0.893
silicate	0.865 – 0.999	0.956 – 1.208

Table 1. Ranges of spectral indices from mineral in ASU library.

From Table 1, we can see that R1 of carbonate minerals is greater than 1, whereas sulfate and silicate minerals have an R1 of less than 1. In addition, R2 of sulfate minerals ranges from 0.799 to 0.893, and silicate minerals have a R2 of 0.956 to 1.208. Therefore, by setting threshold values of R1 and R2, carbonate, sulfate, and silicate minerals can be classified based on Gaofen-5's four thermal infrared band information as following:

- Carbonate: R1>1
- Sulfate: R1<1 and R2<0.92
- Silicate: R1<1 and R2>0.92

3.2 Correlation Analysis

Each spectrum in ASU spectral library is accompanied by physical and compositional information. Therefore, silicate minerals' spectra in ASU library and their corresponding silica content can be used to build the content estimation model. Specifically, correlation analysis is conducted between GF-5's thermal infrared band emissivity of silicate minerals or spectra index calculated by these emissivities (i.e. $\varepsilon_1/\varepsilon_2$, $\varepsilon_2/\varepsilon_3$, $\varepsilon_3/\varepsilon_4$, $(\varepsilon_1+\varepsilon_3)/2\varepsilon_2$ and $(\varepsilon_2+\varepsilon_4)/2\varepsilon_3$), and the silica content; then band emissivity or spectral index with the highest correlation is selected. Finally, through regression analysis, the model with the highest correlation coefficient (R^2) will be finally chosen for silica content inversion. Correlation models with relatively high R^2 are displayed in Figure 5 and listed in Table 2.

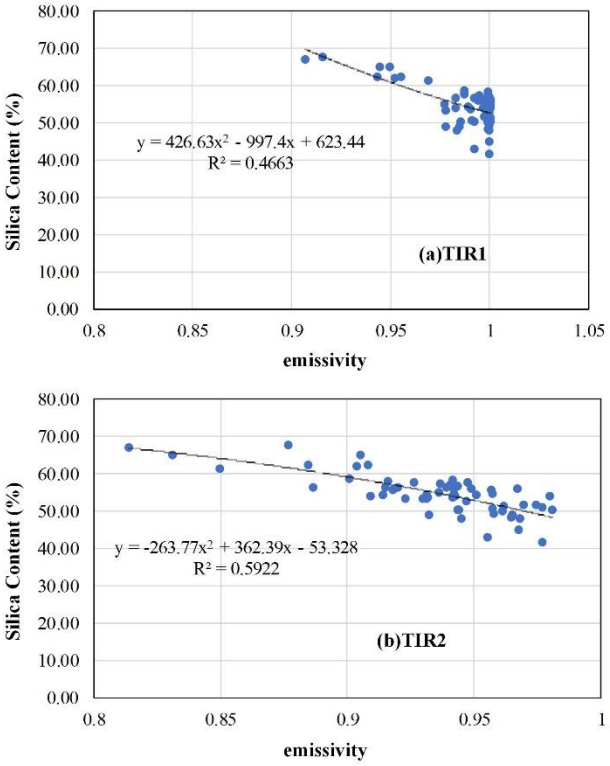

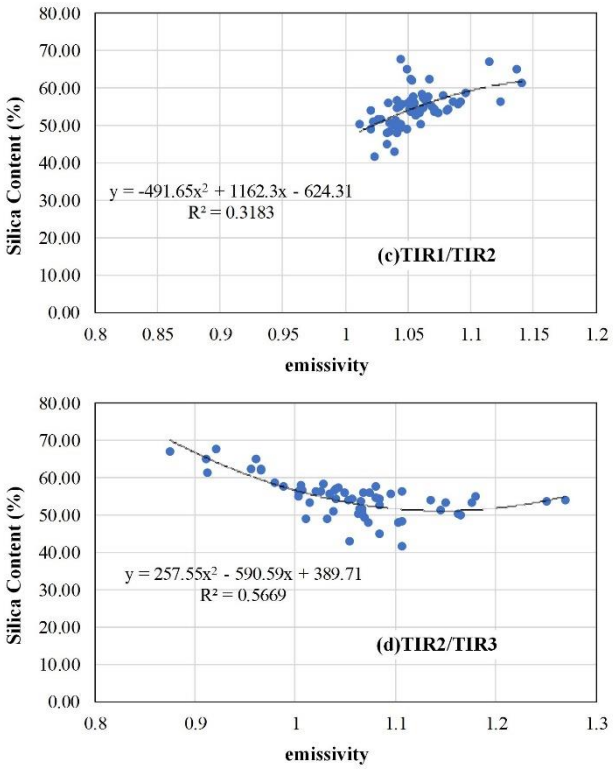

Figure 5 Correlation models established between GF-5's TIR band emissivity/spectral indices of silicate and silica content.

Emissivity/ Spectra index (x)	Correlation model (y denotes silica content)	R^2
ε_1	$y = 4.27x^2 - 9.97x + 6.23$	0.466
ε_2	$y = -2.64x^2 + 3.62x - 0.53$	0.592
$\varepsilon_1/\varepsilon_2$	$y = -4.92x^2 + 11.62x - 6.24$	0.318
$\varepsilon_2/\varepsilon_3$	$y = 2.58x^2 - 5.91x + 3.90$	0.567

Table 2 Correlation model built for silica content estimate based on GF-5's TIR band emissivity/spectral index.

4. RESULTS

4.1 Emissivity Image Generation

The classification method is tested for our study area on GF-5's TIR simulated emissivity image, which is generated based on spectral mixing of ASTER data. The simulation method is similar to one that we've given in previous work (Liu et al., 2017). The simulated image is displayed in Figure 6.

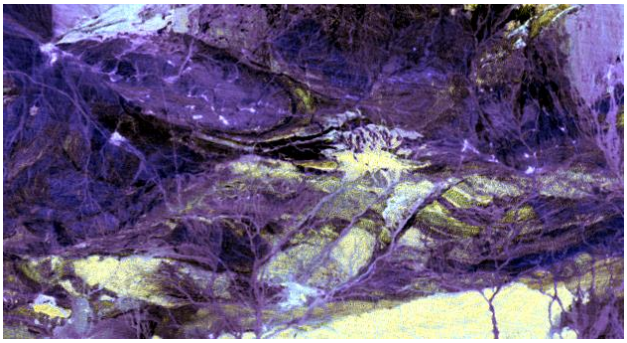

Figure 6. False color composite of simulated GF-5’s TIR band emissivity image (R-TIR1, G-TIR2, B-TIR3).

4.2 Result Analysis

Mineral classification is conducted using thresholds of spectral indices proposed in Section 3.1. According to our experimental results, only carbonate and silicate minerals have been extracted; no sulfate minerals identified in the study area. We have collected 47 samples (14 carbonate and 33 silicate samples) in Liuyuan, and used these samples to validate the mapping results, which turn out to be with 94% and 100% correct of recognizing carbonate and silicate minerals, respectively. Moreover, through ground survey with geological information analysis, sulfate minerals do not exist in the study area.

According to the method proposed in Section 3.2, the correlation between TIR2 emissivity and the silica content was found to be the highest. The corresponding model is a quadratic polynomial one that’s established based on TIR2 emissivity. However, the model’s coefficient of determination (R^2) is 0.592, which is not very high. In contrast, silica content inversion model using ASTER data is a linear model based on a spectral index (the ratio of band 12 emissivity to that of band 13), with a R^2 of 0.78. Concerning that linear model is more stable and with a higher R^2 value, it can be inferred that GF-5’s thermal infrared data is not as good as ASTER data for silica content inversion. Comparing the spectral range of GF-5 and ASTER TIR bands in Figure 1, we can see that ASTER’s band 12 and 13 are basically overlapped by GF-5’s TIR2 band, which shows that GF-5’s band settings cannot exhibit spectral features of silica contents as that in ASTER data.

5. CONCLUSIONS

In this paper, the application of Gaofen-5’s thermal infrared data is discussed for mineral information extraction, in terms of mineral classification and silica content estimate for silicate rocks. Based on mineral spectra from ASU spectral library, a classification method is proposed for carbonate, silicate and sulfate minerals, as well as the inversion model of silica content tried on correlation for silicate minerals. Since actual Gaofen-5 data is unavailable, the classification has been tested on simulated data, and accuracy analysis is conducted with ground data collected in the field. According to experimental results, using the method proposed in this paper, mineral classification can be performed using Gaofen-5’s thermal infrared data. However, the silica content inversion model is not as good as that based on ASTER thermal data, showing that emissivity of GF-5’s thermal infrared bands do not exhibit obvious spectral features associated with silica content.

REFERENCES

Ye X., Ren H., Liu R., Qin Q., Liu Y., Dong J., 2017. Land surface temperature estimate from Chinese Gaofen-5 satellite data using split-window algorithm. IEEE Transactions on Geoscience and Remote Sensing, vol. 55, no. 10, pp. 1-12.

Kanlinowski A., Oliver S., 2004. ASTER Mineral Index Processing. Remote Sensing Application Geoscience Australia. Australian Government Geoscience Website: http://www.ga.gov.au/image_cache/GA7833.pdf

Ninomiya, Y., Fu B., 2003. Extracting lithologic information from ASTER multispectral thermal infrared data in the northeastern Pamirs. Xinjiang Geology, vol. 21, no. 1, pp. 22-30.

Aboelkhair H., Ninomiya Y., Watanabe Y., Sato I., 2010. Processing and interpretation of ASTER TIR data for mapping of rare-metal-enriched albite granitoids in the central eastern desert of Egypt. Journal of African Earth Sciences, vol. 58, no. 1, pp. 141-151.

Cui J., Yan B., Wang R., Tian F., Zhao Y., Liu D., Yang S., Shen W., 2014. Regional-scale mineral mapping using ASTER VNIR/SWIR data and validation of reflectance and mineral map products using airborne hyperspectral CASI/SASI data. International Journal of Applied Earth Observation and Geoinformation, vol. 33, pp. 127-141.

Liu Y., Li N., Ren H. and Zhang T., 2017. Emissivity image simulation for thermal infrared bands on Gaofen-5 using airborne hyperspectral data, In Proc. IEEE International Geoscience and Remote Sensing Symposium (IGARSS), pp. 2093-2096.

2018 Fifth International Workshop on Earth Observation and Remote Sensing Applications

Study on White Birch Identification in Northeastern China using Hyperspectral Remote Sensing Data

Kun Shang*, Yao Liu, Chenchao Xiao
China Aero Geophysical Survey and Remote Sensing Center for Land and Resources
Beijing, China
shangkun0213@126.com

***Abstract*—The mixed forest of larch (*Xingan Larix gmelinii*) and white birch (*Betula platyphylla*) is the main forest type in Northeastern China and plays a key role in regional ecological environment. Remote sensing has become an important approach to identify and classify vegetation types. By using hyperspectral data, we could obtain more detailed vegetation information, such as tree species. This study mainly focuses on the identification algorithm of white birch based on hyperspectral remote sensing data. The results show that the proposed method can effectively detect the white birch with larch as the background vegetation. Using this method, we can quickly realize the survey of tree species in large area, which is of great significance for the study of forest landscape ecology**

Keywords*—White birch, identification, hyperspectral, remote sensing

I. Introduction

The mixed forest of larch (*Xingan Larix gmelinii*) and white birch (*Betula platyphylla*) is the main forest type in Northeastern China. It plays a key role in building green ecological barrier and maintaining national ecological security in the north area (Ercha et al., 2013). However, for a variety of reasons, this kind of forest is also faced with several problems, such as the tree species and stand structure are getting simple, resulting in more forestry disasters (Li et al., 2012). Therefore, there is an urgent need to develop an efficient identification method focused on white birch.

Traditional methods of estimating the proportion of tree species are mostly based on field investigation, which costs a lot of manpower and material resources. By using remote sensing data, the distribution of tree species in large area can be obtained quickly and timely (Saatchi et al., 2008). Nevertheless, the identification capability using traditional multi-spectral remote sensing data has its limits in some area, where both the target and the background are vegetation types. Fortunately, hyperspectral remote sensing data have more abundant spectral information with hundreds to thousands spectral bands. By using hyperspectral data, we can identify more detailed vegetation information (Buddenbaum et al., 2005; Clark et al., 2005; Matsuki et al., 2017; Wietecha et al., 2017).

Therefore, this study mainly focuses on the identification algorithm of white birch based on hyperspectral remote sensing data.

II. Data and Study Area

Genhe forest experimental area, located in Great Xingan Mountains, is chosen as the study area (121.46° --121.54° E, 50.90° --50.95° N). Xingan larch (*Xingan Larix gmelinii*) and white birch (*Betula platyphylla*) are the dominant vegetation types in this region.

Fig. 1. The image used in our study (R: 488.43nm, G: 543.72nm, B: 694.91nm).

978-1-5386-6642-5/18/$31.00 ©2018 IEEE

The hyperspectral data used in this study was obtained by AISA Eagle II hyperspectral scanner in August 28th, 2016. The spatial resolution is 1m and the spectral resolution is 3.3nm with 64 spectral bands, covering a spectral range from 400nm to 1000nm.

To remove the impacts of the atmosphere and topography on the original data, radiation calibration, geometric correction and atmospheric correction are performed. CALIGEOPRO software is used for radiation calibration and geometric correction, while ATCOR software is used for atmospheric correction.

The processing of original aerial remote sensing image could be time-consuming because hyperspectral images usually contain a large amount of spectral data. So for improving the calculation efficiency, we use a sub image of 500*750 pixels as our experimental data. Note that according to field investigations, this sub image basically covers the main surface types in the Genhe experimental area, including white birch, Xingan larch, forest swamp, bare land and road.

III. METHODOLOGY

The white birch identification process mainly includes the following steps. Firstly, considering that white birch is one of the typical broad-leaved tree species, the biological parameters in the canopy of white birch and larch has great difference. So we choose 15 kinds of vegetation indices, which are sensitive to the chlorophyll content, photochemical, structure insensitive pigment, anthocyanin and water content to distinguish white birch from Xingan larch. Then, according to the separability between larch and white birch, feature selection of the original spectrum and vegetation index is performed to reduce the data dimension. Lastly, based on the selected feature bands, four kinds of target identification algorithms are compared, including Matched filtering (MF), Target-constrained interference-minimized filter (TCIMF), Mixture tuned matched filtering (MTMF), and Mixture tuned TCIMF (MTTCIMF).

A. Feature selection

We employ the Jeffries-Matusita (J-M) Distance (Schmidt and Skidmore, 2003) to describe the separability of samples between white birch and the background types, in order to have better assessments for the capabilities of identifying white birch of different bands in the original image. J-M distance distributes between 0 and 2, good separability between samples can be expressed by a distance value larger than 1.9.

The formula of J-M distance is as follows:

$$JM_{ij} = \left\{ \int_x \left[\sqrt{p(x/W_i)} - \sqrt{p(x/W_j)} \right]^2 dx \right\}^{\frac{1}{2}}$$

where p(x/Wi) is conditional probability density, that is, the probability of the i^{th} pixel belongs to the W_i class.

The differences in spectra between white birch and other background types are extracted when analyzing the spectral features of white birch, and the separability between white birch and other types in the original spectral space is computed.

Meanwhile, we calculate several vegetation indices that are sensitive to the contents of chlorophyll, photochemical, structure insensitive pigment, anthocyanin and water in canopy, as well as the separabilities in the feature space of the individual vegetation indices.

TABLE I. VEGETATION INDICES

NO.	ABBR.	FULL NAME
1	NDVI	Normalized Difference Vegetation Index
2	SRI	Simple Ratio Index
3	EVI	Enhanced Vegetation Index
4	ARVI	Atmospherically Resistant Vegetation Index
5	RENDVI	Red Edge Normalized Difference Vegetation Index
6	MRESRI	Modified Red Edge Simple Ratio Index
7	MRENDVI	Modified Red Edge Normalized Difference Vegetation Index
8	SGI	Sum Green Index
9	VREI1	Vogelmann Red Edge Index 1
10	PRI	Photochemical Reflectance Index
11	SIPI	Structure Insensitive Pigment Index
12	RGRI	Red Green Ratio Index
13	ARI1	Anthocyanin Reflectance Index 1
14	ARI2	Anthocyanin Reflectance Index 2
15	WBI	Water Band Index

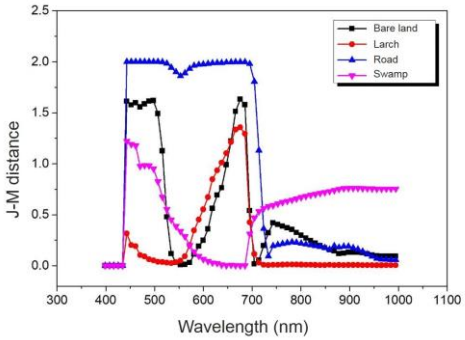

Fig. 2. Separability of samples between white birch and background types in different original bands (J-M distance).

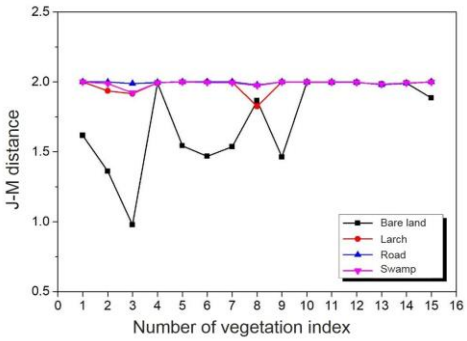

Fig. 3. Separability of samples between white birch and background types in different vegetation indices (J-M distance).

978-1-5386-6642-5/18/$31.00 ©2018 IEEE

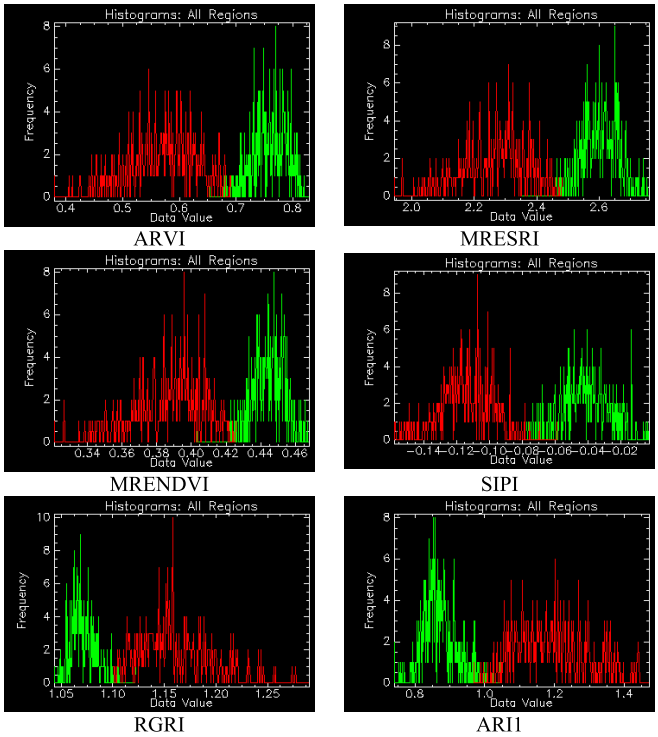

Fig. 4. Histograms of white birch (red) and Xingan larch (green) under different vegetation indices.

At last, the most useful spectral features that are sensitive to white birch in the combining spectral space of both original bands and proposed vegetation indices are selected, and the feature spaces for identifying white birch are accordingly established.

The finally used feature spaces contain: six original bands within the spectral region of 443.1 to 497.58 nm, six original bands within 647.19 to 685.34 nm, and some vegetation indices including ARVI, SIPI, RGRI, ARI1, MRESRI and MRENDVI.

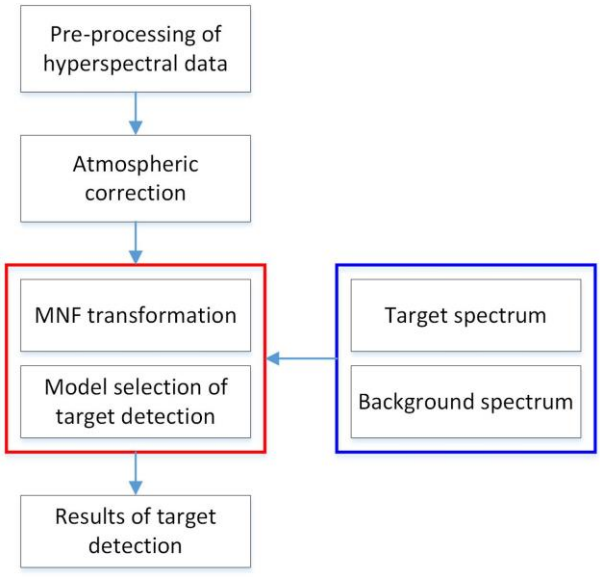

Fig. 5. Flow scheme for detection of white birch based on hyperspectral data.

B. *Target detection methodology*

Figure 5 shows the processing flow for detecting white birch using the selected features. During the process, four widely used target detection methods are analyzed and compared: Matched filtering (MF), Target-constrained interference-minimized filter (TCIMF), Mixture tuned matched filtering (MTMF), and Mixture tuned TCIMF (MTTCIMF).

We select 314 white birch samples through comprehensive interpretation and filter survey verification, and use 100 of them to be training samples, and the rest as test samples for assessing the detection accuracies.

IV. Results

The accuracies of difference identification methods are listed in Table II. By comparing the detection results based on the four methods between the original and feature bands, we can see that dimensionality reduction for the original spectral space not only increases the calculation efficiency but also maintains high accuracies for all methods. In particular, the accuracies for MTTCIMF and MTMF method are even much higher when transferred to feature bands (i.e., increase by about 2.8%). And for feature bands, all methods can yield highly accurate results (accuracies over 98%).

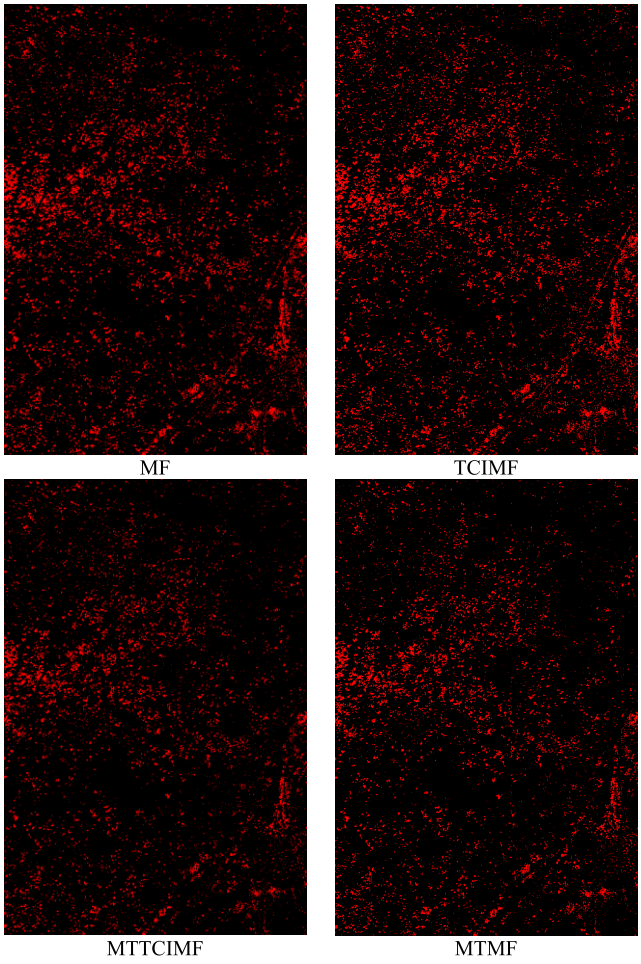

Fig. 6. Identification results of white birch using original spectral bands.

978-1-5386-6642-5/18/$31.00 ©2018 IEEE

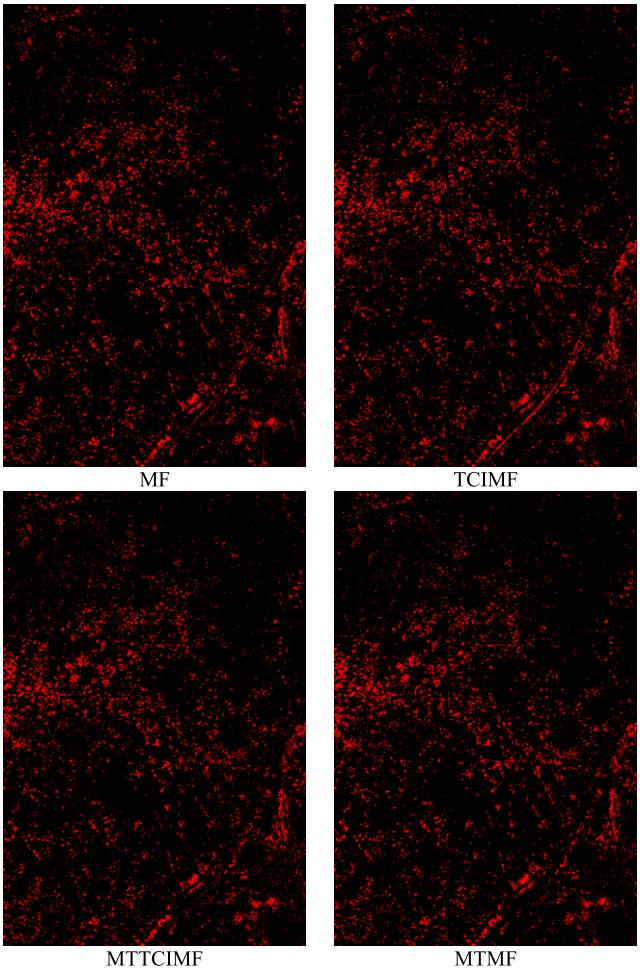

Fig. 7. Identification results of white birch using selected feature bands.

TABLE II. IDENTIFICATION ACCURACY OF WHITE BIRCH

METHOD	ORIGINAL BANDS	FEATURE BANDS
MF	98.5981%	**99.0654%**
TCIMF	98.1308%	98.5981%
MTTCIMF	95.7944%	98.5981%
MTMF	96.2617%	**99.0654%**

In addition, it is worth noting that the MTTCIMF and MTMF methods do not need adjusting parameters artificially, so one important advantage for them is the detection results are usually less disturbed by man-made operations.

V. CONCLUSIONS

This study proposes a white birch identification method based on vegetation indices using hyperspectral remote sensing data, and takes Genhe forest experimental area as the study area to perform the data experiment. The identification method makes full use of the abundant spectral information of hyperspectral data, and takes the biological parameters' difference, such as chlorophyll content, photochemical and anthocyanin, between the target and background vegetation types into consideration. The results show that the proposed method can effectively detect the white birch with larch as the background vegetation. Using this method, we can quickly realize the survey of tree species in large area, which is of great significance for the study of forest landscape ecology.

ACKNOWLEDGMENT

This work was supported by the Chinese Major Project of High Resolution Earth Observation System under Grant 30-Y20A30-9003-15/17 and 04-Y20A36-9001-15/17. And this data set is provided by 2016 Remote sensing Experiment supported by the National Basic Research Program of China (973 Program) "Dynamic analysis and modeling of remote sensing information for complex land surface (2013CB733400)".

REFERENCES

[1] Ercha H U, Wang X, Zhang W, et al. Age structure and point pattern of Butula platyphylla in Wulashan Natural Reserve of Inner Mongolia[J]. Acta Ecologica Sinica, 2013, 33(9):2867-2876.

[2] H. Buddenbaum, M. Schlerf, J. Hill. Classification of coniferous tree species and age classes using hyperspectral data and geostatistical methods[J]. International Journal of Remote Sensing, 2005, 26(24):5453-5465.

[3] Li Jing, Luo Youqing, Shi J. The optimum mixture ratio of larch and birch in terms of biodiversity conservation: A case study in Aershan forest area[J]. Acta Ecologica Sinica, 2012, 32(16):4943-4949.

[4] Schmidt K S, Skidmore A K. Spectral discrimination of vegetation types in a coastal wetland[J]. Remote Sensing of Environment, 2003, 85(1):92-108.

[5] Saatchi S, Buermann W, Steege H T, et al. Modeling distribution of Amazonian tree species and diversity using remote sensing measurements[J]. Remote Sensing of Environment, 2008, 112(5):2000-2017.

[6] Clark M L, Roberts D A, Clark D B. Hyperspectral discrimination of tropical rain forest tree species at leaf to crown scales[J]. Remote Sensing of Environment, 2005, 96(3):375-398.

[7] Matsuki T, Yokoya N, Iwasaki A. Hyperspectral Tree Species Classification of Japanese Complex Mixed Forest With the Aid of Lidar Data[J]. IEEE Journal of Selected Topics in Applied Earth Observations & Remote Sensing, 2017, 8(5):2177-2187.

[8] Wietecha M, Modzelewska A, Stereńczak K. Airborne hyperspectral data for the classification of tree species a temperate forests[J]. Sylwan, 2017, 161(1):3-17.

978-1-5386-6642-5/18/$31.00 ©2018 IEEE

A Simple Shadow Area Processing Method

Haiqing Wang
China Aero Geophysical Survey and Remote Sensing Center for Land and Resources,Beijing 100083,China.
Email: whq0705@126.com

Keywords: Remote sensing, shadow area, ratio analysis, image processing

Abstract: Shadow is an important factor that restricts remote sensing information extraction. How to use simple and effective image processing method to display the remote sensing information of shadow area has been a difficult problem in the field of remote sensing. In this paper, a simple ratio analysis method is applied to study the shadow area remote sensing image processing, which shows the remote sensing information hidden in the shadow area better. The method lays a good foundation for further remote sensing information extraction. This method is simple and effective, not only can solve the problem, but also easy to operate, even the non-remote sensing image processing professionals can also be used flexibly.

1 INTRODUCTION

Shadow is an important factor that restricts remote sensing information extraction. How to use simple and effective image processing method to display the remote sensing information of shadow area has been a difficult problem in the field of remote sensing. There are many research findings about shadow processing, in recent years. A shadow processing method based on normalized RGB colour model was proposed by Yang and Zhao (Yang and Zhao, 2007).A shadow compensation method based on linear stretching, smoothing and principal component was proposed by Wang and Wang (Wang and Wang, 2010). By improving the Wallis filtering shadow compensation strategy, the ground information in the shadow area was highlighted by Gao et al. (Gao et al., 2012). The shadow vegetation index SVI was constructed to discuss the problem of image shadow removal by Xu et al. (Xu et al., 2013).Combining the wave band regression model and shadow vegetation index SVI can be effective, according to Liu et al. (Liu et al., 2013). Gao et al. (Gao et al., 2014) believe that in order to compensate the model as the foundation, through the mean brightness shadow and non-shadow region statistics and variance, it is possible to use the method of feature extraction and matching of automatic acquisition of model parameters, automatic compensation and shadow comprehensive regional overall level of compensation and compensation for the two level local window. Deng et al. (Deng et al., 2015) explored the use of blue light suppression algorithm and statistical information of shadow homogeneity to compensate for H, I and S components, respectively and converted the results to RGB colour space to achieve shadow compensation. Based on ArcGIS Engine platform, Matlab and GDAL development tools, Yang et al. (Yang et al., 2015) integrated shadow detection and compensation systems designed according to the shadow detection and compensation algorithm of high resolution remote sensing images. Shadow removal of remote sensing images based on inhomogeneous regularized texture-preserving was proposed by Fang et al. (Fang et al., 2015). The shadow removal model of traditional HSV space by integrating one step information, based on it, a shadow removal algorithm of moving objects based on reflectance ratio invariants, was proposed by Zhang and Yang (Zhang and Yang, 2016). Improvement of image shadow tracking and elimination algorithm based on texture loss least constraint was proposed by Yan et al. (Yan et al., 2016). Methods of pattern recognition and image enhancement are used to discuss the problem of shadow removal by Zhao et al. (Zhao et al., 2016). Methods used shadow extraction, envelope removal, similar pixel search and shadow brightness reconstruction to explore the shadow

Wang, H.
A Simple Shadow Area Processing Method.
In *Proceedings of International Workshop on Environment and Geoscience (IWEG 2018)*, pages 507-510
ISBN: Not Available

information reconstruction experiment of Landsat 8 OLI image in hilly area of southwest China were proposed by Zhang et al. (Zhang et al., 2017). Shadow removal algorithm based on improved Gaussian mixture model and texture was proposed by Wang and Zhang (Wang and Zhang., 2017). A method of target detection and shadow removal based on the combination of improved adaptive hybrid Gaussian model and colour space was proposed by Wang and Tong (Wang and Tong, 2013). These shadow removal methods are more suitable for remote sensing researchers, and master software professionals, however for remote sensing interpretation and information extraction of personnel engaged in the application of remote sensing, these software are often not good, and need a lot of energy to carry on the software programming, it is also difficult to extract remote sensing information of a shadow area. If a simple, effective, easy to understand and easy to operate shadow area processing method could be found; it will solve the problem of remote sensing shadow for interpreters and information extraction personnel.

2 AN OVERVIEW OF THE STUDY AREA

The study area is located in the middle of Qinghai Province, in the southeastern side of the Qaidam Basin. It is a part of Kunlun mountain, Burhan Budai Mountains in China, the highest peak of which is 5000 meters above sea level. The study area is located at an elevation of 4000 meters. Under the action of plate movement, the ground surface continues to uplift, the erosion is sharp and the terrain is rugged where it is located at the southern margin barrier of the Qaidam Basin. The remote sensing image of the mountain slope often has shadow, causing a lot of trouble to the remote sensing information extraction and interpretation work, need a simple and effective treatment method of shadow zone.

3 REMOTE SENSING DATA AND PRE-PROCESSING

In order to improve remote sensing image of shadow area, the GeoEye-1 and Worldview-2 remote sensing data of the study area were obtained (Table 1).

In order to ensure that the research work will be carried out smoothly, first of all remote sensing data quality was checked for the vegetation cover, the amount of snow and ice, cloud cover, distortion, and noise. Inspection shows that the remote sensing data is characterized by rare cloud and snow, low vegetation cover, no distortion, no noise (Table 2).

Table 1: List of remote sensing data and their characteristics.

Number	Data Type	Band Name	Band Number	Resolution(m)	Spectral Range(nm)
1	GeoEye-1	Pan	Pan	0.5	450-800
		Blue	1	2	450-510
		Green	2	2	510-580
		Red	3	2	655-690
		Near Infrared	4	2	780-920
2	Worldview-2	Pan	Pan	0.5	450-800
		Coastal	1	2	400-450
		Blue	2	2	450-510
		Green	3	2	510-580
		Yellow	4	2	585-625
		Red	5	2	630-690
		Red Edge	6	2	705-745
		Near Infrared 1	7	2	770-895
		Near Infrared 2	8	2	860-1040

Table 2: List of remote sensing data inspection

Number	Data Type	Vegetation	Snow and Ice	Cloud	Distortion	Noise	Strip
1	GeoEye-1	Very Sparse	No	<5%	Not Obvious	No	No
2	Worldview-2	Very Sparse	<5%	<5%	Not Obvious	No	No

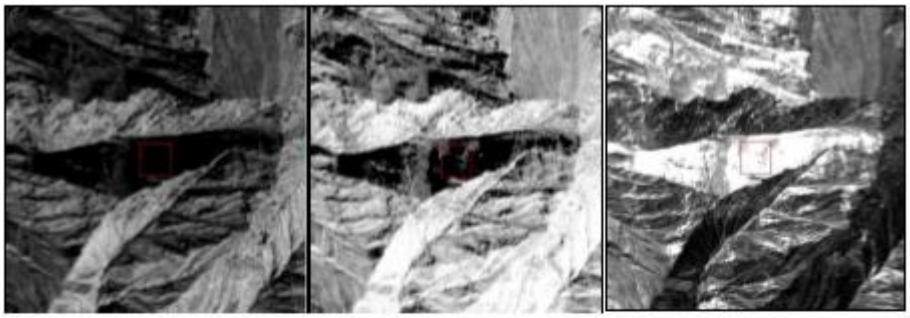

Figure 1: Image contrast of GeoEye-1 before and after data ratio operation (Left: B1; Middle: B3; Right: B1/B3).

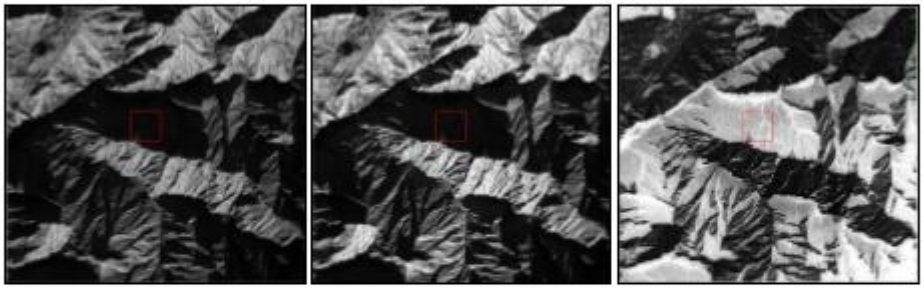

Figure 2: Image contrast of Worldview-2 before and after data ratio operation (Left: B3; Middle: B8; Right: B3/B8).

Remote sensing data pre-treatment includes raw data normalization, image rectification, band registration, image mosaic, data fusion, removal of interference and tailoring of black edges. The processed remote sensing data are more suitable for subsequent research.

4 IMAGE PROCESSING IN SHADOW AREA

In order to display remote sensing information hidden in the shadow area, a variety of remote sensing image processing methods had been tried, and it was found that the method of using band ratio operation is simple and effective.

Using GeoEye-1 remote sensing data to conduct shadow area remote sensing image processing method, it was found that after executing B1/B3 band ratio operation, the hidden information in the shadow area can be displayed, which is convenient for remote sensing interpretation (Figure 1).

Using Worldview-2 remote sensing data to conduct shadow area remote sensing image processing method, it is found that after B3/B8 band ratio operation, the hidden information in the shadow area can be displayed, which is convenient for remote sensing interpretation (Figure 2).

5 CONCLUSIONS

It is concluded that by using GeoEye-1 and Worldview-2 remote sensing data, B1 to B3 and B3 to B8 band ratios respectively can make the hidden information in the shadow area appear, which makes the interpretation of the remote sensing images easier.

This method is simple and effective, not only to solve the shadow problem, but also easy to operate, even for the non-remote sensing image processing professionals.

ACKNOWLEDGMENTS

China Geological Survey Project: national mineral resources development environment remote sensing monitoring (DD20160075, 121201003000172705), national mine new restoration and treatment monitoring in 2017 (DD20189805, 121201003000172718) support.

REFERENCES

Deng L, Deng M J and Zhang L S 2015 Optimization of shadow detection and compensation method for high-resolution remote sensing images *J Remote Sensing Technology and Application* **30**(2) 277-284

Fang Y M, Li B L and Wu Y J 2015 Shadow removal of remote sensing images based on inhomogeneous regularized texture-preserving *J Journal of Computer Applications* **35**(S2) 238-241

Gao X J, Wan Y C and Yang Y W 2014 Automatic shadow detection and automatic compensation in high resolution remote sensing images *J Acta Automatica Sinica* **40**(8) 1709-1720

Gao X J, Wan Y C and Zheng S Y 2012 Automatic shadow detection and compensation of aerial remote sensing image *J Geomatics and Information Science of Wuhan University* **37**(11) 1299-1302

Liu J, Xu Z H and Yu K Y 2013 Shadow detection and removal method for remote sensing image in mountainous and hilly area *J Transactions of the Chinese Society for Agricultural Machinery* **44**(10) 238-241, 237

Wang H R and Tong W 2017 Target detection and shadow removal method based on the improved gaussian model *J Journal of Jiangsu University of Science and Technology (Natural Science Edition)* **31**(2) 172-177

Wang Y and Wang S G 2010 Detection and compensation of shadows in high resolution remote sensing images using PCA *J. Journal of Applied Sciences* **28**(2) 136-141

Wang Y N and Zhang H 2017 Shadow removal algorithm based on improved gaussian mixture model and texture *J Computer Engineering and Design* **38**(7) 1879-1884

Xu Z H, Liu J and Yu K Y 2013 Construction of vegetation shadow index (SVI) and application effects in four remote sensing image *J Spectroscopy and Spectral Analysis* **33**(12) 3359-3365

Yan F, Zhang J and Wu S D 2016 Improvement of image shadow tracking and elimination algorithm based on texture loss least constraint *J Modern Electronics Technique* 39(27) 104-108

Yang J and Zhao Z M 2007 Shadow processing method based on normalized RGB color model *J. Opto-Electronic Engineering* **34**(12) 92-96

Yang X W, Yang S W and Zhang L M 2015 Design and development of the shadow detection and compensation system for high-resolution remote sensing images *J Remote Sensing for Land and Resources* **27**(3) 177-181

Zhang P and Yang Y X 2016 Multiple information fusion of video moving target shadow removal algorithm *J Video Engineering* **40**(2) 59-64

Zhang T, Liao H P and Cui L L 2017 Mountainous shadow information restoration based on the continuum removed *J Journal of Remote Sensing* **21**(4) 604-613

Zhao Y F, Ren H E and Hu J F 2016 Genetic algorithm and homomorphic filter for log face image process *J Journal of Northeast Forestry University* **44**(8) 92-96

TYPICAL APPLICATIONS OF AIRBORNE LIDAR TECHNOLAGY IN GEOLOGICAL INVESTIGATION

Xiongwei Zheng , Chunlei Xiao*
China Aero Geophysical Survey& Remote Sensing Center for Land and Resources, Beijing100083, China-
(12260746,45561247)@qq.com

Commission III, WG III/5

KEY WORDS: airborne light detection and ranging (LiDAR); surface subsidence; landslide; fault

ABSTRACT:

The technology of airborne light detection and ranging (LiDAR), also referred to as Airborne Laser Scanning, is widely used for high-resolution topographic data acquisition (even under forest cover) with sub-meter planimetric and vertical accuracy. This contribution constructs the real digital terrain model to provide the direct observation data for the landscape analysis in geological domains. Based on the advantage of LiDAR, the authors mainly deal with the applications of LiDAR data to such fields as surface land collapse, landslide and fault structure extraction. The review conclusion shows that airborne LiDAR technology is becoming an indispensable tool for above mentioned issues, especially in the local and large scale investigations of micro-topography. The technology not only can identify the surface collapse, landslide boundary and subtle faulted landform, but also be able to extract the filling parameters of collapsed surface, the geomorphic parameters of landslide stability evaluation and cracks. This technology has extensive prospect of applications in geological investigation.

1. INTRODUCTION

Airborne light detection and ranging (LiDAR) system is a multi-sensor system comprising three major time-synchronized components: a laser scanner unit, a Global Navigation Satellite System (GNSS) and Inertial Measurement Unit (IMU). Based on the laser pulse time-of-flight distance measurement, all three components together enable the direct derivation of the absolute position (X, Y, Z) of each record reflection on the earth. Therefore, the system is widely used for high-resolution topographic data acquisition.

The technology of LiDAR with its direct determination of elevation is capable to retrieve terrain (i.e. Bare Earth) point measurements even under forest cover, allowing the generation of Digital Terrain Models (DTMs) with a high degree of automation, which has revolutionized the acquisition of elevation data by providing a tool for rapid, highly accurate and cost-effective data acquisition, relevant for regional and local geological applications: Features such as tectonic structures even if covered by vegetation could be evident by small local elevation changes in the range of decimeters (Cunningham, 2006; Arrow Smith, 2009), these minor changes in elevation can still be observed as the high vertical accuracy of LiDAR is not lost by rasterization; Several studies use LiDAR DTM to derive topographic signatures for characterizing land-slides (Mc Kean, J., 2004; Glenn, N. F., 2006) or automated mapping of landslides (Booth, A. M., 2009) even in forested areas (Van Den Eeckhaut, 2012) in order to create or update inventories; Similar studies have continued to improve the state-of-the-art in automated mapping of landslides (Tarolli, 2012; Berti, 2013), extraction of channel networks, identification of biotic signatures in landscape morphology (Roering et al., 2010), classification of marine terraces (Bowles and Cowgill, 2012), and characterization of alluvial fan surfaces (Staley, 2006; Volker, 2007); Besides object detection and mapping airborne LiDAR data are an essential input in various process simulation models in order to be able to predict or simulate scenarios of future events and risk estimation of hazards such as floods modeling processes (Cobby, 2003; Rufin Soler, 2008), debris flows (Wichmann, V., 2008; Conway, 2010), rockfall (Deparis , J., 2008; Lan, H. X., 2010) and avalanches (Schmidt , 2005; McColliste, 2009).

This paper presents studies in the geological investigation fields such as surface land collapse, landslide and fault structure extraction, using LiDAR data acquired by Leica ALS50-II airborne laser system and its standard products -DEM, to assess the ability of LiDAR technology on geological objects detection and interpretation.

2. LIDAR DATA ANALYSIS

Airborne LiDAR system sends out laser pulses that get back-scattered by various objects (ground surface, vegetation, constructions etc.) and record the feedback signal. Objects in different elevations may be illuminated by the cone of light causing more than one echo that can be recorded by the sensor's receiver, usually displayed in the form of discrete point cloud.

The analysis of LiDAR data products starting with the 3D point cloud, possibly with full-wave-form attributes, can be grouped into (i) a direct use of data and information derived from LiDAR such as digital elevation model (DEM) and (ii) an indirect application of further refined data such as roughness parameters of land cover maps and hillshade maps etc. Basically, the direct input extracts information from the LiDAR observation (i.e. elevation and radiometric data), whereas the indirect integration is based on a prior abstraction and processing (e.g. classification and object detection).

A first step in Geological landform interpretation is the LiDAR data visualization. For example, 3D perspective views or DEM color-coded by height. Slicing or drawing profiles of the data helps to get a better impression of the surface such as in complex situations with mixed surface and object types. Deeper understanding is gained by visualizing derivatives such as slope, aspect and surface curvature or to colored drape information

from optical sensors over the elevation data. Care has to be taken when adding ancillary data not acquired simultaneously in order to avoid misinterpretation caused by temporal differences in both datasets. Also differences in registration, accuracy, and resolution have to be taken into account if combining different data sets.

For applications in Geological landform analysis the separation of terrain echoes (i.e. bare Earth) and echoes on objects such as buildings and vegetation - called filtering - is of major importance. Various methods and approaches are published either working directly on the point cloud or on rasterized Digital Surface Model (DSM). An introduction to filtering and an overview of the most prominent approaches can be found in Pfeifer (Pfeifer, 2008). An overview of processing methods, analysis, and comparison of widely distributed software products and applications of digital elevation models is given by Hengl (Heng, 2009). Elevation model representing the geomorphological relevant surface can be characterized by landform classification providing input for applications in geological investigation. DTM is the basis for landform characterization and delineation. Landforms vary in their appearance which depends on the representation scale, makes the boundary definitions of regions vague and difficult to delineate. This turns landform classification into an ambiguous multi-resolution problem. In order to reach high automation for classification, object-based approaches are used frequently. They either work directly in the point cloud (object-based point cloud analysis - OBPA, Rut zinger, 2008) or in the derived rasterized models and images (object-based image analysis - OBIA, Blaschke, 2010). These approaches can be combined or iteratively applied where first the input data is segmented into homogeneous areas to define patches of points or pixels, which represent a part of an object. Features describing segments can be either related to the statistical distribution of the point or pixel values and their geometrical and topological characteristics such as segment shape, size, and neighborhood relations. Originally coming from the field of land cover classification OBIA is also used for DTM extraction and geomorphological object classification.

3. APPLICATIONS

3.1 Surface Land Collapse Survey

The subsidence is one form of coal mine secondary geological calamity, it will make the environment worsening and endanger people's life and safety. Therefore, recognizing the actual range of surface subsidence includes important research and practical significance. The precise measurement of the collapse, fill volume, area and other data for the mine geological environment problems provide decision-making basis for engineering renovation. In this paper, coal dam region in Hunan province was taken as an example to ground collapse analysis using airborne LiDAR, in order to study the surface subsidence(under vegetation cover)information recognition and extraction.

In the study area, there are complex geological environment in mines, dense vegetation, scarp, housing and other complex features. What’s more, as a result of hydrothermal condition is enough, and less human disturbance after the collapse, in the region, surface subsidence covered by dense vegetation. Shown in figure 1 (a) for optical image of the mining subsidence area (red of the location of the elliptical instructions to collapse). The figure shows that, due to the optical sensors can't penetrate the vegetation, hence collapse information can't be accessed from the optical remote sensing image. After field investigation, it can found that the fieldwork method is difficult to carry out in test zone, due to steep terrain and dense vegetation cover (shown in figure 1 (a)). A prominent advantage of airborne LiDAR compared to photogrammetry is the ability to derive to penetrate vegetation by "seeing" through small gaps in the canopy, make it possible to derive accurate DTM even in densely forested areas, providing a very detailed terrain description. Therefore, based on the DEM constructed by discrete ground point from LiDAR, the boundaries of the earth's surface subsidence area and not collapse can be interpreted clearly (as shown in figure 1 (b) of the red line), so as to identify the collapse range effectively, and through further GIS spatial analysis to obtain the parameters such as geometric center of the surface subsidence pit coordinates (projected coordinate system), area and perimeter (table 1).

(a) image

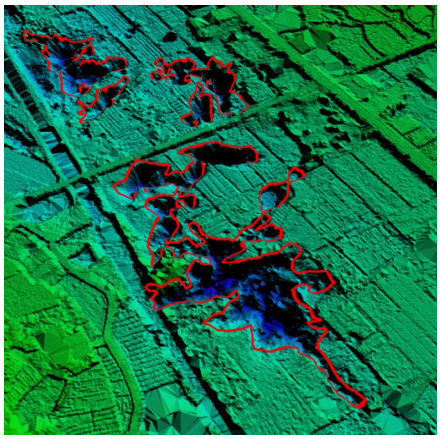

(b) DEM obtained by airborne LiDAR (the red line for the surface subsidence area and not collapse)

Figure 1.Subsidence area of coal dam covered with dense vegetation

collapse pit	
attribute name	attribute value
perimeter / km	1.345
area / km^2	0.007 55
center _X/ m	638 082.990
center _Y/ m	318 848.871
center _Z/ m	44.15

Table 1. Geometry information of subsidence pits

The advantage of surface subsidence investigation using airborne laser scanning system is that the obtained high-precision DEM , which is quicker and more accurate calculation sinkhole fill area and volume, provide important parameters for

surface subsidence to implement project management. However, field geological investigation and measurement, are regularly difficult to accurate measure the subsidence pits fill area and volume parameters. In this paper， Triangular prism method is carried out to calculate the fill volume of surface subsidence, the basic principle is: ① laser discrete point cloud on the ground constructed the irregular triangle net (TIN, figure 2 (left)), forming the three prism set about the calculation of earthwork terrain; ② filtering out surface subsidence (pit) ground point, and then, using reserving ground points determined a zero plane (right) (figure 2)by surface fitting. ③ Finally, the superposition of two TIN structure obtained by the 2 on the surface of the corresponding volume of the irregular triangular structural unit clamp is the result of fill volume (table 2).

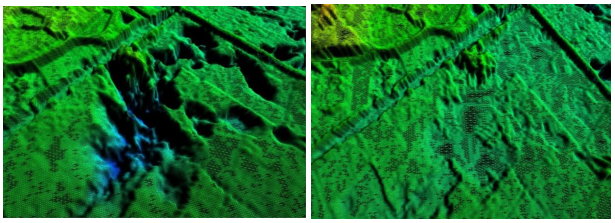

Fig.2 TIN constructed by ground data (left) and surface fitting(right)

3.2 Landslides Detection And Characterization

Airborne LiDAR permits an improvement in the landslides detection and characterization by creating accurate and precise high-resolution digital elevation model(HRDEM) in raster grids or TIN, which are 2.5D representations of the topography, or in true 3D point cloud with a high density. Taking Zhangjiawan landslides in three gorges region of China as an example, the method of landslide identification bases on HRDEM from LiDAR system is analyzed in this article.

The primary technique has been widely applied to detect and map landslides by optical remote sensing, makes use of image color difference or light shadow to identify terrain elevation mutations (such as slope sag, scratches, etc.). Although the resolution of image (figure 3) can achieve sub meter level, limited to a single light direction, it is difficult to identify the geomorphic features of landslide such as gully and boundary etc. in detail. For airborne LiDAR technology, the obtained bare earth point cloud data has the advantage to construct digital elevation model, which could depict the real topography, concluded micro morphological characteristics. And then, the hillshade can be derived through different azimuth settings based on DEM, with different illumination angle oblique hill shading set up by different azimuth to strengthen the micro morphological characteristics and terrain landform features, which facilitate to identify the boundary of landslide group.

Figure 4 shows that simulating different azimuth (90°, 135° and 180°), a series of hillshade images about Zhangjiawan landslides derived from DEM. Obviously, compared with optical image, hillshade maps based on LiDAR data can more clearly reflect the stereo configuration of landslides topography. Moreover, there are obvious differences in landslides local features expressed by shade relief images from different azimuth: Compared with the shade relief image under the illumination Angle 135°, these illumination Angle is 90° and 180° hillshade maps can more clearly reflect the linear features such as gully; The hillshade maps under azimuth angle 90° and 180°, reflected different focus of the morphological characteristics, are able to complement each other. According to geomorphic features expressed by the hillshade maps under different azimuth angle, the boundary of Zhangjiawan landslides were delineated as shown in figure 5 (the red lines marking out the border of the landslide group), the landslide is composed of six secondary landslide.

Fig.3 Ortho-photo of Zhangjiawan landslides

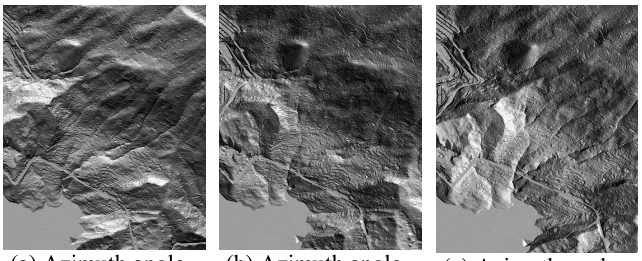

(a) Azimuth angle 90° (b) Azimuth angle 135° (c) Azimuth angle 180°

Fig.4 Hillshade maps of Zhangjiawan landslide

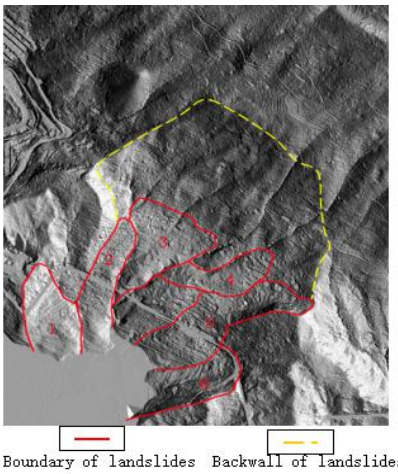

Fig.5 Boundary and back scarp of Zhangjiawan landslides(Azimuth angle 180°)

3.3 Fault detection

ALS - derived DEM gives an accurate topography and permits to identify morphologies have significations in order to characterize the past fault activity. Study area located in Beiya mine lot in Yunnan province of China was selected to carry out the test on fault detection using LiDAR data. These data are

very reliable with respect to height accuracy (root mean square error: 0.2 m) and spot density (average density of laser spot: 2 pts/m^2).

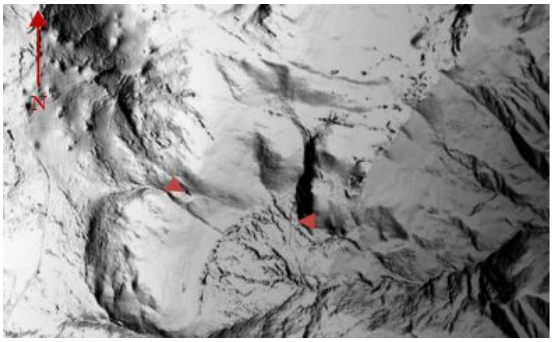

(a) Dimensional display by LiDAR data

(b) Display by optical image

Fig.8 Display of micro-features of faults（Characteristic between the red arrow is fault broken terrain）

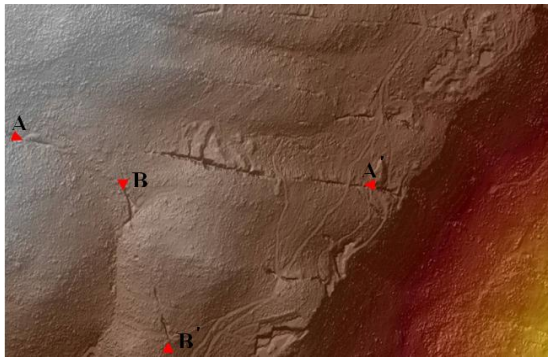

(a) Hillshade

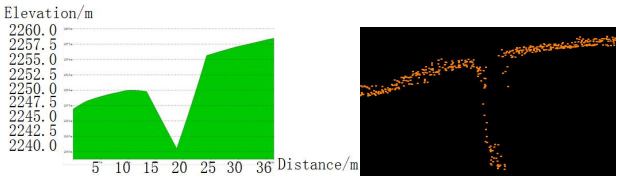

(b) DEM cross-section drawn (c)Discrete points cross-section drawn

Fig.9 Identification and micro-feature information of fissures

For early geomorphologists, field observations were central to investigate the fault fracture and local surface active fault zones in the scale of meters and centimeters, combined with surveying difficulties (poor line of sight and limited GPS coverage). LiDAR data can be depicted micro-topography meticulously, the derived hillshade can identify the location of the crack orientation towards nearly EW (AA) and NNW (BB) (figure 9 (a)). The LiDAR data is a form of discrete 3 d point clouds (figure 9c), makes a different with optics image connected relationship between pixels. Moreover, based on the LiDAR data profile information (figure 9 (b), (c)), the surface cracks information such as depth, length and geometric patterns can be determined, to provide the foundational data for fault detection quantitative analysis with different echoes.

Utilizing the filtering discrete ground points to constructed DEM of truly landscape, which has the high spatial resolution (0.5m). This resolution reaches the scale demand for broken landscape identification. The shade relief derived from LiDAR DEM can realize true three-dimensional expression of the terrain bump tiny differences, succeeded to detect the surface fissuring and the displacement of fault as Fig.8(a) shown. However, compared with traditional optical remote sensing means the study found that it is difficult to identify the subtle fault broken terrain recognized from LiDAR data in optical image (figure 8 b).

4. CONCLUSIONS

The airborne LiDAR (Light Detection and Ranging) technology can directly measure the elevation of the bare ground surface, construct Digital Elevation Model of true landscape, which could provide the foundational data for geological investigations. This paper demonstrates the applications in geological investigation such as surface land collapse, landslide and fault structure extraction for studying Earth surface landforms and points out the large potential of applications using LiDAR data for micro morphology of geological survey. LiDAR datasets are used in different processing levels, ranging from the original point clouds to the DEM, and also in different depths of integration into applications, starting with LiDAR derivatives (e.g. shaded relief map) assisting visual interpretation: Airborne LiDAR technology see through the vegetation on elevation to get the real 3D digital surface model (DEM), which is a reliable observation data to reveal the structure of the surface micro topography, which can recognize the surface subsidence under vegetation cover effectively, and extract quantitative elements such as filling area and volume of the surface subsidence, these elements can provide scientific basis for the comparative analysis about collapse development and engineering renovation in the complex landform area; The shaded relief map (hillshade) can simulate different illumination angle highlighting and strengthening the micro morphological characteristics to identify landslides effectively, that provides the real terrain observation data for landslides emergency; Compared with optical image, shaded relief map can reveal subtle fault broken terrain, the structural characteristics of small ups and downs, if do research in different echoes, the dynamic changes of the landform features can be depicted to provide a more effective technical methods for the high precision active faults structure research.

ACKNOWLEDGEMENTS

This work was supported by Mineral resources exploitation & environmental remote sensing monitoring project. (No. 121201203000160009) .

REFERENCES

Booth, A. M., ROERING, J. J., 2009. Automated landslide mapping using spectral analysis and high resolution topographic

data: Puget Sound lowlands, Washington, and Portland Hills, Oregon. *Geomorphology*, 109 (3), pp. 132-147.

Berti, M., Corsini, A., Daehne, A., 2013. Comparative analysis of surface roughness algorithms for the identification of active landslides. *Geomorphology*, 182(427),pp.1-18.

Bowles, C.J., Cowgill, E., 2012. Discovering marine terraces using airborne LiDAR along the Mendocino-Sonoma coast, northern California. *Geosphere* ,8 (8),pp. 386-402.

Deparis, J., Fricout, B., Jongmans, D., Vllemin, T., 2008. Combined use of geophysical methods and remote techniques for characterizing the fracture network of a potentially unstable cliff site (the “Roche du Midi”, Vercors massif, France). *J. Geophys. and Engineer*, 5 (2), pp. 147-157.

Gleenn, N. F., Strutker, D. R., Chadwick, D. J., Thackray, G. D., 2006. Analysis of LiDAR-derived topographic information for characterizing and differentiating landslide morphology and activity. *Geomorphology*, 73 (1-2) pp. 131-148.

Hengl, T., Reuter, H., 2009. *Geomorphometry Concepts, Software, Applications*. Elsevier, pp. 796.

Mckean, J., Roering, J., 2004.Objective landslide detection and surface morphology mapping using high-resolution airborne laser altimetry. *Geomorphology,* 57 (3-4), pp. 331-351.

Lan, H. X., Mertin, C. D., Zhou, C. H., Lim, C. H., 2010. Rockfall hazard analysis using LiDAR and spatial modeling. *Geomorphology*, 118 (1-2), pp. 213-223.

Mccollister, C. M., Comey, R. H., 2009. Using LiDAR (Light Distancing And Ranging) data to more accurately describe avalanche terrain. Proc. *International Snow Science Workshop*, pp. 117-119.

Pfeifer, N., Mandlburger, G., 2008. LiDAR data filtering and DTM generation.*Topographic laser ranging and scanning: Principles and processing*, pp. 307-334.

Rufin Soler, C., Hequette, A., Gardel, A., 2008. Assessing the vulnerability of coastal lowlands to marine flooding using LiDAR data, Sangatte coastal dunes, northern France. Z., *Geomorph. Supp*l, 52 (3), pp.195-211.

Rutzinger, M., Hofle, B., Hollaus, M., 2008. Object-based point cloud analysis of fullwave form airborne laser scanning data for urban vegetation classification. *Sensors*, 8 (8), pp. 4505–4528.

Staley, D.M., Wasklewicz, T.A., Blaszczynski, J.S., 2006.
Surficial patterns of debris flow deposition on alluvial fans in Death Valley, CA using airborne laser swath mapping data. *Geomorpholog*y, 74 (1), pp.152-163.

Schmidt, R., Heller, A., Sailer, R., 2005.Vergleich von Laser scanning mit herkommlichen Hohendaten in der dynamische Lawinensimulation mit SAMOS. *Internationale Geodatische Woche Obergurgl, Wichman*n, pp.131-140.

Tarolli, P., Sofia, G., Dalla Fontana, G., 2012. Geomorphic features extraction from high resolution topography: landslide crowns and bank erosion. *Natural Hazards*, pp.1-19.

Van Den Eeckhaut, M., Kerle, N., Poesen, J., Hervás, J., 2012. Object-oriented identification of forested landslides with derivatives of single pulse LiDAR data. *Geomorphology*, 173-174(9), pp. 30-42.

Volker, H., Wasklewicz, T., Ellis, M., 2007. A topographic fingerprint to distinguish alluvial fan formative processes. *Geomorphology*, 88 (1), pp. 34-45.

Wichmann V., Rutzinger, M., Vetter, M., 2008. Digital terrain model generation from airborne laser scanning point data and the effect of grid-cell size on the simulation results of a debris flow model. *Hamb. Beitr. Phys. Geogr. und Landschaftsökol*, 19, pp. 103-113.

Revised March 2018

2018 Fifth International Workshop on Earth Observation and Remote Sensing Applications

Application of Object-oriented Classification with Hierarchical Multi-Scale Segmentation for Information Extraction in Nonoc Nickel Mine, the Philippines

Li CHEN Wei LI Xian ZHANG Ling CHEN
China Areo Geophysical Survey and Remote Sensing Center for Land and Resources
Beijing, CHINA
Email: chenlixyz@163.com

Chao CHEN
Marine Science and Technology College
Zhejiang Ocean University
Zhoushan, CHINA
Email: ayang198206@163.com

***Abstract*—At present, high spatial resolution remote sensing images have been widely applied in the ground objects classification. However, the information extraction of typical opencast mining areas by using high spatial resolution remote sensing images is less studied. The open-pit Nonoc nickel mine is one of the largest laterites nickel ore in Philippines. In this paper, based on the data resource of high spatial resolution remote sensing images, we used the method of object-oriented classification with hierarchical multi-scale segmentation to extract ground object information in the Nonoc nickel mining areas. The qualitatively and quantitatively relative analysis between single scale and hierarchical multi-scale identification results shows that hierarchical multi-scale segmentation has better effect and the highest precise, and the overall accuracy and Kappa coefficient are 92.73% and 0.9024 respectively. Consequently the hierarchical multi-scale segmentation method is more suitable to be applied to the information extraction of open-pit laterites nickel mining areas.**

Keywords—hierarchical multi-scale segmentation; object-oriented classification; nickel mine; information extraction; WorldView-2

I. INTRODUCTION

With rapid developments of remote sensing technology, the high spatial resolution images, such as QuickBird, IKONOS, WorldView and GaoFen (GF) data, are widely utilized for classification, in particular the remote places and harsh conditions. The classification results of high spatial resolution images show higher and better precision in the land use/ cover change, agricultural monitoring, road and building extraction [1-4]. Recently, in order to avoid "salt and pepper" effect and take full advantages of the shape and texture features of high spatial resolution images to improve the classification accuracy, object-oriented classification methods with multi-scale segmentation have gradually become the research focus [5]. For the mining area, Zhang et al. (2016) detected the mill tailings by GF-1 data and Yin et al. (2012) extracted the coal mine area by IKONOS data by using object-oriented classification method [6-7]. However, there are fewer researches focused on extraction in the open-pit laterites nickel mining areas by using high spatial resolution images. Due to complexity and inhomogeneity of mining areas, we aim to investigate and exploit the potential of the object-oriented classification on basis of hierarchical multi-scale segmentation and to extract laterites nickel mining areas effectively and automatically by WorldView-2 image.

II. STDUY AREA AND DATA

A. Study area

The Nonoc nickel deposit, one of the largest laterites nickel ore in the Philippines, is located in Nonoc Island, northern Surigao City [8]. It is estimated there are 112 million tons of nickel ore which is mainly laterite oxide ore [9]. The laterite regolith is thicker and the thickness is generally 3~10 m [10]. Owing to abundant resource, shallow depth, high comprehensive utilization value and easy exploration and exploitation, the Nonoc nickel deposit is well known in the world and widely concerned by other countries. In this research, the eastern region of Nonoc nickel deposit (1329 pixels×1873 pixels) is chosen as the study area which is composed of six types of ground object, including water, vegetation, road, soil, pending mining area and mining area.

B. Data and Pre-Processing

The remote sensing data is acquired on March 2, 2012 by WorldView-2 satellite launched on October 8, 2009 from Vandenburg Air Force Base in California. WorldView-2 satellite operates at an altitude of 770 km and an inclination of 98°. The swath width of data is 16.4 km and revisit time is 1.1 day. WorldView-2 satellite sensor simultaneously collect panchromatic imagery of 0.46 m spatial resolution and multispectral imagery with eight bands at 1.84 m spatial resolution which includes four standard bands (red, green, blue and near-infrared1) and four new bands (coastal, yellow, red edge and near-infrared).

The Pre-processing required three steps by ENVI 5.3[11-13]: (1) Radiometric Correction to eliminate the radiometric distortion including radiometric calibration and atmospheric correction; (2) Geometric Correction to acquire the accurate

This work is supported by Youth Innovation Fund Project of Ministry of Land and Resources Key Laboratory of Airborne Geophysics and Remote Sensing Geology(2016YFL16) and Geological Survey Project of China(DD20160117).
978-1-5386-6642-5/18/$31.00 ©2018 IEEE

geographical coordinates and (3) Clip to obtain the study area. The WorldView-2 image of study area is shown in Fig.1.

Fig. 1. True color composite image of WorldView-2 and verification samples in study area

III. METHODS

The extraction of mining areas carried out by object-oriented classification methods on basis of hierarchical multi-scale segmentation technique. First of all, the optimal segmentation scale was analyzed in the study area, and three scale levels were selected for segmentation. Secondly, combined with the spectral features, texture features, shape features and related characteristics of the objects, the classification rules were established. Thus, classification results were extracted by three single scales and hierarchical multi-scale in the study area. At last, the extraction results were evaluated by visual interpretation and confusion matrix with verification sample data.

The method steps were as follows: ① Based on eCognition9.0 software, four bands of Worldview-2 image, which includes blue(B1), green(B2), red(B3) and NIR(B4), were considered as the input data; ②Using hierarchical multi-scale segmentation technology, the scale parameter was 70, shape weight was 0.3 and compactness weight was 0.5 as the first segmentation scale; ③ Normalized difference water index(NDWI) was calculated by using B2 and B4. The objects whose NDWI>0.1 were classified as the water; ④Normalized difference vegetation index (NDVI) was computed by using B3 and B4 in the non-water areas. When NDVI $\geqslant$ 0.37 or (0.25<NDVI<0.37 and Mean（B3）$\leqslant$210), the corresponding objects were extracted as the vegetation; ⑤ The second segmentation scale was executed in the unclassified objects. The scale parameter was 70, shape weight was 0.1 and compactness weight was 0.5; ⑥ In non-vegetation areas, objects were classified as the roads on the basis of density rule (Density$\leqslant$0.9); ⑦The third segmentation scale was carried out in the remaining unclassified objects. The scale parameter was 100, shape weight was 0.1 and compactness weight was 0.5; ⑧ The mining areas were extracted by gray-level co-occurrence matrix mean variance (GLCM std) rule (GLCM std$\geqslant$32 and B1>220 and B3>310) and ⑨The soil and pending mining areas were distinguished by GLCM std and NDVI rules (GLCM std >25 and NDVI<0.17) in the unclassified objects. The flowchart of hierarchical multi-scale segmentation processing is shown in Fig.2.

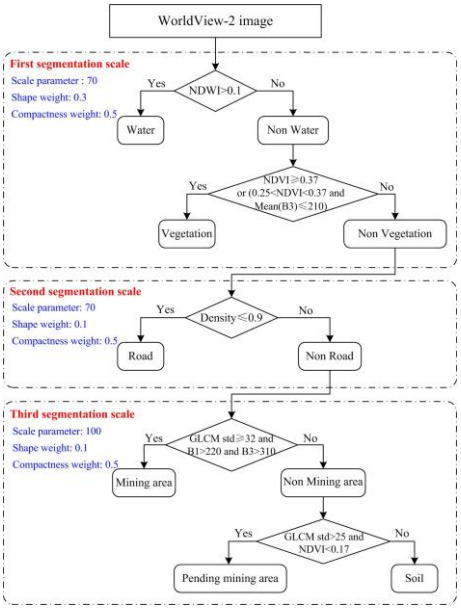

Fig. 2. Flowchart of object-oriented classification method based on hierarchical multi-scale segmentation

IV. RESULTS AND ANALYSIS

The extraction results of the nickel mining areas are shown in Fig.3 and the classification accuracy evaluation is shown in Table 1. In Fig.3, the extractive results of the different segmentation scales indicate that both the water body and vegetation can be fully extracted by using NDWI and NDVI rules. Some regions with higher brightness of mining areas are easy to differentiate. However, owe to the color similarity of lots of unexploited areas, the narrow non-cement roads, bare soil and pending mining areas are difficult to distinguish. Overall, the result of Hierarchical multi-scale shows preferable visual effect. In order to further quantitatively analysis, the extraction accuracy was evaluated by using confusion matrix of 234 verification points (40539 pixels, show in Fig. 1) which were randomly selected in the study area. Compared with three single scales, the hierarchical multi-scale segmentation gave the highest precise. Furthermore, the most raising of overall accuracy and Kappa coefficient are 5.73% and 0.0782 respectively.

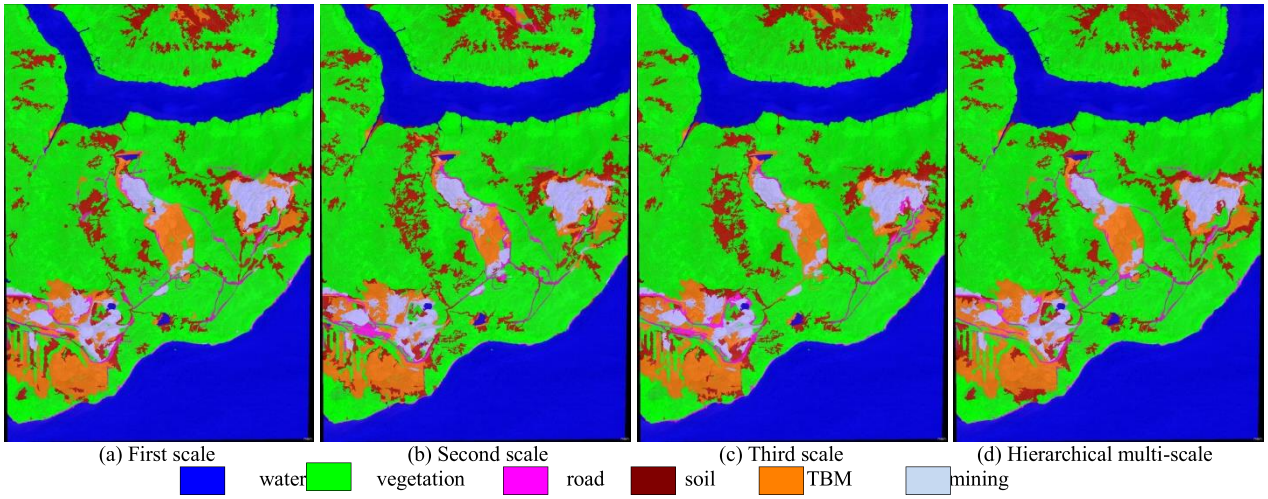

Fig. 3. Extraction results by using object-oriented classification method with different segmentation scales

TABLE I. ACCURACY EVALUATION OF CLASSIFICATION RESULTS

Scales	Mining area		TBM area		Overall accuracy/%	Kappa
	Producer accuracy/%	*User accuracy/%*	*Producer accuracy/%*	*User accuracy/%*		
First scale	99.58	93.86	71.74	65.01	90.65	0.8745
Second scale	99.05	95.78	78.68	65.24	89.25	0.8554
Third scale	96.92	95.50	81.05	59.87	87.00	0.8242
Hierarchical multi-scale	99.85	96.50	83.33	75.25	92.73	0.9024

V. CONCLUSION AND DISCUSSION

Based on the data resource of WorldView-2, our analyzed results show that the information of nickel mining areas is extracted availably and efficiently by using the method of object-oriented classification with hierarchical multi-scale segmentation. The overall accuracy and Kappa coefficient are 92.73% and 0.9024 respectively, indicating that the effect of extraction is better than any single scales. As can be seen from the above analysis, the extracted results are effective and can fully meet application requirements.

However, due to the color similarity, pending mining areas are difficult to discriminate form the bare soil, the producer accuracy and user accuracy are both low. Hence, the future work could pay more attention to the further research of the rules for bare soil and pending mining areas, improving the extractive effects and accuracy. Furthermore, more verification works are very necessary, such as increasing the number of samples to verify the validity and objectivity of the accuracy and applying in other study areas to analyze the robustness and universality of the rules.

REFERENCES

[1] Upadhyay P, Kumar A, Roy P S, et al, “Effect on specific crop mapping using Worldview-2 multispectral add-on bands: Soft classification approach”, Journal of Applied Remote Sensing, 6 (1), pp. 24-35, 2012.

[2] Pacifici F, Chini M, Emery W J, “A neural network approach using multi-scale textural metrics from very high-resolution panchromatic imagery for urban land-use classification”, Remote Sensing of Environment, 113 (6), pp.1276-1292, 2009.

[3] Longbotham N, Chaapel C, Bleiler L, et al, “Very high resolution multiangle urban classification analysis”, IEEE Transactions on Geoscience and Remote Sensing, 50 (4), pp.1155-1170, 2012.

[4] Mutanga O, Adam E, Cho M A, “High density biomass estimation for wetland vegetation using Worldview-2 imagery and random forest regression algorithm”, International Journal of Applied Earth Observation and Geoinformation, 18, pp.399-406, 2012.

[5] Blaschke T, Lang S, Lorup E, et al, “Object-oriented image processing in an integrated GIS/remote sensing environment and perspectives for environmental applications”, Environmental Information for Planning, 2, pp.555-570, 2000.

[6] Zhang Y Y, Remote Sensing Image Based on GF-1 Mining Area of Information Extraction and Modeling, Master Dissertation, North China University of Science and Technology, Tangshan, 2016.

[7] Yin Z, A research on mine area information extraction based on remote sensing image of IKONOS using object-oriented classification, Master Dissertation, Central South University, Changsha, 2012.

[8] Yang X S, Guo Y S, Chen B Y, et al. “The distribution and the exploration, development and utilization situation of the lateritic nickel ore resources in the world”, Acta Geoscientia Sinica, 34(z1), pp.193-201, 2013.

[9] Cui Y L, Yang X S, Jiang Y G, et al. “Metallogenic condition prospecting indicator mineralized type lateritic nickel deposit”, Acta Mineralogica Sinica, 33(4), pp.449-455, 2013.

[10] Guo Y S, Luo Y F, et al, Geological and exploration of lateritic nickel deposits in China and southeast Asia, Geological Publishing House, Beijing, 2013.

[11] Li Chen, Qiming Qin, Yanbing Bai, et al. “Integrating remote sensing and super-low frequency lectromagnetic technology in exploration of buried faults”. 2013 IEEE International Geoscience and Remote Sensing Symposium (IGARSS), Melbourne, pp. 811-814, 2013.07.21-26.

[12] Guangwei Zhen, Li Chen, et al. “Alteration anomaly information extraction using hyperspectral remote sensing in coalbed methane enrichment”. 2016 IEEE International Geoscience and Remote Sensing Symposium (IGARSS), Beijing, pp. 5394-5397, 2016.07.10-15.

[13] Li Chen, Qiming Qin, Chao Chen, et al. “Remote sensing information of mineralizing alteration extraction methods”. 2012 IEEE International Geoscience and Remote Sensing Symposium (IGARSS), Munich, pp. 5947-5950, 2012.07.22-27.

Multiparameter Joint Transformations of Potential Field and Application to Gravity Gradiometry Processing

Yao Luo[1,2], Meiping Wu[1,2], Feng Luo[2], Qing Shu[2], Wenzhi Zhang[2]

[1] *College of Artificial Intelligence, National University of Defense Technology, Changsha, PRC*

[2] *China Aero Geophysical Survey and Remote Sensing Center for Land and Resources, Beijing, PRC*

Abstract

With the rapid development of multiparameter measuring for aeromagnetic and airborne gravity survey, traditional data processing faces new challenges, and multiparameter joint transformations have become a new topic. We propose a procedure framework for multiparameter joint transformations of potential field data in the Fourier domain. The framework was obtained by constructing observations with the potential and minimizing the sum of the data misfit. In the application to gravity gradiometry, we discussed the gravity potential that calculated from the raw tensor components, and proposed a generalized transformation, which contains different weighting factors for different components. We also considered data processing for instrument which acquires two curvature components of the gravity gradient tensor, and discussed the algorithms of determining the potential from curvature components.

Keywords: Multiparameter measurement, transformations of potential field data, airborne gravity gradient, Fourier domain.

Introduction

Nowadays, gravity and magnetic exploration are not satisfied with the traditional measurement of a single field parameter, while simultaneously acquiring a number of field parameters become more and more popular, especially for airborne gravity gradient (AGG) and aeromagnetic survey. As a result of the development of highly sensitive magnetometers, aeromagnetic gradiometry has become another routine choice for exploration, which can add a new dimension to high resolution of shallow magnetic information. AGG survey is the main direction of multiparameter measurement of airborne gravity. In recent years, airborne gravity gradiometer provides very accurate measurements of the spatial variations of the gravity field and its engineering applications or commercial surveys have become common [1]. Multiparameter measurements of potential field, such as AGG measurements, bring new challenges to data processing. The routine transformations for potential field usually just transform one component into another form, while multiparameter survey will acquire multiple parameters simultaneously, hence, it is necessary to consider multiparameter data joint transformations of potential field. In practice, joint transformation of multiparameter data is significant for airborne gravity gradient data processing. Some commercial airborne gravity gradiometers, such as Falcon airborne gravity gradiometer, only acquire GNE and GNU components, and we need multiparameter joint transformations procedure for reconstructing the entire tensor from them.

In order to solve the problem of multiparameter joint transformations for potential field, we first employ the Fourier transform matrix to express the potential field transformation in the frequency domain as a matrix production form. Then we construct the multiparameter as a linear form of the gravitational attraction or magnetic scalar potential. The final potential is obtained by minimizing the data misfit between the multiparameter constructed and observations. The gravitational attraction or magnetic scalar potential then can be used to convert to any parameters of potential field. Since the transformations do not take into account the specific measurement systems, it provides universal framework of multiparameter joint transformations of potential field

data.

Matrix Product Form of Potential Field Transformations

The potential field transformations can be represented as filtering in the Fourier domain. Here we define U_0 as the field to be converted, U_T is the result of transformation, and Λ is the filter of potential field transformation in the Fourier domain. $[U_0]$, $[\Lambda]$ and $[U_T]$ are grid data of $N_1 \times N_2$ size. The relationship of potential field transformations in the Fourier domain can be expressed as Hadamard product of matrices, i.e.

$$[\widetilde{U}_T] = [\Lambda] \circ [\widetilde{U}_0], \tag{1}$$

where $[\widetilde{U}_0]$ and $[\widetilde{U}_T]$ are the Fourier transform of matrices, respectively.

2D Fourier transform can be written in matrix form as (2, 3)

$$vec([\widetilde{U}_0]) = [F_{N_1N_2}]vec([U_0]), \tag{2}$$

$$vec([U_0]) = [F_{N_1N_2}]^{\mathrm{H}} vec([\widetilde{U}_0]). \tag{3}$$

Thus, the equation (1) can be expressed as (4)

$$vec([U_T]) = [F_{N_1N_2}]^{\mathrm{H}} diag\left\{vec\left([\Lambda]\right)\right\}[F_{N_1N_2}]vec([U_0]), \tag{4}$$

where $vec([x]) = [x(0,0), x(1,0), ..., x(N_1-1,0), x(0,1), ..., x(N_1-1, N_2-1)]^{\mathrm{T}}$, $diag(vec([x]))$ will return a square diagonal matrix with the elements of vector $vec([x])$ on the main, $[F_{N_1N_2}] = [f_{N_2}] \otimes [f_{N_1}]$, $[f_N] = \frac{1}{\sqrt{N}} \begin{bmatrix} W_N^{0\times 0} & W_N^{0\times 1} & \cdots & W_N^{0\times(N-1)} \\ W_N^{1\times 0} & W_N^{1\times 1} & \cdots & W_N^{1\times(N-1)} \\ \vdots & \vdots & \ddots & \vdots \\ W_N^{(N-1)\times 0} & W_N^{(N-1)\times 1} & \cdots & W_N^{(N-1)\times(N-1)} \end{bmatrix}$ is the normalized Fourier transform matrix, $W_N = \exp\left(\frac{-i2\pi}{N}\right)$, $W_N^k = \exp\left(\frac{-i2\pi}{N}k\right)$, $i^2 = -1$, the Kronecker product denoted by $\otimes$, and the superscript H denotes complex conjugate transposition.

Therefore, the potential field transformations can be expressed as matrix product of form, i.e.

$$\mathbf{d} = \mathbf{G}\mathbf{m}. \tag{5}$$

For example, we set $\Lambda = \exp(-h\sqrt{k_x^2 + k_y^2})$, representing upward continuation matrix, where $h > 0$, k_x and k_y are the wave numbers in the x and y directions, thus $\mathbf{G} = [F_{N_1N_2}]^{\mathrm{H}} diag\{vec([\Lambda])\}[F_{N_1N_2}]$. If $\mathbf{m} = vec([U_0])$ is the observed field, we can calculate the upward continuation field **d** by using equation (5). If $\mathbf{d} = vec([U_0])$ is the observed field, we can invert the downward continuation field **m** by solving equation (5).

Framework of Multiparameter Joint Transformation

For multiparameter survey, the measurement results can be expressed as a linear form of the gravitational attraction or magnetic scalar potential in the Fourier domain [5]. We set the observation of the multiparameter field is U_j (j = 1,2,3, ... , n), the transformation matrix is $\mathbf{G}_j$, i.e.

$$\mathbf{G}_j = [F_{N_1N_2}]^{\mathrm{H}} diag\left\{vec([\Lambda_j])\right\}[F_{N_1N_2}]. \tag{6}$$

Thus

$$vec([U_j]) = \mathbf{G}_j vec([V]), \tag{7}$$

where V is the gravitational attraction or magnetic scalar potential.

In order to solve the potential in equation (7), we introduce a weighted objective function with the form

$$\phi = \sum_{j=1}^{n} \lambda_j \left\| vec([U_j]) - \mathbf{G}_j vec([V]) \right\|_2^2, \tag{8}$$

where λ_j is the weighted factor. Solving partial derivative of equation (8) on vector V, we will get

$$\frac{\partial \phi}{\partial vec([V])} = 2\sum_{j=1}^{n} \lambda_j \mathbf{G}_j^{\mathrm{H}} \left(vec([U_j]) - \mathbf{G}_j vec([V]) \right). \tag{9}$$

Minimizing equation (8) with the partial derivative is zero, thus

$$vec([V]) = \left(\sum_{j=1}^{n} \lambda_j \mathbf{G}_j^{\mathrm{H}} \mathbf{G}_j \right)^{-1} \sum_{j=1}^{n} \lambda_j \mathbf{G}_j^{\mathrm{H}} vec([U_j]), \tag{10}$$

i.e.

$$vec([V]) = \sum_{j=1}^{n} [F_{N_1 N_2}] diag\{ vec([\frac{\lambda_j \Lambda_j^*}{\sum_{j=1}^{n} \lambda_j \Lambda_j^* \Lambda_j}]) \} [F_{N_1 N_2}] vec([U_j]), \tag{11}$$

where superscript * indicates complex conjugate. Then equation (11) can be written as a simpler form

$$\widetilde{V} = \sum_{j=1}^{n} \frac{\lambda_j \Lambda_j^* \widetilde{U}_j}{\sum_{j=1}^{n} \lambda_j \Lambda_j^* \Lambda_j}, \tag{12}$$

where $\widetilde{V}$ and $\widetilde{U}_j$ are the Fourier transform of V and U_j, and Λ_j is the filter of potential field transformation in the Fourier domain, i.e.

$$\widetilde{U}_j = \Lambda_j \widetilde{V}. \tag{13}$$

Therefore, for multiparameter joint transformations, the gravitational attraction or magnetic scalar potential can be calculated by using equation (12). It provides a universal framework of extracting potential from multiparameter components.

Airborne Gravity Gradient Data Processing Application

Airborne gravity gradient data provide rate of change of a given component of the gravity field in a given direction. Given the three components of the gravity field, there are nine different gradients and they collectively form a tensor at each point in the 3D space. Here, adopting a right-hand Cartesian coordinate system in which the x-axis points to geographic north, y-axis to the east, and z-axis downward, the gravity gradient tensor is represented by

$$\mathbf{T} = \begin{bmatrix} \frac{\partial^2 V}{\partial x^2} & \frac{\partial^2 V}{\partial x \partial y} & \frac{\partial^2 V}{\partial x \partial z} \\ \frac{\partial^2 V}{\partial y \partial x} & \frac{\partial^2 V}{\partial y^2} & \frac{\partial^2 V}{\partial y \partial z} \\ \frac{\partial^2 V}{\partial z \partial x} & \frac{\partial^2 V}{\partial z \partial y} & \frac{\partial^2 V}{\partial z^2} \end{bmatrix} = \begin{bmatrix} \mathbf{T}_{xx} & \mathbf{T}_{xy} & \mathbf{T}_{xz} \\ \mathbf{T}_{yx} & \mathbf{T}_{yy} & \mathbf{T}_{yz} \\ \mathbf{T}_{zx} & \mathbf{T}_{zy} & \mathbf{T}_{zz} \end{bmatrix}. \tag{14}$$

Since the gravitational attraction satisfies Laplace's equation in source-free regions, the

gradient tensor is symmetric and has zero trace, i.e. $\mathbf{T}_{xx}+\mathbf{T}_{yy}+\mathbf{T}_{zz}=0$, and $\mathbf{T}_{mn}=\mathbf{T}_{nm}$, where $m,n=x,y,z$. Consequently, there are only five independent components in the tensor.

The 2D Fourier transform of each gradient tensor component is related to that of the gravitational potential by an algebraic expression

$$\widetilde{\mathbf{T}}=\mathbf{D}\widetilde{V},\quad \mathbf{D}=\begin{bmatrix} -k_x^2 & -k_xk_y & ik_xk_z \\ -k_xk_y & -k_y^2 & ik_yk_z \\ ik_xk_z & ik_yk_z & k_z^2 \end{bmatrix}, \tag{15}$$

where $\widetilde{\mathbf{T}}$ is the Fourier transformation of gradient tensor, k_x and k_y are the wave numbers in the *x* and *y* directions, $k_z=\sqrt{k_x^2+k_y^2}$.

Evaluating potential for full gravity gradient tensor

At present, Gradiometers deployed in commercial systems have two types, partial tensor system with 8 accelerometers and full tensor gradiometer (FTG) [1]. The FTG systems measure five independent components, including $\mathbf{T}_{xx}$, $\mathbf{T}_{xy}$, $\mathbf{T}_{xz}$, $\mathbf{T}_{yy}$, and $\mathbf{T}_{yz}$, but the partial tensor systems only measure two components. For FTG systems, given the 5 components of raw tensor gradient data, it is logical to utilize them to carry out post-acquisition processing to further reject noise. To get utilize tensor gradient, we substitute the linear transformation mapping gravitational attraction to gradient into the framework of equation (12) for calculating the potential

$$V=\frac{-\lambda_{xx}k_x^2\widetilde{\mathbf{T}}_{xx}-\lambda_{xy}k_xk_y\widetilde{\mathbf{T}}_{xy}-i\lambda_{xz}k_xk_z\widetilde{\mathbf{T}}_{xz}-\lambda_{yy}k_y^2\widetilde{\mathbf{T}}_{yy}-i\lambda_{yz}k_yk_z\widetilde{\mathbf{T}}_{yz}}{\lambda_{xx}k_x^4+\lambda_{xy}k_x^2k_y^2+\lambda_{xz}k_x^2k_z^2+\lambda_{yy}k_y^4+\lambda_{yz}k_y^2k_z^2}, \tag{16}$$

where λ_{mn} is the weight of $\mathbf{T}_{mn}$.

If $\lambda_{xx}=\lambda_{xy}=\lambda_{xz}=\lambda_{yy}=\lambda_{yz}$,

$$\widetilde{V}=\frac{-k_x^2\widetilde{\mathbf{T}}_{xx}-k_xk_y\widetilde{\mathbf{T}}_{xy}-ik_xk_z\widetilde{\mathbf{T}}_{xz}-k_y^2\widetilde{\mathbf{T}}_{yy}-ik_yk_z\widetilde{\mathbf{T}}_{yz}}{2k_z^4-k_x^2k_y^2}. \tag{17}$$

It can be found that equation (16) is consistent with the Sanchez's method of extracting potential from gradient components in the Fourier domain [6,7]. Both equation (16) and equation (17) can extract potential from gradient components, but the noise levels of components are different, which are ignored in equation (17). In practice, we should consider the weight of the gradient components observed. Consequently, equation (16) is a generalized method, which considers the different quality of the components. Once the potential is found, the utility of gravity gradient tensor components can then be calculated easily by using equation (15).

Transformation processing for partial tensor system

We also consider the problem of evaluating the gravity gradient tensor components form airborne gravity gradiometers of partial tensor system. Typical partial tensor systems, such as FALCON and HeliFALCON systems, only acquire two curvature components of the gravity gradient tensor namely GNE ($\mathbf{T}_{\mathrm{NE}}$) and GUV ($\mathbf{T}_{\mathrm{UV}}$)

$$\mathbf{T}_{\mathrm{NE}}=\mathbf{T}_{xy}, \tag{18}$$

$$\mathbf{T}_{\mathrm{UV}}=\frac{\mathbf{T}_{xx}-\mathbf{T}_{yy}}{2}. \tag{19}$$

Since these curvature components cannot easily and intuitively be related to the causative geology, they should be transformed into vertical gravity gradient data or gradient tensor data. To evaluating tensor, we can use equation (12) to calculating the gravitational attraction. The potential

can be transformed into GNE and GUV, i.e.

$$\widetilde{\mathbf{T}}_{\mathrm{NE}} = -k_x k_y \widetilde{V}\,, \tag{20}$$

$$\widetilde{\mathbf{T}}_{\mathrm{UV}} = \frac{-(k_x^2 - k_y^2)}{2}\widetilde{V}\,. \tag{21}$$

Thus, we can determine potential directly by equation (12), i.e.

$$\widetilde{V} = \frac{-\lambda_{\mathrm{NE}} k_x k_y \widetilde{\mathbf{T}}_{\mathrm{NE}} - 0.5\lambda_{\mathrm{UV}}(k_x^2 - k_y^2)\widetilde{\mathbf{T}}_{\mathrm{UV}}}{\lambda_{\mathrm{NE}}(k_x k_y)^2 + 0.25\lambda_{\mathrm{UV}}(k_x^2 - k_y^2)^2}, \tag{22}$$

where λ_{NE} and λ_{UV} are the weights of $\mathbf{T}_{\mathrm{NE}}$ and $\mathbf{T}_{\mathrm{UV}}$, respectively.

If $\lambda_{\mathrm{NE}} = \lambda_{\mathrm{UV}}$,

$$\widetilde{V} = \frac{-4k_x k_y \widetilde{\mathbf{T}}_{\mathrm{NE}} - 2(k_x^2 - k_y^2)\widetilde{\mathbf{T}}_{\mathrm{UV}}}{k_z^4}\,. \tag{23}$$

Equation (23) is completely consistent with the potential determined by least-squares approach shown by Pilkington (based on Brewster J, personal communication, 2012) [7].

Pilkington also gave another form of formula for determining potential [7], i.e.

$$\widetilde{V} = \frac{2\left(\widetilde{\mathbf{T}}_{\mathrm{UV}} + i\widetilde{\mathbf{T}}_{\mathrm{EN}}\right)}{\left(k_y - ik_x\right)^2}\,. \tag{24}$$

Pilkington may think that equation (23) and equation (24) are different methods [7]. In fact, equation (23) is consistent with equation (24), because

$$k_x k_y \widetilde{\mathbf{T}}_{\mathrm{UV}} = \frac{k_x^2 - k_y^2}{2}\widetilde{\mathbf{T}}_{\mathrm{NE}}\,. \tag{25}$$

Equation (24) can be transformed into equation (23) according equation (25). Dransfield gives another form of formula to determine vertical gravity gradient (based on Maurice Craig's personal communication) [8], i.e.

$$\widetilde{\mathbf{T}}_{zz} = -2\left(\frac{k_y - ik_x}{k_x - ik_y}\right)\left(\widetilde{\mathbf{T}}_{\mathrm{NE}} + i\widetilde{\mathbf{T}}_{\mathrm{UV}}\right). \tag{26}$$

In fact, according to equation (26), equation (24) and equation (23) are the same. To the best of our knowledge, the methods given in the current literatures have no difference from equation (22), but equation (22) takes into account the different precision of components, and therefore, it is a more general method of evaluating the potential from GNE and GUV.

Processing example of airborne gravity gradiometer

To illustrate the application of multiparameter joint transformations of potential field, we show a real example of airborne gravity gradient data processing. The airborne gravity gradient data collected from a high-resolution airborne gravity gradient (AGG) survey flown over a portion of Great Sand Dunes National Park and Preserve in the San Luis Valley of south-central Colorado[9]. Fugro Airborne Surveys conducted a high-sensitivity HeliFALCONTM AGG survey over survey areas under contract with United States Geological Survey (USGS). Figure 1 shows the grid data of GNE and GUV. The system noises for this survey were 2.88 E and 3.04 E for NE and UV respectively for figure 1. We use equation (22) to calculate the corresponding potential and obtain the vertical gravity gradient grid for interpretation. Figure 2 shows the result of the vertical gravity gradient grid, where the weight coefficients in the processing are 1/2.88 and 1/3.04, respectively. We compared the Figure2 with the vertical gravity gradient grid published by the USGS, and neither of them considered long wavelengths. The example verifies our algorithm.

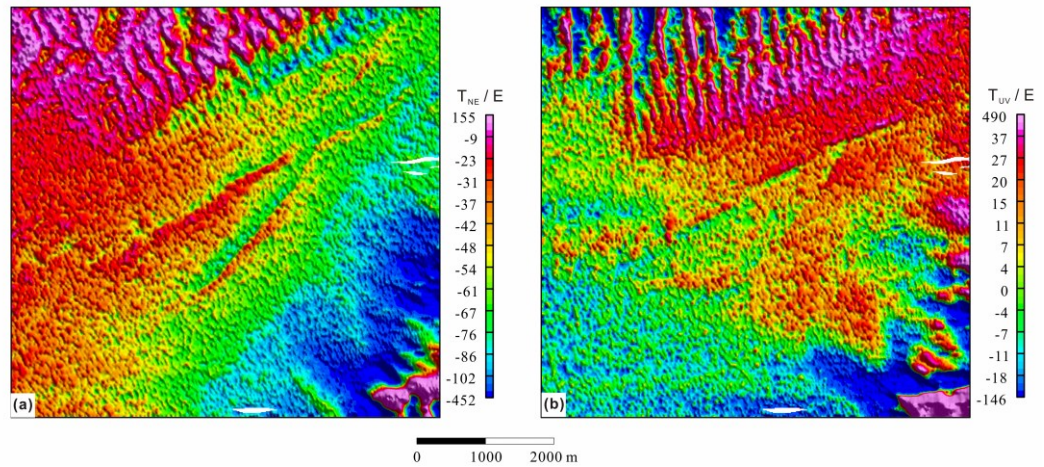

Figure 1. The measured airborne gravity gradients GNE (a) and GUV (b)

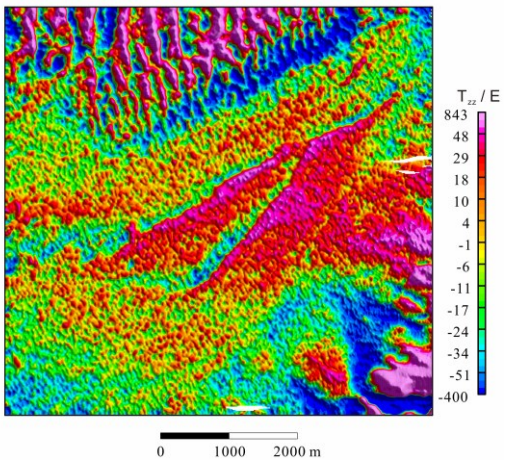

Figure 2. Result of the vertical gravity gradient

Conclusions

With the rapid development of multiparameter measuring for aerogeophysical survey, we established a procedure framework for multiparameter joint transformations of potential field data. The framework is obtained by constructing the transformation relations between the multiparameter observations and the potential, and minimizing the sum of the data misfit. By using the framework, we discussed the gravity potential calculated from the gradient tensor components, and proposed a generalized transformation, which contains the different weighting factor of different components. We also pointed out that there is essentially no difference between the various methods of evaluating gravity gradient tensor components or gravity potential from the curvature components in the Fourier domain.

Acknowledgments

This work was supported by the National Key Research & Development Program of China (2017YFC0602000, 2017YFC0601700, 2017YFC0601600) and China Geological Survey Project (DD20189410). The airborne gravity gradient data in Figure 1 are downloaded from United States Geological Survey (USGS).

References

[1] Dan, D., Daniel, K. and Thomas, M., 2007, Gravity gradiometer systems - advances and challenges: ASEG Extended Abstracts 2007: 19th Geophysical Conference, 1-4. doi: 10.1071/ASEG2007ab034
[2] Ghouse, M. A., 1993, 2D grid architectures for the DFT and the 2D DFT: Journal of VLSI signal processing systems for signal, image and video technology, 5(1), 57-74. doi: 10.1007/BF01880272
[3] Rao, K. R., Kim, D.N. and Hwang, J. J., 2010, Fast Fourier transform - Algorithms and applications: Springer. doi: 10.1007/978-1-4020-6629-0
[4] Luo, Y. and Wu, M. P., 2016, Minimum curvature method for downward continuation of potential field data: Chinese Journal of Geophysics, 59(1), 240-251. doi: 10.6038/cjg20160120
[5] Blakely, R. J., 1996, Potential theory in gravity and magnetic applications: Cambridge University Press.
[6] Sanchez, V., Sinex, D., Li, Y., Nabighian, M., Wright, D. and Smith, D. V., 2005, Processing and inversion of magnetic gradient tensor data for UXO applications: Symposium on the Application of Geophysics to Engineering and Environmental Problems 2005, 1193-1202. doi: 10.4133/1.2923435
[7] Pilkington, M., 2014, Evaluating the utility of gravity gradient tensor components: Geophysics, 79(1), G1-G14. doi: 10.1190/geo2013-0130.1
[8] Dransfield, M. H. and Christensen, A. N., 2013, Performance of airborne gravity gradiometers: The Leading Edge, 32(8), 908-922. doi: 10.1190/tle32080908.1
[9] Drenth, B.J., Abraham, J.D., Grauch, V.J.S., and Hodges, G., 2013, Digital data from the Great Sand Dunes airborne gravity gradient survey, south-central Colorado: U.S. Geological Survey Open-File Report 2013-1011.
.

2018 Fifth International Workshop on Earth Observation and Remote Sensing Applications

Comparative Analysis of the Fusion Methods Based on GF-3 Radar and GF-1 Multispectral Data

Zhengbo Fu
China Aero Geophysical Survey and Remote Sensing Center for Land and Resources
Beijing, China
marcofu_whu@163.com

Jianwei Qi
China Aero Geophysical Survey and Remote Sensing Center for Land and Resources
Beijing, China
29970092@qq.com

Dandan Zhang
China Aero Geophysical Survey and Remote Sensing Center for Land and Resources
Beijing, China
68753490@qq.com

Jie Wang
China Aero Geophysical Survey and Remote Sensing Center for Land and Resources
Beijing, China
wangjie0039@163.com

Wei Zhang
China Aero Geophysical Survey and Remote Sensing Center for Land and Resources
Beijing, China
dave6806@163.com

Xu Han
China Aero Geophysical Survey and Remote Sensing Center for Land and Resources
Beijing, China
eqbeowulf@163.com

***Abstract*—To make better use of the advantages of radar and promote the application of image fusion based on radar data, the author uses different fusion methods based on GF-3 SAR and GF-1 MSS, and evaluates the fusion results by analyzing mean, variance, information entropy, average gradient, spectral distortion and correlation coefficient. The results show that HSV and GS transforms have the best performances in overall. PC is recognized as the third, while it is still remarkable that it has the best ability of spectral retention. And the specialty in NIR band makes PC more conducive for extraction of vegetation. Brovey and Multiplicative transforms are not effective in comparison.**

Keywords—GF-3, multispectral image, SAR, fusion, remote sensing

I. INTRODUCTION

With the increase in the quantity of remote sensing satellites, the amount of multi-sensor and multi-resolution images has also grown explosively [1]. The technology of image fusion solves the problem that high spatial resolution and multi-spectral properties cannot be provided by a single sensor at the same time. However, previous research is more focused on optical images rather than radar data. In recent years, North China has been affected by heavy fog more frequently. Optical images are subject to cloud and fog shielding so that they cannot provide valuable fusion images. Radar can make all-weather and all-day observation of the earth. To some extent, radar can break the restriction of optical images which are vulnerable to cloud and fog shielding. Although there are related studies about the fusion using radar and optical images, research on image fusion using GF-3 SAR data is few as GF-3 has just been in service less than two years. For new ideas on utilizing radar and optical image, the author attempts to explore different fusion methods based on GF-3 SAR and GF-1 multispectral data, and evaluate the fusion result by analyzing indexes including mean, variance, information entropy, average gradient, spectral distortion and correlation coefficient [2].

II. DATA PREPROCESSING

The research is based on the east of Anyang City, Henan Province. The experimental data include GF-3 radar data and GF-1 multispectral data. The acquired date of GF-3 radar data is 31st January, 2017, with a spatial resolution of 3 meters. The multispectral data include a four-band image with a spatial resolution of 8 meters and its acquired date is 18th June, 2016. Types of features on the ground in this study area include buildings, roads, water, vegetation, etc.

The preprocessing of radar data include spatial filtering, radiation calibration, multi-look, geocoding, terrain radiation correction and reprojection. Side-view radar is commonly suffered from speckle noise. The speckle noise is randomly distributed in the image and mixed with the ground objects, with a result of reducing the spatial resolution of the radar image. Therefore, the suppression of speckle noise is particularly important before the fusion of radar and multispectral data. Because of its importance, filtering is widely used to reduce image noise. Among the common filtering methods, Frost filter is a minimum mean square error algorithm which adapts to the local statistics of the image to preserve edges and small features. It can smooth noise while maintaining the edge information and the details of the image, without reducing the clarity of the radar image. Compared with the median filter and the average filter, the Frost filter is a better choice. A 3×3 filter window is selected for noise reduction in this paper. It should be noted that the rise and fall of the terrain has a certain influence on the geometric and radiation of the radar. Although the study area is in the plain, the terrain radiation correction of radar should be applied DEM to weaken the geometric deformation caused by the terrain, for a better registration between radar and multispectral image. The

This work was jointly supported by "National Key R&D Program of China" (No.2017YFB0503803), and "Geological and mineral evaluation project of the China Geological Survey" (No.DD20160077).

978-1-5386-6642-5/18/$31.00 ©2018 IEEE

preprocessing of GF-1 multispectral data includes atmospheric correction and geometric correction before fusion.

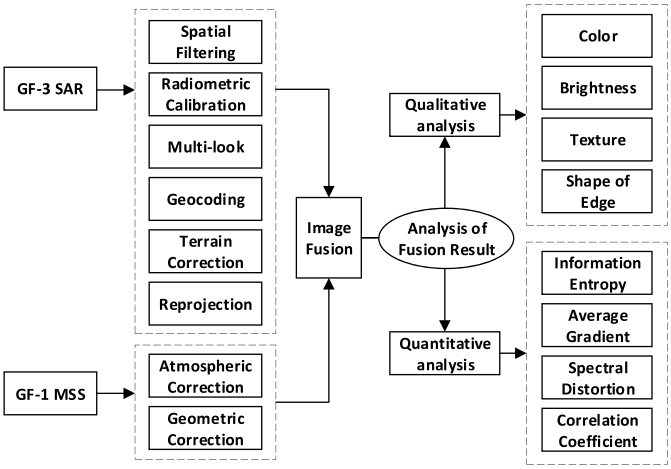

Fig. 1. Data Processing and research methods

III. Research Methods

The research methods include image fusion and the evaluation on fusion quality. Fig.1 shows the research procedure.

A. *Image fusion methods*

The purpose of image fusion is to get an accurate and stable interpretation result on the premise of improving the clarity of the image while not changing spectral characteristics [3]. The methods of fusion are diversified for different application purpose. Fusion methods such as HSV, Brovey, PC, GS and Multiplicative are adopted in this paper because of the characteristic of the ground objects. Because only three bands can be participated in the operation in HSV transform, all the fusion methods in this experiment use band 4(NIR), 3(Red), and 2(Green) to calculate and display for a more intuitive visual effect, which is standard false color synthesis.

1) HSV transform: H, S, V represent hue, sateration and value respectively. The three components are independent 010each other and can be separately controlled, so that the color features can be quantitatively described by them. And the RGB color space can be quickly converted into HSV space to complete the fusion of images with different resolution.

2) Brovey transform: Also called ratio conversion. It decomposes the image space of multispectral images into color and brightness and calculates them. The algorithm is simple and easy to implement, and can effectively reduce the coefficients in the conversion process [4].

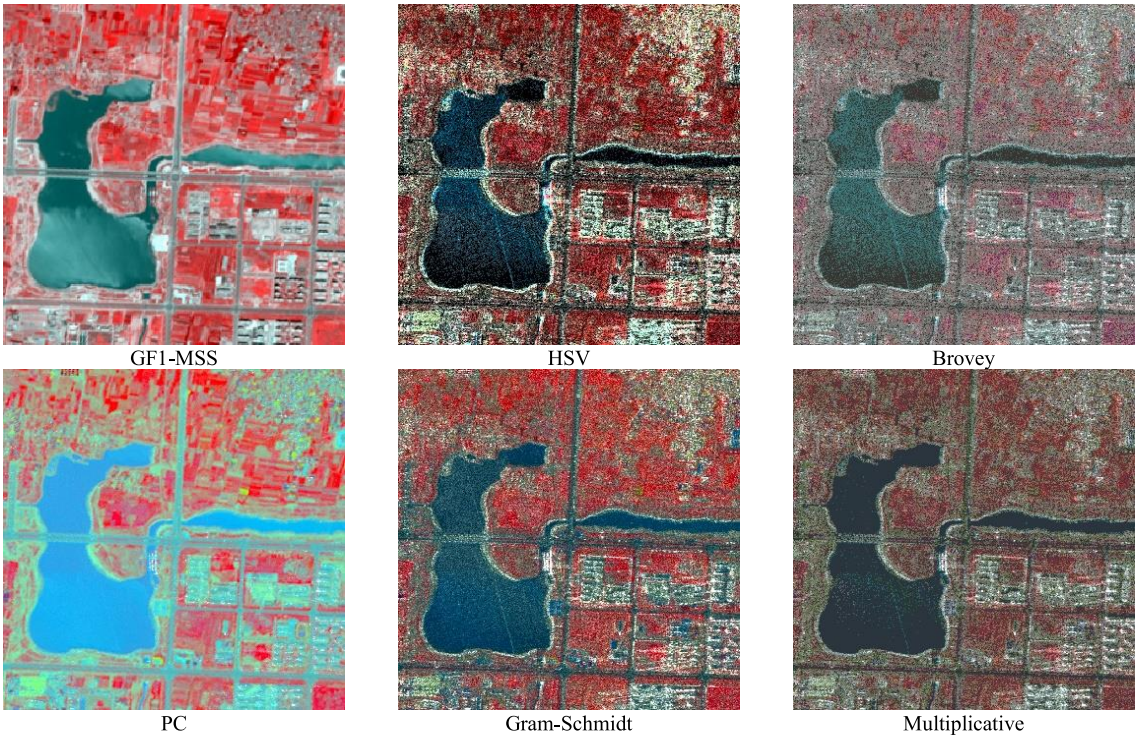

Fig. 2. Fusion results of different methods

3) PC transform: PC is the abbreviation of principal component analysis. It is a multi-band orthogonal linear transformation based on statistics [5]. After transformation, the first component has the most information, while other components would lost information [6].

4) GS transform: GS is the abbreviation of Gram-Schmidt. Like the principle of PC, the Gram-Schmidt transform replaces the first component with the high-resolution radar image, and transforms the multispectral data into orthogonal space, and then makes fusion. It can eliminate redundant information. This method can better maintain the spectral information of the original multispectral data, and solve the problem that the first component information is too concentrated [7].

5) Multiplicative transform: Using the multiplicative algorithm to merge two images with different spatial resolution.

B. Methods of evaluation on Fusion Quality

Quality evaluation of image fusion can generally be divided into qualitative analysis dominated by subjective perceptions, and quantitative analysis measured by objective indicators.

1) Qualitative analysis based on visual observation: Color, brightness, characteristics of the texture, and the shape of the edge can be used to evaluate the effect of fusion by visual observation [8].

2) Quantitative analysis: Some indexes demonstrate more objective evaluation on fusion quality, effectively avoid being too subjective.

a) Mean: Mean is the average of image gray value, which reflects the brightness of the image from the visual side.

b) Variance: It reflects the dispersion of the image gray level. The greater the variance, the more distinct the gray levels. And the contrast will be more obvious, which means more information contained in the image.

c) Information Entropy: It is an important indicator reflecting the richness of information in images.

$$H(x) = -\sum_{i=0}^{2^n-1} P_i log_2 P_i \quad (1)$$

d) Average Gradient: The gradient represents the changing rate of the image gray value and reflects the clarity of the fusion image. Commonly, the decrease of average gradient means the image becomes blurred after fusion.

$$\bar{G} = \frac{1}{(M-1)(N-1)} \times \sum_{i=1}^{M-1} \sum_{j=1}^{N-1} \sqrt{\left(\left(\frac{\partial F(x_i, y_i)}{\partial x_i}\right)^2 + \left(\frac{\partial F(x_i, y_i)}{\partial y_i}\right)^2\right)/2} \quad (2)$$

e) Spectral distortion: Spectral distortion describes the distortion of the spectrum. Higher spectral distortion means more severe distortion the fusion image.

$$D = \frac{1}{M \times N} \sum_{i=1}^{M} \sum_{j=1}^{N} | F(i,j) - F'(i,j) | \quad (3)$$

f) Correlation coefficient: Correlation coefficient describes the retention of spectral characteristics before and after fusion.

$$R = \frac{\sum_{i=1}^{M} \sum_{j=1}^{N} (F(i,j) - \bar{A}_F)(F'(i,j) - \bar{A}_{F'})}{\sqrt{\sum_{i=1}^{M} \sum_{j=1}^{N} (F(i,j) - \bar{A}_F)^2} \sqrt{\sum_{i=1}^{M} \sum_{j=1}^{N} (F'(i,j) - \bar{A}_{F'})^2}} \quad (4)$$

IV. Quality Evaluation of Image Fusion

As shown in Fig.2, visual observation and contrast should be carried out after clipping the fusion images with a fixed size window and same location. In ArcGIS, it can be found that the multispectral image is more blurred than the fusion result while zooming to raster resolution, which shows that the fusion images have significantly improved in spatial resolution.

TABLE I. The Evaluation Indexes of Images and Bands

Data	Band	Mean	Variance	Information Entropy	Average Gradient	Spectral distortion	Correlation coefficient
GF-3		2.70	10.71	2.74	1.54		
	Green	57.97	523.23	6.46	9.68	0.00	1.00
GF1-MSS	Red	72.51	862.25	6.83	12.27	0.00	1.00
	NIR	103.19	892.24	6.73	9.72	0.00	1.00
	Green	64.50	2477.65	6.84	32.76	28.59	0.39
HSV	Red	81.63	4000.46	6.49	41.12	35.83	0.43
	NIR	112.76	4581.89	4.28	55.83	44.67	0.25
	Green	2.35	9.90	2.50	1.30	55.90	0.20
BROVEY	Red	2.26	8.60	2.45	1.23	70.55	0.23
	NIR	2.39	6.01	2.58	1.29	101.12	0.23
	Green	40.40	54.62	4.75	1.87	19.95	0.60
PC	Red	39.33	95.62	5.23	2.28	33.60	0.82
	NIR	83.10	292.53	6.06	2.98	24.41	0.79
	Green	49.78	1168.14	6.66	20.61	22.00	0.38
GS	Red	60.84	1930.38	7.02	28.30	30.42	0.34
	NIR	92.83	2371.82	7.45	28.65	30.15	0.53
	Green	4.71	3.11	1.64	0.67	53.28	0.34
MULTIPLICATIVE	Red	6.17	4.96	2.06	0.88	66.34	0.36
	NIR	7.08	7.03	2.62	1.33	96.12	0.22

A. *Qualitative evaluation*

The HSV transform well preserves the color and brightness. The edge and shape of lakes and roads are relatively clear and artificially developed areas such as buildings exhibit brightly in the image, which make it to be easily identified. However, some of the texture features are also lost.

The image after Brovey transform looks dark and gray, different features are mixed together. The shape and outline of the ground objects are too blurred to be identified visually.

Although the color distortion of building area is serious in PC, vegetation and lakes are easy to identified since being enhanced, and the texture is clearer than other methods

The effect of GS transform is good. The brightness is moderate while details of the building area are well preserved. The color is relatively close to the original multispectral image.

Both the shape and the edge information in the image are partially lost after Multiplicative transform. The fusion image looks dark and gray which make it difficult to identify the features on the ground.

B. *Quantitative evaluation*

To analyze the fusion results more objectively, the mean, variance, information entropy, average gradient, spectral distortion, and correlation coefficient of each image were calculated to make quantitatively analysis. The results are shown in TABLE I.

As shown in Fig.3(a), compared with GF-1 MSS, only HSV transformation among the five fusion results has an increased mean value. Among other transforms, Brovey and Multiplicative have the most mean-attenuation which are less than 1/10 of GF-1 MSS in each band with a serious loss of brightness information. The results are consistent with the visual observation.

As shown in Fig.3(b), the variance is significantly increased after HSV and GS transform, especially in the Red and NIR bands, which indicates the wealth of gray information of those two bands. On the contrary, the variance after PC, Brovey, and Multiplicative transforms have reduced. The variance after Brovey and Multiplicative are reduced by more than a hundred times, which directly reflected the visual results of gray and dark.

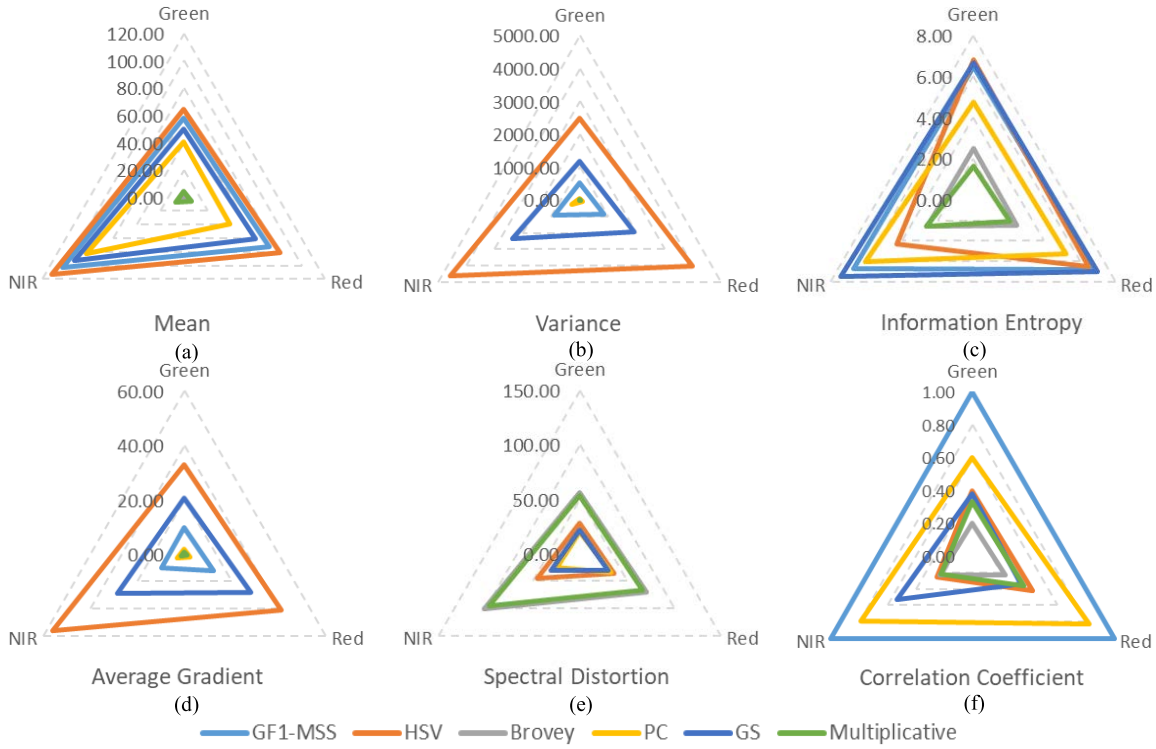

Fig. 3. Radar chart of different indexes and bands

The information entropy is shown in Fig.3(c). The information entropy after GS transform exceeds the original multispectral in three bands, indicating that the information volume is improved. The information entropy of HSV and PC is relatively close to GF-1 MSS. However, the information entropy of HSV reduce more in the NIR band than the other two bands. The information entropy has a big loss after Brovey and Multiplicative transform.

As shown in Fig.3(d), HSV has the largest average gradient, especially in NIR band, which is followed by GS transform. And they are both higher than GF-1 MSS. The edge information of the ground objects has significantly enhanced, and the clarity of fusion images after HSV and GS are increased. Although Brovey and PC transforms maintain the average gradient close to the GF-3 radar image, it still has a significant reduction compared to GF-1 MSS. Multiplicative transform has the smallest average gradient which is most blurred image with indistinguishable details.

Fig.3(e) shows the spectral distortion of each fusion method. Since they are all referenced to GF-1 MSS which spectral

distortion is 0. The closer to the center of the triangle, the smaller spectral distortion. PC has the smallest spectral distortion, followed by GS and HSV. Brovey and Multiplicative have the most severe distortions.

The correlation coefficient is referenced to GF-1 MSS which correlation coefficient is 1. Therefore, the larger area the delta covered in the Fig.3(f), the stronger the ability to maintain the spectrum [9]. PC transform has the highest correlation coefficient, which is close to 0.8 in the Red and NIR bands and slightly lower in the Green band. The correlation coefficient of other fusion results is less than 0.5 except for GS in the NIR band which correlation coefficient is 0.53. Brovey is the lowest one with the weakest ability of keeping the spectrum characteristic.

TABLE II. SORTING OF FUSION METHODS IN DIFFERENT INDEXES

Indexes	**Area of the delta sorted in descending order**				
Mean	HSV	GS	PC	Multiplicative	Brovey
Variance	HSV	GS	PC	Brovey	Multiplicative
Information Entropy	GS	HSV	PC	Brovey	Multiplicative
Average Gradient	HSV	GS	PC	Brovey	Multiplicative
Spectral distortion	Brovey	Multiplicative	HSV	GS	PC
Correlation coefficient	PC	GS	HSV	Multiplicative	Brovey

V. CONCLUSION

At present, the fusion technology based on panchromatic and multispectral images is very mature, but fusion of radar data and multispectral is rarely applied in practical application. In this paper, five common fusion methods and evaluation were applied to merge GF-3 and GF-1MSS with the following conclusions:

A. Qualitative evaluation

The visual observation shows that the fusion results of HSV and GS transforms are better, and the texture of buildings in residential areas is clear. Although the color distortion of PC transform is serious, the vegetation information such as crops and trees has significantly enhanced after PC; The effects of Brovey and Multiplicative transforms are not good enough, for the fusion results are gray and dark, and the details of the ground objects are not clear.

B. Quantitative evaluation

The area of each delta in the radar chart indirectly reflects the evaluation index. Therefore, the area of delta is calculated and sorted in descending order as shown in TABLE II. The quantitative evaluation verifies the visual observation: HSV transform has the highest mean, variance and average gradient, with well-preserved high-frequency information, clear gray levels and good image clarity. GS transform gets the maximum information entropy in all methods. The vegetation information is relatively prominent after PC transform, because of a higher information entropy in the NIR band. PC transform also has the smallest spectral distortion, while Brovey and Multiplicative are ranked behind in distortion. The correlation between PC and GF-1 MSS is the highest which indicates the best spectral retention ability. GS and HSV are following behind, but still under 0.6.

In summary, HSV and GS transforms have the best performances in overall. PC is recognized as the third, while it is still remarkable that it has the best ability of spectral retention. And the specialty in NIR band makes it more conducive for extraction of vegetation. Brovey and Multiplicative transforms have the worst fusion effect. In the future, more multispectral data sources should be adopted to explore the differences on the fusion between different multispectral data and radar data.

ACKNOWLEDGMENT

This work was jointly supported by “National Key R&D Program of China” (No.2017YFB0503803), and “Geological and mineral evaluation project of the China Geological Survey” (No.DD20160077).

REFERENCES

[1] C. Pohl, J. L. Van Genderen. "Review article multisensor image fusion in remote sensing: concepts, methods and applications." International journal of remote sensing 19.5 (1998): 823-854.

[2] R. Raguram, J. M. Frahm, M. Pollefeys. "Exploiting uncertainty in random sample consensus." Computer Vision, 2009 IEEE 12th International Conference on. IEEE, 2009.

[3] G. Simone, A. Farina, F. C. Morabito, et al. "Image fusion techniques for remote sensing applications." Information fusion 3.1 (2002): 3-15.

[4] J. Zhou, D. L. Civco, J. A. Silander. "A wavelet transform method to merge Landsat TM and SPOT panchromatic data." International journal of remote sensing 19.4 (1998): 743-757.

[5] H. Yesou, Y. Besnus, J. Rolet. "Extraction of spectral information from Landsat TM data and merger with SPOT panchromatic imagery—a contribution to the study of geological structures." ISPRS Journal of Photogrammetry and Remote Sensing 48.5 (1993): 23-36.

[6] V. K. Shettigara. "A generalized component substitution technique for spatial enhancement of multispectral images using a higher resolution data set." Photogram. Enggineer. Remote Sen. 58 (1992): 561-567.

[7] C. A. Laben, B. V. Brower. "Process for enhancing the spatial resolution of multispectral imagery using pan-sharpening." U.S. Patent No. 6,011,875. 4 Jan. 2000.

[8] S. Klonus, M. Ehlers. "Performance of evaluation methods in image fusion." Information Fusion, 2009. FUSION'09. 12th International Conference on. IEEE, 2009.

[9] K. G. Nikolakopoulos. "Comparison of nine fusion techniques for very high resolution data." Photogrammetric Engineering & Remote Sensing 74.5 (2008): 647-659.

2018 Fifth International Workshop on Earth Observation and Remote Sensing Applications

Sensitivity analysis about FLAASH model parameters

Jie Wang
China Aero Geophysical Survey and Remote Sensing Center for Land and Resources
Beijing, China, 100083
wangjie0039@163.com

Jianwei Qi
China Aero Geophysical Survey and Remote Sensing Center for Land and Resources
Beijing, China, 100083
29970092@qq.com

Dandan Zhang
China Aero Geophysical Survey and Remote Sensing Center for Land and Resources
Beijing, China, 100083
68753490@qq.com

Zhengbo Fu
China Aero Geophysical Survey and Remote Sensing Center for Land and Resources
Beijing, China, 100083
marcofu_whu@163.com

***Abstract*—When using FLAASH model to process a large number of image data automatically, it is hard to determine model parameters' values exactly. To solve this problem, this paper analyze the sensitivity of mainly 8 model parameters. The simulated GF2 satellite multispectral dataset based on four type land cover was used as input data. These parameters are assumed to be independent and irrelevant, therefore sensitivity analysis is performed using the local analysis method. Variation coefficient was introduced into this paper to quantitatively analyze the effect of these parameters on FLAASH model. Atmosphere model, ground elevation, view zenith angle, and visibility value have dramatic effect on FLAASH model's accuracy, the aerosol model and water column multiplier have little effect on the model. In addition, frequency resolution and view azimuth angle have no effect on the model in all four bands and four land types.**

Keywords—atmospheric correction; FLAASH; sensitivity analysis; surface reflectivity.

I. INTRODUCTION

Atmospheric absorption and scattering are important reasons that cause the radiation distortion of the remote sensing image. Atmospheric correction is the necessary process to removing the effects of the atmosphere [1]. FLAASH is a MODTRAN4-based atmospheric correction model, it derives the surface reflectivity by lookup tables based on MODTRAN simulation data [2]. With high precision, simplicity of use, and applicability, it has been widely used to correct the hyperspectral image and multispectral image. FLAASH model has more than 30 parameters, except for some parameters that we can determine the input value easily, such as latitude and longitude of the image, imaging time, spectral response function, etc. There are remaining mainly 8 parameters that need to be set according to the actual situation, and it is hard to determine these parameters values exactly when processing a large number of image data automatically [3]. If these parameters in the model have little effect on the output of the FLASSH model, we actually do not need to spend so much effort on how to set their values precisely [4]. So sensitivity analysis about FLAASH model parameters seems particularly important, that could provide a reference for identifying the key parameters and how to set their values.

II. METHODOLOGY

A. Analysis method

This paper discussed a total of eight parameters, which are atmosphere model, aerosol model, frequency resolution, ground elevation, view azimuth angle, view zenith angle, visibility value, and water column multiplier. The default values of these parameters are SAS model, rural model, 15cm^{-1}, 1km, 0°, 180°, 40km and 1, respectively. If we consider the correlation between each parameter, the situation will be very complicated. Therefore, this paper assumes that these parameters are independent and irrelevant. Sensitivity analysis of these parameters is performed using the local sensitivity analysis method [5].

This paper changes one parameter value within a reasonable range and make other parameters keep unchanged simultaneously each time. By estimating the change degree of the surface reflectivity under different parameters, sensitivity of these parameters have been analyzed.

The atmosphere model and aerosol model include seven models and four modes respectively; the frequency resolution varies from 5um to 15um in steps of 5um; the ground elevation varies as 0.15km, 0.3km, 0.5km, 1.0km, 1.5km, 2.0km respectively; the view azimuth angle varies from 0° to 180° in steps of 30°; the view zenith angle varies from 150° to 180° in steps of 5°; the visibility value varies from 20km to 45km in steps of 5km; the water column multiplier varies from 0.25 to 1.75 in steps of 0.25.

B. Datasets

In order to quantitatively analyze the results, this paper simulates GF2 satellite multispectral dataset based on four types land cover [6], which are vegetation, water, soil and buildings. GF2 multispectral data has four bands, including blue, green, red and the near-infrared band respectively.

The latitude and longitude of the simulation data are 40°N and 105°E respectively, the imaging date is November 14, 2016, time is 3:30 am, and rows and columns are both 1000, image resolution is 3.2m. The spectral response function of GF2 data in four bands is shown in the Fig. 1.

978-1-5386-6642-5/18/$31.00 ©2018 IEEE

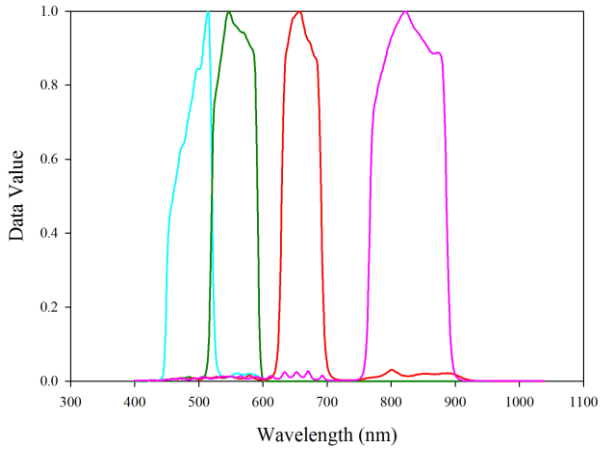

Fig. 1. The spectral response function of GF2 data.

C. variation coefficient

In order to more intuitively view the effect of each parameters on the FLAASH model, this paper uses the variation coefficient to quantify the sensitivity of each parameter [7], Calculation formula of which is

$$C = \sigma / \mu \quad (1).$$

In this equation, C is variation coefficient, μ and σ are respectively average value and standard deviation of the surface reflectivity under different values of each parameter. The standard deviation μ could be calculated as

$$\sigma = \sqrt{\frac{1}{N}\sum_{i=1}^{N}(x_i - \mu)^2} \quad (2).$$

In this equation, μ and σ are respectively average value and standard deviation. Xi is the i-th reflectivity value, N is the number of reflectivity values.

Take the atmosphere model as an example, it has six selectable values. Correspondingly, the FLAASH model has six output reflectivity results. First, the averages and standard deviation of the six reflectivity results would be calculated, then divide the standard deviation by the average and get the variation coefficient in four bands, by which judging the sensitivity of the atmosphere model for the FLAASH model. Generally when the variation coefficient is greater than 0.02, it indicates that this parameter would have a large effect on the model.

III. RESULTS

In order to better analyze the effect of each parameter on the model, this paper makes a statistical analysis in the all four bands of GF2 data. Variation coefficients of each parameter in four bands and four land types have been calculated, By which judging the sensitivity of each parameter in different bands and land types and then providing some help for different application requirements.

A. atmosphere model

The atmosphere model has six selectable values, which are entered into the FLAASH model and we get the surface reflectivity results. Fig. 2 shows the surface reflectivity in four GF2 bands under different values of atmosphere model and four land types: (a) vegetation, (b) water, (c) soil, (d) buildings.

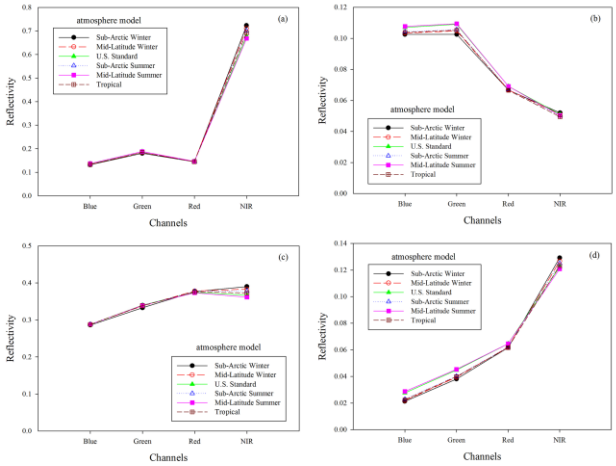

Fig. 2. The surface reflectivity in four GF2 bands under different values of atmosphere model and four land types: (a) vegetation, (b) water, (c) soil, (d) buildings.

It can be seen that atmosphere model could affect reflectivity in the near-infrared band for all four land types, in the blue and green band only for water and buildings land type, in the red band only for buildings land type. There are no significant variations in reflectivity under other conditions.

The variation coefficients of the atmosphere model in four GF2 bands for four land types are shown in the Table 1. The results which the coefficient of variations show are consistent with Fig. 2.

TABLE 1. THE VARIATION COEFFICIENTS OF THE ATMOSPHERE MODEL

	Blue	Green	Red	NIR
Vegetation	0.01561	0.01599	0.00476	0.03083
Water	0.01993	0.02617	0.01719	0.01872
Soil	0.00303	0.00918	0.00440	0.02986
Buildings	0.13054	0.07413	0.02164	0.02619

B. aerosol model

The aerosol model has four selectable values. Fig. 3 shows the surface reflectivity in four GF2 bands under different values of aerosol model and four land types.

We can see that aerosol model could only affect reflectivity in the blue band for buildings land type, and in the near-infrared band for water land type. There are no significant variations in reflectivity under other conditions. Therefore, when setting this parameter, if we do not know the specific value, we could set approximately, that would hardly affect the accuracy of the FLAASH model.

978-1-5386-6642-5/18/$31.00 ©2018 IEEE

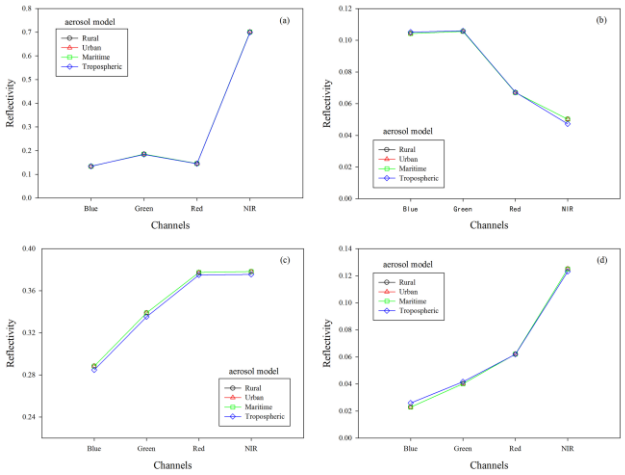

Fig. 3. The surface reflectivity under different values of aerosol model.

The variation coefficients of the aerosol model in four GF2 bands for four land types are shown in the Table 2. The variation coefficients in the blue band for buildings land type, and in the near-infrared band for water land type are greater than 0.02, others are less than 0.02, which show consistent results with Fig. 3.

TABLE 2. THE VARIATION COEFFICIENTS OF THE AEROSOL MODEL

	Blue	Green	Red	NIR
Vegetation	0.00065	0.00331	0.00310	0.00148
Water	0.00443	0.00130	0.00093	0.03082
Soil	0.00613	0.00551	0.00302	0.00361
Buildings	0.06278	0.0166	0.00161	0.00753

C. frequency resolution

The frequency resolution has three selectable values. Fig. 4 shows the surface reflectivity in four bands under different values of frequency resolution and four land types.

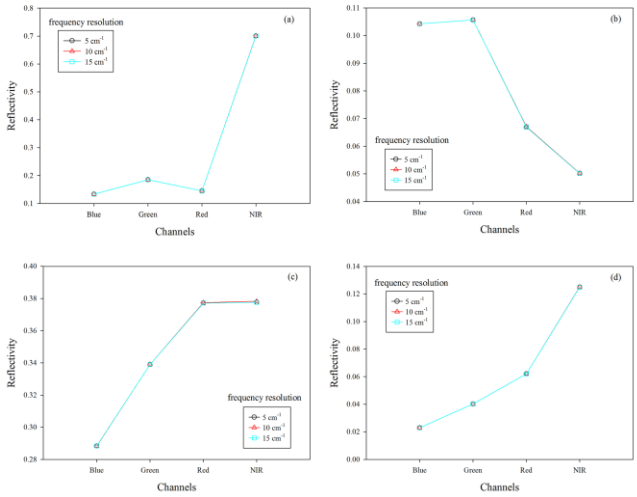

Fig. 4. The surface reflectivity in four GF2 bands under different values of frequency resolution and four land types: (a) vegetation, (b) water, (c) soil, (d) buildings.

There are almost no variations in reflectivity in four bands and four land types, showing the frequency resolution has no effect on the accuracy of the FLAASH model.

Table 3 show the variation coefficients of the frequency resolution, which all less than 0.001.

TABLE 3. THE VARIATION COEFFICIENTS OF THE FREQUENCY RESOLUTION

	Blue	Green	Red	NIR
Vegetation	0.00000	0.00000	0.00029	0.00082
Water	0.00000	0.00014	0.00086	0.00086
Soil	0.00005	0.00004	0.00026	0.00084
Buildings	0.00000	0.00000	0.00023	0.00092

D. ground elevation

The ground elevation has six selectable values. Fig. 5 shows the surface reflectivity in four bands under different values of ground elevation and four land types.

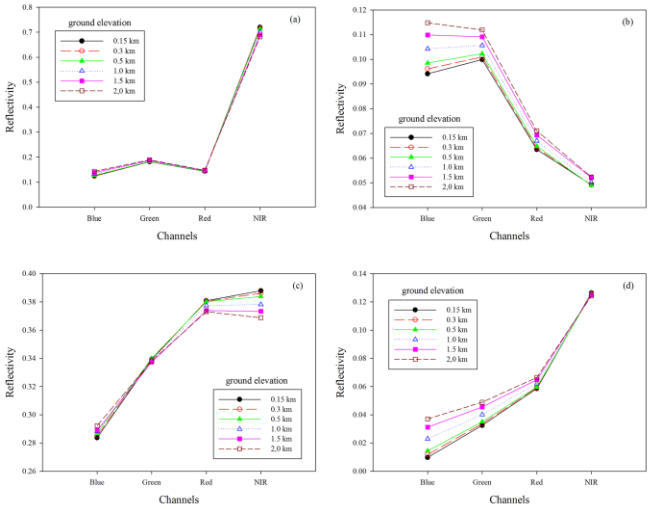

Fig. 5. The surface reflectivity under different values of ground elevation.

Ground elevation has dramatic effect on reflectivity in all four band for water land type, in the blue, green, red band for buildings land type, in the near-infrared band for soil land type. There are no significant variations in reflectivity under other conditions.

The variation coefficients of the ground elevation are shown in the Table 4, range of which are 0.00281 to 0.52329, showing that ground elevation has obviously different effect on the reflectivity for four land types.

TABLE 4. THE VARIATION COEFFICIENTS OF THE GROUND ELEVATION

	Blue	Green	Red	NIR
Vegetation	0.05845	0.01671	0.01079	0.02202
Water	0.07941	0.04555	0.04587	0.03081
Soil	0.01052	0.00281	0.00915	0.02001
Buildings	0.52329	0.17137	0.05291	0.00639

E. view azimuth angle

The view azimuth angle has six selectable values. The surface reflectivity are shown in the Fig. 6.

978-1-5386-6642-5/18/$31.00 ©2018 IEEE

Like frequency resolution, there are no variations in reflectivity in four bands and four land types. The setting of the view azimuth angle would not substantially affect the accuracy of the FLAASH model.

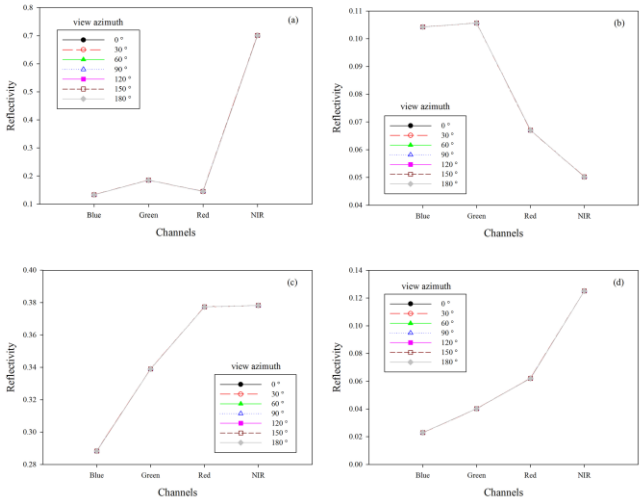

Fig. 6. The surface reflectivity under different values of view azimuth angle.

The variation coefficients of the ground elevation are shown in the Table 5, which are all 0.

TABLE 5. THE VARIATION COEFFICIENTS OF THE VIEW AZIMUTH ANGLE

	Blue	Green	Red	NIR
Vegetation	0.00000	0.00000	0.00000	0.00000
Water	0.00000	0.00000	0.00000	0.00000
Soil	0.00000	0.00000	0.00000	0.00000
Buildings	0.00000	0.00000	0.00000	0.00000

F. view zenith angle

The view zenith angle varies from 150° to 180° in steps of 5°. The surface reflectivity are shown in the Fig. 7.

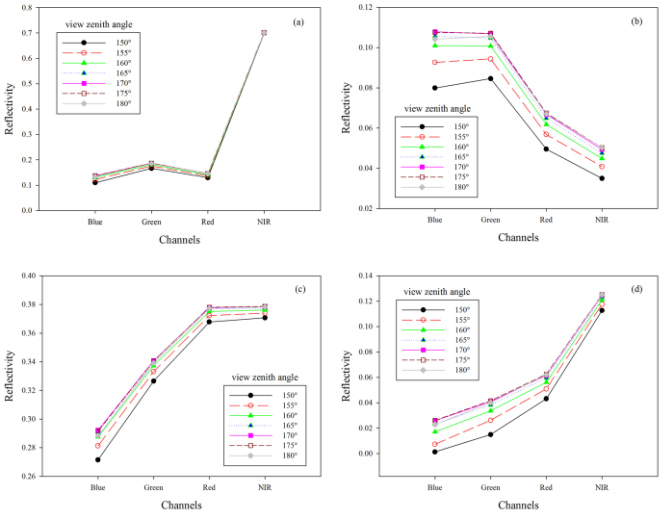

Fig. 7. The surface reflectivity under different values of view zenith angle.

Obviously different from view azimuth angle, the view zenith angle has dramatic effect on reflectivity for water, soil and buildings land types in all four bands, for vegetation land type in blue, green and red bands. The variation coefficients of the ground elevation are shown in the Table 6, most of which are greater than 0.02.

TABLE 6. THE VARIATION COEFFICIENTS OF THE VIEW ZENITH ANGLE

	Blue	Green	Red	NIR
Vegetation	0.07484	0.03924	0.04131	0.00120
Water	0.09835	0.07976	0.10362	0.12131
Soil	0.02505	0.01486	0.00966	0.00751
Buildings	0.72842	0.28234	0.12253	0.03727

G. visibility value

The visibility value varies from 20km to 45km in steps of 5km. The surface reflectivity are shown in the Fig. 8.

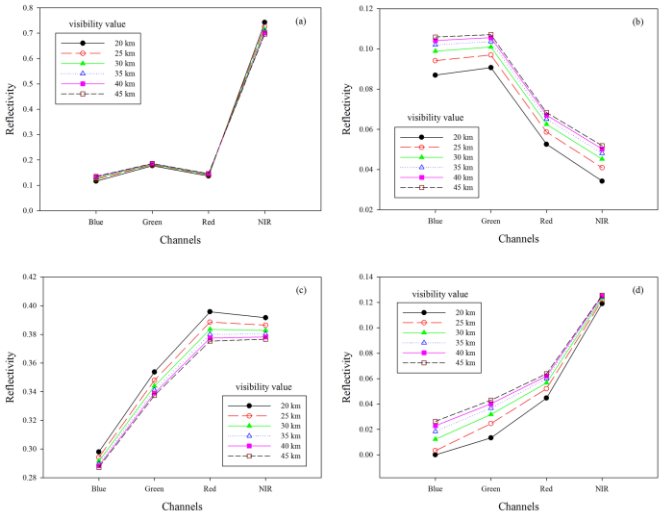

Fig. 8. The surface reflectivity under different values of visibility value.

The Fig.8 shows that the visibility value has a very significant effect on reflectivity in all four bands for four land types, meaning that it has strong sensitivity for FLAASH model. Table 7 shows the variation coefficients of the visibility value, the minimum of which is 0.01378, and the maximum even exceeds 1.

TABLE 7. THE VARIATION COEFFICIENTS OF THE VISIBILITY VALUE

	Blue	Green	Red	NIR
Vegetation	0.05502	0.01756	0.02434	0.02394
Water	0.07193	0.06078	0.09478	0.14551
Soil	0.01378	0.01776	0.01998	0.01460
Buildings	1.14651	0.34971	0.12619	0.01984

H. water column multiplier

The water column multiplier varies from 0.25 to 1.75 in steps of 0.25. Fig. 9 shows the surface reflectivity in four GF2 bands under different values of water column multiplier and four land types.

978-1-5386-6642-5/18/$31.00 ©2018 IEEE

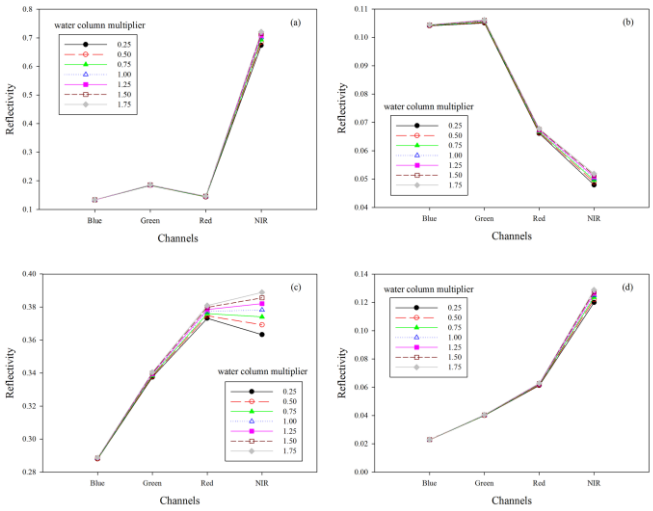

Fig. 9. The surface reflectivity in four GF2 bands under different values of water column multiplier and four land types: (a) vegetation, (b) water, (c) soil, (d) buildings..

The Figure shows that the water column multiplier has a very significant effect on reflectivity only in NIR band for four land types, nor in other bands.

Table 8 shows the variation coefficients of the water column multiplier, which in NIR band are all greater than 0.02, in other bands are less than 0.01.

TABLE 8. THE VARIATION COEFFICIENTS OF THE WATER COLUMN MULTIPLIER

	Blue	Green	Red	NIR
Vegetation	0.00107	0.00332	0.00780	0.02373
Water	0.00116	0.00366	0.00874	0.02802
Soil	0.00095	0.00312	0.00728	0.02413
Buildings	0.00193	0.00439	0.00914	0.02535

IV. CONCLUSIONS

This paper adopts the local sensitivity analysis method to analyze the influences of FLAASH model parameters' changes on the surface reflectivity which is FLAASH model's output. A total of eight adjustable parameters were considered, namely atmosphere model, aerosol model, frequency resolution, ground elevation, view azimuth angle, view zenith angle, visibility value, water column multiplier.

In order to more intuitively view the effect of each parameters on the FLAASH model, this paper uses the variation coefficient to quantify the sensitivity of each parameter, and makes a statistical analysis in the all four bands of simulated GF2 data for four land types.

The analysis results indicate that the atmosphere model, ground elevation, view zenith angle, visibility value have dramatic effect on FLAASH model's accuracy, these parameters require precise values to ensure the accuracy of FLAASH model. Furthermore, the aerosol model and water column multiplier have little effect on the FLAASH model's output. In addition, frequency resolution and view azimuth angle have no effect on FLAASH model in all four bands and four land types, the values of the two parameters could be set approximately as inputs.

This paper provides a good reference for how to set parameters' values when using FLAASH model to process a large number of image data automatically. However, the combination of FLAASH model parameters does not be provided, Because the specific value of each parameter should be set according to the actual situation. Some could be set approximately, and others need to be precise.

I. ACKNOWLEDGMENT

This work was jointly supported by the China Geological Survey under grant 121201203000160007, and the China Aero Geophysical Survey and Remote Sensing Center for Land and Resources.

II. REFERENCES

[1] M. W. Matthew, S. M. Adler-Golden, A. Berk, et al. "Atmospheric correction of spectral imagery: evaluation of the FLAASH algorithm with AVIRIS data." Applied Imagery Pattern Recognition Workshop, 2002. Proceedings. 31st. IEEE, 2002.

[2] Adler-Golden, S., et al. "FLAASH, a MODTRAN4 atmospheric correction package for hyperspectral data retrievals and simulations." Proc. 7th Ann. JPL Airborne Earth Science Workshop. Vol. 97. Pasadena, CA: JPL Publication, 1998.

[3] X. Yang, and Y. Chen, Y. Zhang. "Effect on atmospheric correction by inputting parameters of FLAASH model." Remote Sensing Information 6 (2008): 32-37.

[4] T. Perkins, S. M. Adler-Golden, M. W. Matthew, et al. "Speed and accuracy improvements in FLAASH atmospheric correction of hyperspectral imagery." Optical Engineering 51.11 (2012): 111707.

[5] X. Zhou, H. Lin. "Local sensitivity analysis." Encyclopedia of GIS. Springer, Cham, 2017. 1130-1131.

[6] F. Bian, D. Fan, Y. Zhang, D. Wang. "Synchronous atmospheric radiation correction of GF-2 satellite multispectral image." Fourth Seminar on Novel Optoelectronic Detection Technology and Application. Vol. 10697. International Society for Optics and Photonics, 2018.

[7] H. Abdi. "Coefficient of variation." Encyclopedia of research design 1 (2010): 169-171.

978-1-5386-6642-5/18/$31.00 ©2018 IEEE